Modeling the Dynamics of Liquid Metal in Fusion Liquid Walls Using Maxwell-Navier-Stokes Equations

Suresh Murugaiyan

Dissertation submitted to the Faculty of the

Virginia Polytechnic Institute and State University

in partial fulfillment of the requirements for the degree of

Doctor of Philosophy

in

Aerospace Engineering

Stefano Brizzolara, Co-chair

Bhuvana Srinivasan, Co-chair

Eric Paterson

Colin Adams

December 8, 2023

Blacksburg, Virginia

Keywords: Maxwell-Navier-Stokes, Magneto-Hydrodynamics, Potential Formulation,

Z-pinch, Liquid Metal, Fusion.

Modeling the Dynamics of Liquid Metal in Fusion Liquid Walls Using Maxwell-Navier-Stokes Equations

Suresh Murugaiyan

(ABSTRACT)

The dissertation explores a framework for numerically simulating the deformation of the liquid metal wall's free surface in Z-pinch fusion devices. This research is conducted in the context of utilizing liquid metals as plasma-facing components in fusion reactors. In the Z-pinch fusion process, electric current travels through a plasma column and enters into a pool of liquid metal. The current flowing through the liquid metal generates Lorentz force, which deforms the free surface of the liquid metal. Modeling this phenomenon is essential as it offers insights into the feasibility of using liquid metal as an electrode wall in such fusion devices. The conventional magneto-hydrodynamic (MHD) formulation aims at modeling the situation where an external magnetic field is applied to flows involving electrically conducting liquids, with the initial magnetic field is known and then evolved over time through magnetic induction equation. However, in Z-pinch fusion devices, the electric current is directly injected into a conducting liquid. In these situations, an analytical expression for the magnetic field generated by the applied current is not readily available, necessitating numerical calculations. Moreover, the deformation of the liquid metal surface changes the geometry of the current path over time and the resulting magnetic field. By directly solving the Maxwell equations in combination with Navier-Stokes equations, it becomes possible to predict the magnetic field even when the fluid is in motion. In this dissertation, a numerical framework utilizing the Maxwell-Navier-Stokes system is explored to successfully capture the deformation of the liquid metal's free surface due to applied electric current.

Modeling the Dynamics of Liquid Metal in Fusion Liquid Walls Using Maxwell-Navier-Stokes Equations

Suresh Murugaiyan

(GENERAL AUDIENCE ABSTRACT)

In this dissertation, a method is described that uses a computer to simulate how the initially stable, flat surface of liquid metal deforms when subjected to electrical currents in Z-pinch fusion devices, a specific type of nuclear fusion technology. Z-pinch fusion devices generate plasma, a hot fluid-like substance, through the nuclear fusion process, triggered and maintained by strong pulsated current. There's a growing interest in using liquid metal as the first layer of material to isolate the hot plasma from the rest of the nuclear fusion reactor body, rather than solid materials, due to its unique benefits. However, the Z-pinch fusion process, by introducing electric currents through the liquid metal layer, induces a Lorentz force that consequently deforms the surface of the liquid metal. Developing a tool to predict this deformation is vital as it aids in evaluating the potential of using liquid metal as a plasma-facing layer over solid materials in these fusion devices. The simulation tools presented in this dissertation are able to successfully captures the dynamics of how the liquid metal surface deforms under the impact of electrical currents.

Dedication

To my mother

Acknowledgments

This work was partially supported by the Department of Energy ARPA-E BETHE program under grant number DE-AR0001263. The research has been primarily supported by several semester of research assistantship by Dr. Stefano Brizzolara and two semesters of teaching assistantship by Department of Aerospace Engineering, Virginia Tech.

I would like to thank my advisor, Dr. Stefano Brizzolara, for giving me this opportunity and advising me throughout my PhD journey. I appreciate his help in providing relevant resources. Throughout each phase of the solver development, he actively searched for and provided relevant textbooks and journal articles. I would also like to extend my thanks to my Co-chair, Dr. Bhuvana Srinivasan, and my other committee members, Dr. Eric Paterson and Dr. Colin Adams, for serving on my dissertation committee, providing feedback throughout my PhD journey, accommodating all my PhD exam schedules, and offering feedback on my dissertation document. I would like to express my gratitude to Dr. Saad Ragab for his support and advice with my PhD research. His teaching style and deep understanding of fluid dynamics and computational fluid dynamics have been a significant influence on me, as I took several courses from him in these subjects.

I express my heartfelt gratitude to my family for their unconditional love and support. My thanks go to my mother, Malarmathi; brother, Neelakandan; sister, Suganya; sister-in-law, Saranya; nephew, Nalan; brother-in-law, Arun; and my wife, Nandhini. I am grateful to my brother, who was deeply involved and provided financial support for the final year of my Ph.D., alongside our daily conversations that significantly strengthened my mental health during the challenging last phase of my 7-year long PhD journey.

I thank my friends Aditya and Harsha for being there with me all the time. Harsha has consistently been there to listen to my problems and support me in every way possible. Aditya helped a lot with my research. He guided me in using the PetSC library, pushed me to recognize the advantages of solving non-dimensional equations numerically, understanding different linear solvers and offered invaluable advice on several aspects of my code development and my research. I thank my friend Chaitanya, from whom I improved my programming skills. I appreciate Chaitanya's help with debugging many times when I struggled with my code development. I want to thank my friend Kalay for maintaining contact and providing advice on both personal matters and my PhD journey.

I am thankful for the friendships I developed during my PhD studies. Without their company, my life at Virginia Tech would not have been as fulfilling. I have fond memories with Zhongshu, whom I met towards the end of his PhD studies. We often worked late nights at Randolph hall, shared late-night coffee sessions, and enjoyed activities like swimming, going to the gym, and jogging together. His company made my time at Virginia Tech more enjoyable. I value the time spent with Mustahsin, we both started our PhD journey together. He has always been available for conversations and sharing moments. I thank him for our discussions on strategies for managing both my PhD and various aspects of personal life.

I am happy to have had Emad's friendship and company during my time at Virginia Tech. We lived in the same apartment for most of my stay, and I am thankful to him for always being available to discuss both personal matters and aspects of my PhD life. Our frequent conversations on various topics, including politics, ethics, and religion, have greatly enriched my views. His presence and insights have been a significant part of my journey. I appreciate the company of my labmate, Pavan, whose friendship made me feel at home.

I hold great respect for my friend Yang, who I met near his graduation. Yang has always been there for me, offering consistent emotional support and motivating me. I'm thankful for his help with my solver development. My code improved substantially due to his input, even during times when he was busy with his own graduation and solver completion. I am especially grateful for his encouragement and support over phone calls during the time leading up to my defense, which helped me immensely.

I cannot imagine completing my PhD without the support of my family and friends in dealing with various aspects of my PhD and personal life. Love you all, to my family and friends.

Contents

List of Figures

List of Tables

List of Abbreviations

α	Volume fraction
ϵ	Permittivity of the material (F/m)
ϵ_o	Permittivity of free space (F/m)
ϵ_r	Relative permittivity of material
$\hat{\mathbf{i}}, \hat{\mathbf{j}}, \hat{\mathbf{k}}$	Basis vectors for Cartesian coordinates
$\hat{\mathbf{r}}, \hat{\theta}, \hat{\mathbf{z}}$	Basis vectors for cylindrical coordinates
$\mathbf{g}$	Acceleration due to gravity (m/s^2)
μ	Dynamic viscosity of the fluid (Ns/m^2)
μ	Permeability of the material (H/m)
μ_g	Dynamic viscosity of the gas (Ns/m^2)
μ_l	Dynamic viscosity of the liquid (Ns/m^2)
μ_o	Permeability of free space (H/m)
μ_r	Relative permeability of material
∇	Differential operator $(1/m)$
∇'	Dimensionless differential operator
ω	Angular frequency (rad/s)

Φ Electric scalar potential ($Volt$)

Φ' Dimensionless Electric scalar potential

Φ_o Scale factor for Electric scalar potential ($Volt$)

ρ Density of the fluid (kg/m^3)

ρ' Dimensionless density of the fluid

ρ_c Electric charge density (C/m^3)

ρ_f Free electric charge density (C/m^3)

ρ_g Density of the gas (kg/m^3)

ρ_l Density of the liquid (kg/m^3)

ρ_o Scale factor for density of the fluid (kg/m^3)

σ Electrical conductivity of the material (S/m)

σ' Dimensionless electrical conductivity of the material

σ_g Electrical conductivity of the gas (S/m)

σ_l Electrical conductivity of the liquid (S/m)

σ_o Scale factor for electrical conductivity of the material (S/m)

$\mathbf{A}$ Magnetic vector potential ($V \cdot s/m$))

$\mathbf{A}'$ Dimensionless magnetic vector potential

$\mathbf{B}'$ Dimensionless magnetic flux density

$\mathbf{E}'$ Dimensionless electric field

$\mathbf{F}$	Lorentz force (N)
$\mathbf{J}'$	Dimensionless current density
$\mathbf{J}_c$	Conduction current density (A/m^2)
$\mathbf{J}_d$	Displacement current density (A/m^2)
$\mathbf{J}_u$	Current density induced by flow (A/m^2)
$\mathbf{J}_\Phi$	Current density due to potential (A/m^2)
$\mathbf{U}'$	Dimensionless velocity
$\mathbf{U}_o$	Scale factor for velocity (m/s)
A_o	Scale factor for magnetic vector potential $(V \cdot s/m))$
B_o	Scale factor for magnetic flux density (T)
E_o	Scale factor for electric field (V/m)
f	frequency (Hz)
Fr	Froude number
h	Angular momentum $(kg\, m^2/s)$
Ha	Hartmann number
J_o	Scale factor for current density (A/m^2)
$J_{\Phi o}$	Scale factor for current density due to potential (A/m^2)
p	Pressure (Pa)
p'	Dimensionless pressure

p_o Scale factor for pressure (Pa)

r, θ, z Components of cylindrical coordinates(m, rad, m)

Re Reynolds number

Re_m Magnetic Reynolds number

t' Dimensionless time

t_o Scale factor for time (s)

x, y, z Components of Cartesian coordinates (m, m, m)

$\mathbf{B}$ Magnetic flux density (T)

$\mathbf{D}$ Electric displacement field (C/m^2)

$\mathbf{E}$ Electric field (V/m)

$\mathbf{H}$ Magnetic field intensity (A/m)

$\mathbf{J}$ Current density (A/m^2)

$\mathbf{J}_f$ Free current density (A/m^2)

$\mathbf{U}$ Velocity (m/s)

t time (s)

Chapter 1

Introduction

The pursuit of fusion energy is driven by the promise of a clean, abundant, and sustainable power source, capable of meeting the world's growing energy demands without the adverse environmental impacts associated with fossil fuels. Among the various approaches to achieve controlled thermonuclear fusion, magnetic confinement fusion, and specifically the Z-pinch, represents a fascinating and promising avenue of research.

1.1 Z-pinch and Fusion Liquid Wall

Z-pinch is a type of magnetic confinement fusion in which a large current is passed through a plasma column, creating a very strong magnetic field that helps confine and compress the plasma to conditions suitable for fusion. The strong magnetic field compresses the plasma column to high temperatures and densities necessary for fusion reactions. For fusion to successfully occur, the plasma, under the influence of the Z-pinch, must be maintained at these conditions long enough for temperature, density, and pressure to reach levels sufficient to initiate fusion reactions. Following this initiation, fast-moving neutrons are released from the plasma, striking the blanket surrounding the fusion reactor. When struck by a high-energy neutron, the blanket surrounding the fusion reactor heats up. It is then actively cooled with a cooling fluid, facilitating the transfer of heat to the subsequent systems of the power plant for energy conversion and generation.

Within this plasma, two hydrogen isotopes, Deuterium and Tritium, are the key players in one of the most common methods to achieve fusion. When Deuterium and Tritium are compressed and heated to millions of degrees, their nuclei fuse, creating helium and a neutron. These products carry massive amounts of energy (17.6 MeV of energy) that can be captured and harnessed. The reaction is represented in the equation:

$$ {}_1^2D + {}_1^3T \rightarrow {}_2^4He(3.5 \text{ MeV}) + {}_0^1n(14.1 \text{ MeV}) $$

As mentioned earlier, following the fusion reaction, the plasma emits fast-moving neutrons, which significantly contribute to the reactor's energy production process. As they strike the blanket surrounding the fusion reactor, their kinetic energy is transferred to it, heating it significantly. The blanket surrounding the fusion reactor is not merely a passive component; it's a crucial part of the reactor's wall, often referred to as the 'first wall'. As the immediate boundary interacting with the high-energy plasma and neutrons, it faces the formidable challenge of constant bombardment. This interaction leads to extreme stress and radiation damage, causing wear, degradation, and potentially the introduction of impurities into the plasma. The need for frequent maintenance and replacement of this first wall limits the reactor's efficiency and lifespan.

In response to these challenges, the concept of a liquid wall emerges as a compelling alternative. Often composed of molten metal, this dynamic and self-healing surface is capable of withstanding the harsh conditions within the reactor. The utilization of a liquid wall in such fusion reactors presents a promising alternative to conventional solid walls. Unlike traditional solid materials that may crack and degrade over time, a liquid wall can continuously renew its surface, effectively managing the wear and tear from radiation and heat. Since it continuously flows, the liquid metal can absorb and dissipate the intense heat from the plasma and neutron impacts more effectively than solid materials. Moreover, certain types of liquid walls can be designed to capture and breed tritium, a valuable fuel for fusion reactions, through interactions with the neutrons, thus contributing to the reactor's fuel cycle.

Embracing the liquid wall as the first wall addresses many of the longstanding challenges associated with solid materials in the face of intense fusion reactions, paving the way for more sustainable and efficient fusion energy production. This transition from solid to liquid walls could revolutionize the efficiency and durability of fusion reactors, offering a sustainable solution to the challenges posed by solid wall materials in fusion technology.

Despite the potential benefits of employing a liquid metal wall in Z-pinch fusion reactors, realizing its practical application necessitates a comprehensive understanding of the liquid metal's free surface behavior. Free surface behavior of liquid metal is influenced by Z-pinch plasma currents within the Z-pinch configuration as well as various electromagnetic forces present in the fusion environment. Achieving stable free surface conditions in the liquid metal walls of Z-pinch devices is imperative for effective fusion. Any instability in the liquid metal wall can lead to plasma contamination, thereby affecting the fusion process. Numerous investigations have examined the dynamics of fusion liquid walls under the influence of such forces across diverse reactor designs. The focus of this research is to develop a mathematical model capable of describing the impact of Z-pinch plasma currents on the free surface behavior of the liquid wall.

The Figure 1.1 depicts the schematic representation of the Z-pinch configuration employed in magnetic confinement fusion. The configuration consists of flow of axial current within the plasma column and the generation of an azimuthal magnetic field as a consequence of this current. In Figure 1.2, key aspects of the Z-pinch mechanism is shown. It illustrates the axial current within the plasma column, the resulting azimuthal magnetic field and the compression of the plasma by this magnetic field to fusion conditions.

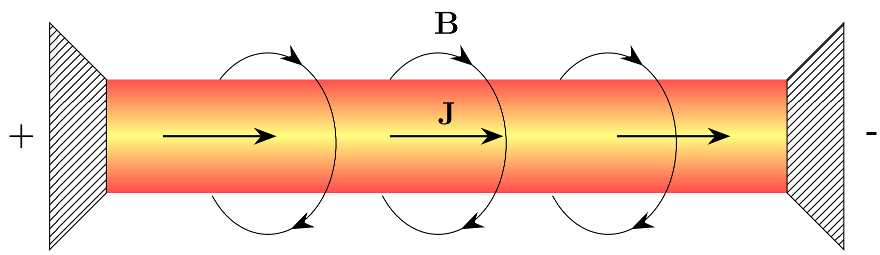

Figure 1.1: Schematic of Z-pinch configuration [5, 13]. **J** represents axial current and **B** azimuthal magnetic field. + and - symbol represents electrodes. The figure is drawn inspired by the sources [5, 13].

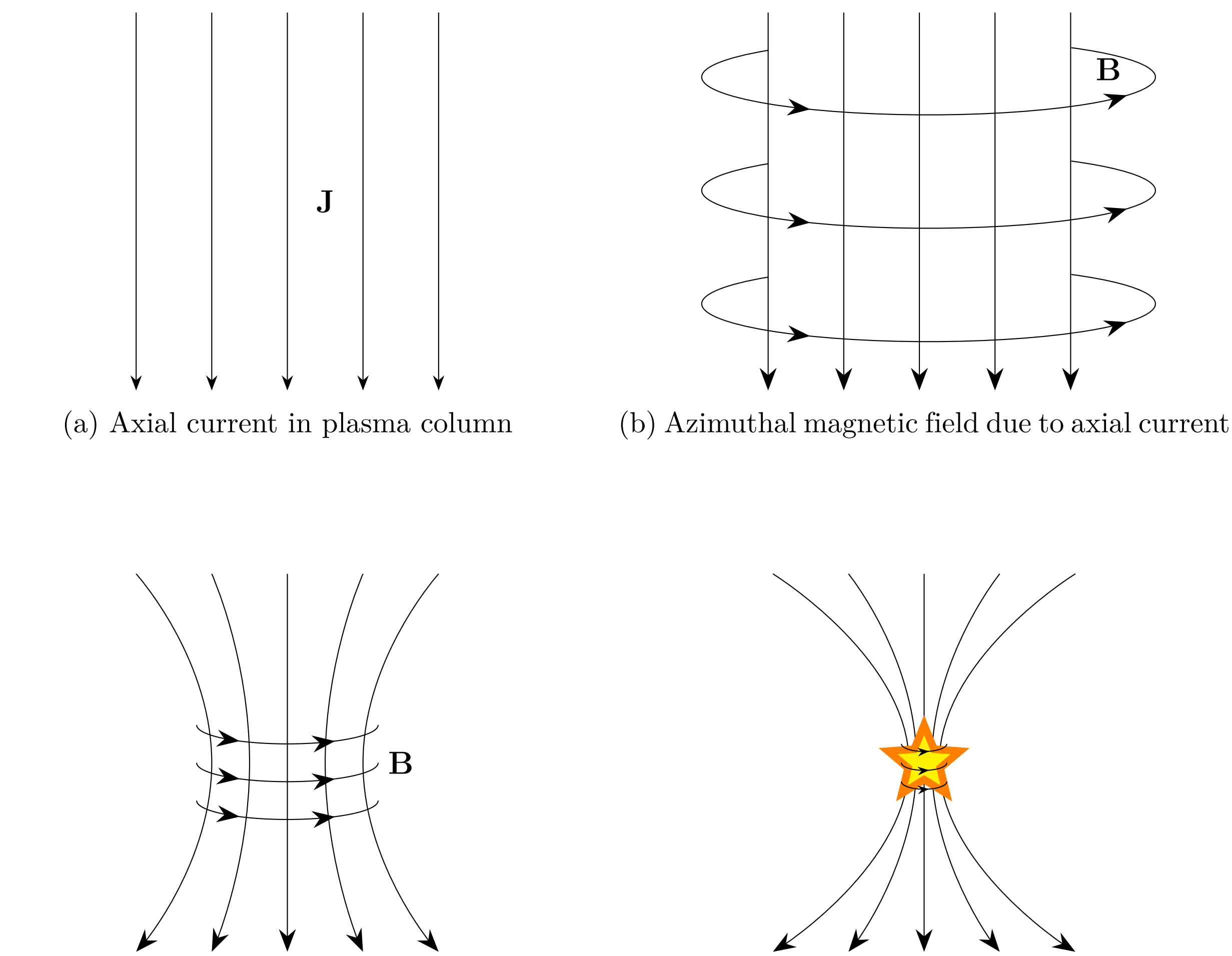

(a) Axial current in plasma column

(b) Azimuthal magnetic field due to axial current

(c) Compression of plasma by magnetic field

(d) Plasma compressed to fusion condition

Figure 1.2: Illustration of Z-pinch mechanism [53]. The figure is adapted from [53].

1.2 Literature review

Although the liquid wall concept offers numerous benefits for fusion reactors, these walls are prone to instabilities caused by electromagnetic forces within the fusion environment. This section provides a concise review of both analytical and numerical research focused on the modeling and stability of fusion liquid walls in the fusion environment.

In a key study by Kevin Brannick [4], an analytical model was developed to study experiments led by Dr. Colin Adam's research team at Virginia Tech. The team at Virginia Tech is working on the possibility of using liquid metal electrodes instead of traditional solid metal ones to improve the long-term performance of Z-pinches. The experiment is simplified by using wire to conduct electricity instead of developing a Z-pinch plasma column as shown in Figure 1.3. The current flowing through the liquid metal generates spatially varying magnetic pressure which creates Lorentz force. Brannick's analytical model looks at how this Lorentz force displaces the liquid metal electrode's free surface, leading to wave formation.

In a contribution by Victoria Suponitsky et al., a magnetohydrodynamics solver known as 'mhdCompressibleInterFoam' was developed in the OpenFOAM suite [46] for simulating compressible two-phase flows with free surfaces. Designed primarily to model the compression of magnetic fields using rotating liquid metal liners within the framework of magnetized target fusion pursued by General Fusion Inc. The evolution of the magnetic field is determined through the toroidal field component and poloidal flux functions. The study investigates the effect of the magnetic field on liner dynamics during implosion, particularly how the magnetic field influences the shape and trajectory of the liner during the process. General Fusion has effectively utilized the "compressibleInterFoam" solver from the OpenFOAM suite for the simulation of imploding liner dynamics and the examination of interface instabilities and their mitigation strategies [1, 33, 45].

In the study [42] conducted by Sun et al., the effects of magneto-hydrodynamic (MHD) drag on flowing liquid metal plasma-facing components were explored, with an emphasis on their potential to facilitate long-pulse operation and high-power exhaust in fusion reactors. The research detailed the consequences of magneto-hydrodynamic drag in conducting liquid metal, notably reducing the flow speed. Through experiments aimed at validating magneto-hydrodynamic drag calculations for both insulating and conducting walls, it was observed that the average flow speed in channels decreases with the use of conducting walls and an increase in the strength of the applied transverse magnetic field. A unique aspect of this work is the presence of a free surface in the flow, distinguishing it from other MHD duct flow experiments. In these free surface flows, the absence of top wall confinement allows the retarding force from the MHD drag to cause a pressure drop, which in turn affects the liquid metal's surface height. This phenomenon results in a variation in surface height along the channel, manifesting most notably as an increased liquid metal depth near the inlet - a 'pileup' effect - while the outlet remains largely unaffected. This behavior, along with other dynamics of liquid metal flow under magneto-hydrodynamic influence, was captured and validated through simulations using software packages OpenFOAM and ANSYS CFX.

In the study [22] conducted by Hvasta et al., the feasibility of using electromagnetic control to manage free-surface liquid metal flows in fusion reactors was investigated. Numerous proposed designs for liquid metal plasma-facing components depend on utilizing Lorentz force for electromagnetic control to maintain adherence to the interior surfaces of the reactor. The necessity for this study arose from the absence of experimental data regarding the electromagnetic control of liquid metal plasma-facing components, prompting a study where electrical currents were introduced into free-surface liquid metal as it flowed through a uniform magnetic field. This approach successfully controlled the flow velocity and depth in line with theoretical predictions, illustrating the capabilities of electromagnetic control.

In a study [10] focused on the stability of liquid metal plasma-facing components, Fiflis et al. explored the potential for ejection of liquid metal into fusion plasma, a significant concern in the implementation of these components in fusion reactors. The study introduced a new theoretical approach based on a modified set of shallow water equations that incorporate surface tension forces, providing a more accurate prediction of lithium surface stability under plasma exposure. This approach utilized shallow water theory to simulate wave propagation on the lithium surface. The model was able to predict conditions leading to lithium ejection and provided a stability boundary for liquid metal surfaces that closely matched experimental observations, offering valuable insights into the design and stability of plasma-facing components in fusion reactors. In agreement with the experiments, the theory predicted that ejections at the edges due to wave impacts against the walls would be more common than ejections from the center of the trenches. The study also highlighted the critical influence of Rayleigh–Taylor and Kelvin–Helmholtz instabilities on the liquid metal surfaces.

In the study [19] conducted by Holgate et al., the electrohydrodynamic stability of a plasma-liquid interface, a critical aspect in the design and operation of magnetic confinement fusion devices like tokamaks, was studied. The paper examines the electric fields and ion flows in the sheath region between the bulk plasma and the liquid, essential for understanding the stability of the liquid surface. By employing a linear perturbation analysis of a liquid-sheath interface, the study determined that if a normal sheath is formed, molten metal surfaces in tokamak edge plasmas can remain stable against the electric field due to the impact of ions on the surface. This analysis provided a deeper understanding of the conditions under which these instabilities occur and suggested that ion bombardment could be a potential method to stabilize the plasma-liquid interface.

In a comprehensive study, Narula et al. explored the behavior of liquid metal film flow under magnetic fields relevant to fusion environments [34]. Their work studies responses of the flowing liquid metal due to the magneto-hydrodynamic forces. The HIMAG computer code was employed for a three dimensional numerical simulation of two-phase flow of electrically conducting liquids. The simulations using HIMAG, specifically on a gallium alloy flow, provided valuable insights, predicting an increase in liquid metal film thickness due to MHD body forces and capturing the tendency of the liquid metal to move away from the side walls.

In the study by Xiujie et al., the team conducts a study on the magneto-hydrodynamic effects on liquid metal film flows in the context of plasma-facing components in fusion technology [54]. Through three-dimensional numerical simulations, the research focuses on understanding the film thickness variation and its surface stability under a gradient magnetic field. They observe three distinct MHD phenomena in film flow: retardant, rivulet, and flat film flow. Their experimental and numerical analyses conclude that flat film flow, which exhibits stable thickness and surface, is a preferable choice for plasma-facing components due to its resistance against the disruptive MHD effects found in other flow types.

The study by Somboonkittichai et al. [40], addresses surface instability in static liquid metal within magnetized fusion plasma, a critical aspect for plasma-facing components in fusion reactors. Utilizing Rayleigh's method to derive a Lagrange equation, the research identifies the primary forces influencing instability, notably the sheath electric field and external magnetic field. It concludes that strong magnetic fields, essential for confinement in fusion devices, predominantly dictate instability. The findings recommend reconsidering the use of static planar free liquid surfaces in advanced fusion devices due to their inherent instability under these conditions. The study further reveals that liquid viscosity serves to dampen surface instability by diminishing the rate at which it initially develops.

In addition to research focusing on fusion liquid walls with free surfaces, numerous studies in the realm of two-phase magneto-hydrodynamics also contribute valuable insights. Exploring two-phase magneto-hydrodynamic (MHD) flows presents a complex challenge, and the body of research in this specific area is notably less extensive than that for single-phase MHD phenomena.

A recent study has developed a formulation that couples the time-dependent magnetic induction equation with conservation laws for multi-phase fluid flow, energy transport, and chemical species transport. This approach aims to describe state transitions like melting and solidification in systems with large property gradients [12].

In a comprehensive study by Righolt et al., the analytical solutions for one-way coupled magnetohydrodynamic free surface flow were explored [37]. The research focused on the behavior of a conductive liquid layer influenced by factors including surface tension, gravity, and Lorentz forces. These solutions were validated through numerical simulations, demonstrating their accuracy within specific ranges of Hartmann, capillary, Bond, and Reynolds numbers.

In the study by Kharicha et al. [27], the deformation of a liquid metal's free surface under electric currents is examined through both experimental and numerical approaches. The experimental setup involved a cylindrical container filled with liquid metal, with electric current applied through centrally positioned copper electrodes. The research found that at lower current densities, the interface is shifted downward due to the Lorentz force's pinch effect. Conversely, at higher current densities, the intensified flow results in further interface displacement, driven by a Bernoulli mechanism. This study is closely related to the current dissertation work. Large deformation of the liquid metal and dynamic solution of coupled Maxwell equations for moving conductors are key aspects that set this dissertation apart from other studies in the field.

1.3 Original Contributions in Present Research

Numerous studies have focused on modeling and analyzing the stability of fusion liquid walls, taking into account the complex electromagnetic forces prevalent in fusion environments. A significant portion of these studies has utilized traditional magneto-hydrodynamic equations, particularly the magnetic induction equation, which describes the evolution of the magnetic field. However, in Z-pinch scenarios where the plasma current directly interacts with the liquid metal, the MHD approach encounters challenges. Specifically, it requires the magnetic field resulting from the current as an initial condition, which may not be readily available. This difficulty arises not only from the lack of analytical solutions, even for simple geometries but also due to the unsteady nature of the current and the deformable nature of the liquid metal conductor.

Recognizing these limitations, this research work develops a numerical solver that directly solves Maxwell's equations to compute the magnetic field induced by the current. By directly solving Maxwell's equations, the need to presuppose initial magnetic fields is eliminated, considering that the magnetic fields are essentially representations of the current. This method addresses a notable gap in the literature and sets the groundwork for better simulations.

The Navier-Stokes equations are solved using the finite volume method, employing the PISO algorithm on a collocated grid with Rhie-Chow interpolation. However, Maxwell's equations in their original form contain curl operators, which, when discretized using finite volume methods, require storing variables in locations other than the cell center, such as on cell edges and vertices. Consequently, the original form with curl operators is incompatible with this finite volume framework. Alternatively, Maxwell's equations in potential form consist of Laplacian and divergence terms, which are more amenable to this computational approach.

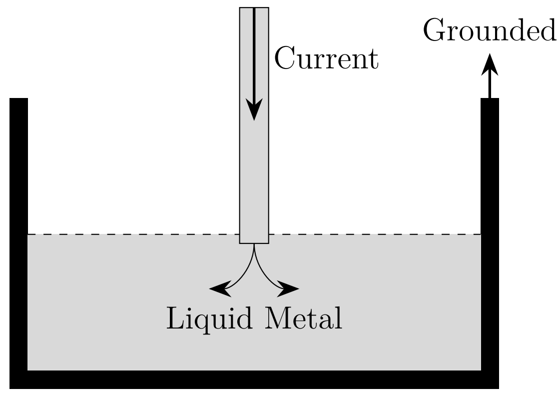

Figure 1.3: Geometry representing current carrying wire in fusion liquid wall model.

In this research work, a numerical solver is developed to model the behavior of a quiescent liquid metal layer when an external electric current is injected, by directly solving Maxwell's equation in conjunction with the Navier-Stokes equation. This serves as a representative model for plasma current flowing into liquid metal walls in Z-pinch fusion device. The goal of this research is to establish a framework for simulating free surface deformation of liquid metal wall during the fusion process. A simplified computational model is adopted for this task. In this approach, a wire, carrying an electric current, takes the place of the plasma column. The current from this wire flows into the liquid metal and exits through the cylindrical container's side wall where it's grounded. The final objectives for the solver include: casting Maxwell's equations in suitable form for the finite volume framework on a collocated grid and solving them numerically, coupling these equations with the Navier-Stokes equations to model liquid metal flows, and ultimately expanding this to cover free surface flows for a comprehensive model of liquid metal walls in Z-pinch. In this context, the following are the original contributions of this research:

1. A numerical solver for Maxwell's equations is developed by reformulating Maxwell's equations in their potential form and subsequently tailored to accurately represent the behavior of liquid metal when electric current injected into it.

2. A Maxwell-Navier-Stokes solver has been developed for single phase flow problems in the presence of electromagnetic fields. This solver was employed to investigate the interaction between fluid dynamics and electromagnetic fields.

3. The solver was adapted to accommodate non-homogeneous media with respect to electrical conductivity. This feature permits the simulation of fluids exhibiting diverse electrical properties, such as the interplay between electrically conducting and non-conducting fluids.

4. A two-phase flow solver has been implemented, designed to address momentum sources caused by currents that create spatially varying magnetic fields. By solving Maxwell's equation directly resolves the necessary spatially varying magnetic field without the need for modeling initial magnetic magnetic field.

1.4 Structure of the Dissertation

This dissertation is structured as follows:

1. Chapter 1 introduces the fusion energy, the Z-pinch method, and the emerging interest in liquid metal walls as plasma-facing components. It discusses the instability of liquid metal surfaces under fusion conditions and the aim to model these phenomena using the Maxwell-Navier-Stokes equations.

2. Chapter 2 discusses the numerical methodology, focusing on the discretization of governing partial differential equations through the finite volume method. It details the discretization of various terms, implementation of boundary conditions, and the collocated grid arrangement. Additionally, the chapter addresses specific formulations for axi-symmetric problems using wedge meshes.

3. Chapter 3 reviews Maxwell's equations in vacuum and derives the potential formulation, including its non-dimensional forms. The chapter explores the impact of displacement current in conductors and presents numerical simulations of the potential formulation of Maxwell equations. Validation is provided through test cases such as an axial current-carrying wire and a radial current-carrying hollow cylinder.

4. Chapter 4 extends the potential formulations of Maxwell's equations to moving conductors, such as liquid metals, by integrating Ohm's law for moving conductors. It introduces the Navier-Stokes equation for conducting liquids, thus establishing the Maxwell-Navier-Stokes system for single-phase flows. The chapter discusses the low magnetic Reynolds number approximation and presents numerical simulations of an axisymmetric electrically driven flow in an annular channel using the Maxwell-Navier-Stokes system.

5. Chapter 5 extends the single-phase flow equations to two-phase electrically conducting flows, presenting numerical simulations using the two-phase Maxwell-Navier-Stokes system. The chapter presents numerical simulations of a two-phase lid-driven cavity and an axisymmetric electrically driven flow in an annular channel with a free surface. Finally, the chapter concludes by presenting numerical simulations of free surface deformation in liquid metal scenarios, marking the step-by-step progression from Maxwell's equations to the two-phase Maxwell-Navier-Stokes systems essential for modeling fusion liquid walls.

Chapter 2

Numerical Method

This chapter provides a concise overview of the discretization process for the governing partial differential equations using the finite volume method based on the knowledge obtained from the resources [6, 25, 50]. The primary focus is on the discretization of various terms in the governing equations and the implementation of boundary conditions. The chosen grid arrangement adopts a collocated approach, where all flow variables are stored at cell centers. For a detailed approach, Jasak's PhD thesis [25] is recommended for further reading.

2.1 Finite Volume Discretization

Finite volume discretization uses the integral definition of differential operators [6, 17, 35], which can be obtained through Gauss's divergence theorem. The equations governing discretized system can be expressed as a matrix equation in the form of $AX = B$. Discretization yields explicit and implicit terms, with the explicit component being included in vector B and the implicit terms being included in matrix A. The algebraic equation resulting from discretization for each cell takes the following form:

$$a_P \phi_P + \sum_{N=1}^{nfaces} a_N \phi_N = b_P \tag{2.1}$$

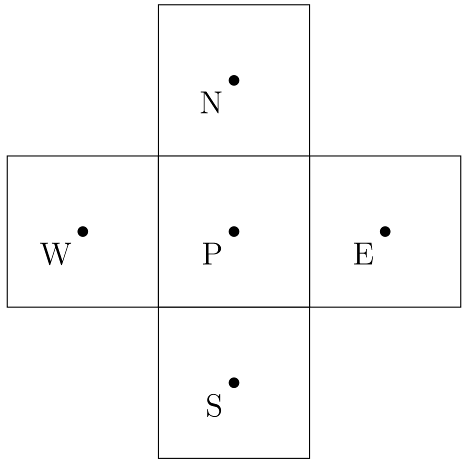

Figure 2.1: Two dimensional control volumes in finite volume discretization: Central cell represented by 'P' with neighboring cells denoted as 'E, W, N, S'. The stencil is readily extensible to 3D representation.

The equation 2.1 expresses the relationship between the values of the dependent variable ϕ in a given cell and its neighboring cells. The coefficient a_P corresponds to the central cell, while a_N represents the neighboring cells. The vector b_P contains the explicit terms resulting from the discretization. It is important to note that the discretization process involves two categories of equations: scalar and vector equations. Consequently, variables in the algebraic equations, such as a_p, a_N, and b_P, assume scalar or vector forms, respectively.

2.1.1 Integral Definition of Differential Operators

Gauss-Divergence Theorem

Divergence of vector results in scalar quantity. The integral definition of divergence operator can be written as [17, 25]

$$\nabla \cdot \mathbf{A} = \frac{1}{\Delta V} \int\limits_V \nabla \cdot \mathbf{A} \, dV$$

Here, $\mathbf{A}$ is any vector quantity and ΔV is the volume of the computational cell.

The volume integral can be converted to surface integral using Gauss divergence theorem

$$\begin{aligned}\nabla \cdot \mathbf{A} &= \frac{1}{\Delta V} \int\limits_{\partial\Omega} \mathbf{A} \cdot \mathbf{dS} \\ &= \frac{1}{\Delta V} \sum_{nfaces} \mathbf{A}_f \cdot \mathbf{S}\end{aligned}$$

Here, $\mathbf{S}$ is cell face area vector, $nfaces$ represents the number of faces of the computational cell and $\mathbf{A}_f$ is the face value of the vector $\mathbf{A}$.

Gradient Theorem

Gradient of scalar results in vector quantity. The integral definition of gradient operator can be written as

$$\nabla\phi = \frac{1}{\Delta V} \int\limits_{V} \nabla\phi \, dV$$

Here, ϕ is any scalar quantity. The volume integral can be converted to surface integral using Gradient theorem

$$\begin{aligned}\nabla\phi &= \frac{1}{\Delta V} \int\limits_{\partial\Omega} \phi \, \mathbf{dS} \\ &= \frac{1}{\Delta V} \sum_{nfaces} \phi_f \; \mathbf{S}\end{aligned}$$

Here, ϕ_f is face value of the scalar quantity ϕ.

2.1.2 Discretization of time derivative

Discretization of time derivative can be carried out by employing either the Euler or the Backward Euler method.

Euler Scheme : The Euler scheme is represented by the following equation [25, 50]:

$$\frac{\partial \phi}{\partial t} = \frac{\phi - \phi^o}{\Delta t}$$

Here, ϕ^o represents the value from the previous time step.

Applying the Euler scheme to each control volume yields the discretized algebraic equation:

$$\left(\frac{\partial \phi}{\partial t}\right)_P = \frac{1}{\Delta t}\left(\phi_P - \phi_P^o\right)$$

The coefficients and source terms for the matrix equation are then calculated as follows:

$$a_P = \frac{1}{\Delta t} \qquad a_N = 0 \qquad b_P = \frac{\phi_P^o}{\Delta t}$$

Backward Euler Scheme : The Backward Euler scheme is expressed by [25, 50]:

$$\frac{\partial \phi}{\partial t} = \frac{1}{\Delta t}\left(\frac{3}{2}\phi - 2\phi^o + \frac{1}{2}\phi^{oo}\right)$$

Here, ϕ^{oo} represents the value from the second old time step.

Applying the Backward Euler scheme to each control volume yields the discretized algebraic equation:

$$\left(\frac{\partial \phi}{\partial t}\right)_P = \frac{1}{\Delta t}\left(\frac{3}{2}\phi_P - 2\phi_P^o + \frac{1}{2}\phi_P^{oo}\right) = \frac{1}{2\Delta t}\left(3\phi_P - 4\phi_P^o + \phi_P^{oo}\right)$$

The coefficients and source terms for the matrix equation are then calculated as follows:

$$a_P = \frac{3}{2\Delta t} \qquad a_N = 0 \qquad b_P = \frac{1}{2\Delta t}\left(4\phi_P^o - \phi_P^{oo}\right)$$

2.1.3 Discretization of Laplacian

The Laplacian term is expressed as:

$$\nabla \cdot \sigma \nabla \phi = \frac{1}{\Delta V} \int\limits_V \nabla \cdot \sigma \nabla \phi \, dV$$

By applying the divergence theorem, the volume integral is transformed into a surface integral:

$$\begin{aligned} \nabla \cdot \sigma \nabla \phi &= \frac{1}{\Delta V} \int\limits_{\partial\Omega} (\sigma \nabla \phi) \cdot \mathbf{dS} \\ &= \frac{1}{\Delta V} \sum_f (\sigma \nabla \phi)_f \cdot \mathbf{S} \end{aligned}$$

Gradients must be evaluated at cell faces, which are referred to as surface normal gradients.

For orthogonal meshes, cell face gradients can be represented as [25, 50]:

$$\nabla \phi_f \cdot \mathbf{S} = |\mathbf{S}| \frac{\phi_N - \phi_P}{|\mathbf{d}|}$$

In this context, $\mathbf{d}$ represents the vector denoting the distance from the center of cell P to the center of the neighboring cell N [25]. Discretization of Laplacian operator becomes

$$\nabla \cdot \sigma \nabla \phi = \frac{1}{\Delta V} \sum_f \sigma_f |\mathbf{S}| \frac{\phi_N - \phi_P}{|\mathbf{d}|}$$

Comparing with the matrix equation and gathering the coefficients yields:

$$a_P = -\frac{1}{\Delta V}\sum_f \sigma_f \frac{|\mathbf{S}|}{|\mathbf{d}|} \qquad a_N = \frac{1}{\Delta V}\sum_f \sigma_f \frac{|\mathbf{S}|}{|\mathbf{d}|} \qquad b_P = 0$$

Dirichlet boundary condition for Laplacian : Boundary conditions must be integrated into the algebraic equation system. Dirichlet condition specifies the value of Φ at the boundary face as Φ_b. For cells with boundary faces:

$$\nabla \cdot \sigma \nabla \phi = \frac{1}{\Delta V} \sum_{innerfaces} \sigma_f |\mathbf{S}| \frac{\phi_N - \phi_P}{|\mathbf{d}|} + \frac{1}{\Delta V} \sum_{boundaryfaces} \sigma_b |\mathbf{S}| \frac{\phi_b - \phi_P}{|\mathbf{d}|}$$

The matrix coefficients of cells corresponding to boundary faces are:

$$a_P = -\frac{1}{\Delta V} \sum_{boundaryfaces} \sigma_b \frac{|\mathbf{S}|}{|\mathbf{d}|} \qquad a_N \ = 0 \qquad b_P = -\frac{1}{\Delta V} \sum_{boundaryfaces} \sigma_b \frac{|\mathbf{S}|}{|\mathbf{d}|} \phi_b$$

Von Neumann boundary condition for Laplacian : Neumann boundary condition specifies the value of the gradient of Φ normal to the boundary face [25]:

$$\hat{n} \cdot \nabla \Phi = \frac{\mathbf{S}}{|\mathbf{S}|} \cdot \nabla \Phi = g_b$$

For cells with boundary faces :

$$\nabla \cdot \sigma \nabla \phi = \frac{1}{\Delta V} \sum_{innerfaces} (\sigma \nabla \phi)_f \cdot \mathbf{S} + \frac{1}{\Delta V} \sum_{boundaryfaces} (\sigma \nabla \phi)_b \cdot \mathbf{S}$$

For the boundary face:

$$\nabla \phi \cdot \mathbf{S} = |\mathbf{S}| g_b$$

Then the equation can be written as :

$$\nabla \cdot \sigma \nabla \phi = \frac{1}{\Delta V} \sum_{innerfaces} (\sigma \nabla \phi)_f \cdot \mathbf{S} + \frac{1}{\Delta V} \sum_{boundaryfaces} \sigma_b |\mathbf{S}| g_b$$

The matrix coefficients of cells corresponding to boundary faces are:

$$a_P = 0 \quad a_N \quad = 0 \quad b_P = -\frac{1}{\Delta V} \sum_{boundaryfaces} \sigma_b |\mathbf{S}| g_b$$

2.1.4 Discretization of Divergence Term

The Divergence term is expressed as:

$$\nabla \cdot (\rho \mathbf{U} \phi) = \frac{1}{\Delta V} \int_V \nabla \cdot (\rho \mathbf{U} \phi) \; dV$$

By applying the divergence theorem, the volume integral is transformed into a surface integral:

$$\begin{aligned} \nabla \cdot (\rho \mathbf{U} \phi) &= \frac{1}{\Delta V} \int_{\partial \Omega} (\rho \mathbf{U} \phi) \cdot \mathbf{dS} = \frac{1}{\Delta V} \sum_f (\rho \mathbf{U} \phi)_f \cdot \mathbf{S} \\ &= \frac{1}{\Delta V} \sum_f \phi_f (\rho \mathbf{U})_f \cdot \mathbf{S} = \frac{1}{\Delta V} \sum_f \phi_f \, F \end{aligned}$$

The quantity $F = (\rho \mathbf{U})_f \cdot \mathbf{S}$ is called mass flux [25, 50]. The face value ϕ_f is calculated using convection differencing schemes.

Convection differencing schemes :

The face value of ϕ is calculated based on the cell center value of ϕ using convection differencing schemes. Two different schemes and their implementation is illustrated next. For other schemes one can refer to [6, 25].

Linear scheme :

The linear scheme [25, 50] is given by

$$\phi_f = f_x\,\phi_P + (1 - f_x)\,\phi_N$$

Here f_x is the interpolation factor [25]. For uniform grid, $f_x = 0.5$.

Using linear scheme, the divergence term becomes,

$$\begin{aligned}\nabla \cdot (\rho \mathbf{U} \phi) &= \frac{1}{\Delta V} \sum_f \phi_f\, F \\ &= \frac{1}{\Delta V} \sum_f \left(f_x\,\phi_P + (1 - f_x)\,\phi_N\right)\, F\end{aligned}$$

Upon comparing with the matrix equation and gathering the coefficients, one obtains:

$$a_P = \frac{1}{\Delta V} \sum_f f_x F \qquad a_N \;\; = \frac{1}{\Delta V} \sum_f (1 - f_x) F \qquad b_P = 0$$

For fully explicit scheme,

$$a_P = 0 \qquad a_N \;\; = 0 \qquad b_P = -\frac{1}{\Delta V} \sum_f \left(f_x\,\phi_P + (1 - f_x)\,\phi_N\right)\, F$$

Note that this linear scheme is unstable in convection dominated flows.

Upwind scheme :

The Upwind scheme [25, 50] is given by

$$\phi_f = \phi_P \quad \mathrm{F} \geq 0$$

$$\phi_f = \phi_N \quad \mathrm{F} < 0$$

The two equations can be combined as [50] $\phi_f = \max(\text{sign(F)},0)\,\phi_P + (1\text{-}\max(\text{sign(F)},0))\,\phi_N$

$$\begin{aligned}\nabla\cdot(\rho\mathbf{U}\phi) &= \frac{1}{\Delta V}\sum_f \phi_f\,F\\ &= \frac{1}{\Delta V}\sum_f \left(\max(\text{sign(F)},0)\,\phi_P + (1\text{-}\max(\text{sign(F)},0))\,\phi_N\right)\,F\end{aligned}$$

The coefficients are given by:

$$a_P = \frac{1}{\Delta V}\sum_f \max(\text{sign(F)},0)F \qquad a_N = \frac{1}{\Delta V}\sum_f (1\text{-}\max(\text{sign(F)},0))F \qquad b_P = 0$$

2.1.5 Computing Boundary values:

Once the matrix coefficients are computed, the matrix is assembled and solved using a linear solver to obtain the cell center values. The boundary values are then determined based on the specified boundary conditions. The Dirichlet boundary condition directly provides the values at the boundary cells. For a Von Neumann boundary condition, the boundary values are computed utilizing the Taylor Series expansion method [25, 50].

$$\phi_b = \phi_P + \mathbf{d}_n.(\nabla\phi)_b$$

In this equation, $\mathbf{d}_n$ is the normal distance vector from the cell center to the boundary [25].

$$\phi_b = \phi_P + |\mathbf{d}_n|g_b$$

Here, $g_b = \hat{n}\cdot\nabla\Phi$. For zero-normal gradient boundary condition ($g_b = 0$):

$$\phi_b = \phi_P$$

2.1.6 Discretization of Gradient :

In this research work, the gradient term is handled explicitly, which means that it is evaluated based on the previous time step values of the variables.

$$\nabla\phi = \frac{1}{\Delta V}\int_V \nabla\phi \, dV$$

By applying the divergence theorem, the volume integral is converted to a surface integral:

$$\begin{aligned}\nabla\phi &= \frac{1}{\Delta V}\int_{\partial\Omega} \phi \, \mathbf{dS} \\ &= \frac{1}{\Delta V}\sum_{nfaces} \phi_f \ \mathbf{S}\end{aligned}$$

When comparing with the matrix equation and collecting the coefficients:

$$a_P = 0 \quad a_N \quad = 0 \quad b_P = -\frac{1}{\Delta V}\sum_f \phi_f \ \mathbf{S}$$

For explicit terms, boundary values are already known from previous time step, eliminating the need to handle boundary conditions separately.

2.2 Wedge Formulation for Axi-Symmetric Problems

Axially symmetric simulations in wedge meshes are particularly well-suited for problems where the fields of interest do not change in the circumferential direction [50]. This means that the variables being modeled remain constant as the system rotates around its central axis. In this research work, the wedge formulation is employed to address and solve axially symmetric cases.

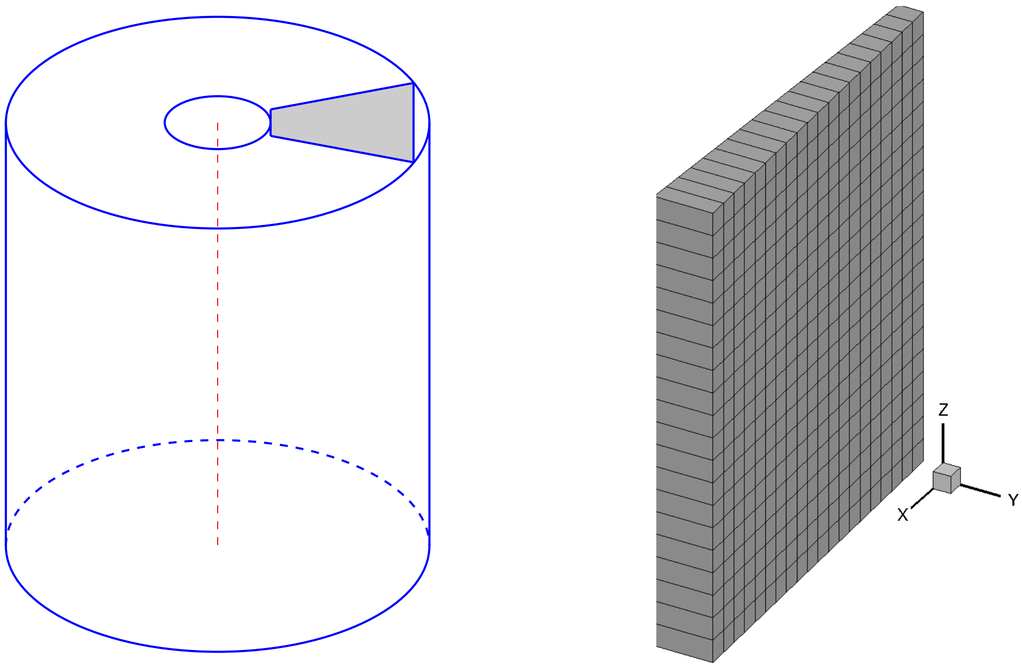

(a) Real Physical Domain

(b) Computational Domain

Figure 2.2: Computational domain for axially symmetric simulations using wedge mesh [50].

Axially symmetric simulations in a wedge mesh [50] use a computational domain that is divided into a series of wedges, each representing a small angle of rotation around the central axis. This approach allows the physical system to be modeled in a 2D plane, reducing the computational requirements compared to 3D simulations. One of the primary advantages of using a wedge mesh technique for axially symmetric simulations is that it allows for the simulations to be carried out in a Cartesian coordinate system.

The wedge formulation for simulations exhibiting axial symmetry is implemented by shaping the system's geometry into a slender wedge [50]. This wedge is characterized by a narrow angle, generally less than 5°, and has a thickness corresponding to a single cell. An example of this is shown in Figure 2.2 . The coordinates used in the simulation are x, y, and z, which correspond to r, θ, and z, respectively.

Chapter 3

Maxwell's Equations

3.1 Maxwell Equations

Maxwell's equations are a fundamental set of equations that describe the behavior of electric and magnetic fields in space, and how they relate to the distribution of electric charges and currents. These equations explain the complex relationship between electric and magnetic fields, and how they are interdependent. They were first developed by James Clerk Maxwell in the 19^{th} century and are now considered to be a cornerstone of modern physics and electrical engineering. A concise summary of Maxwell's equations is presented in this chapter based on the textbooks [11, 16, 24]. For a detailed review, sources [11, 16, 24] are recommended for further reading.

Maxwell equations explain how electric fields and magnetic fields are created. The equations describe two kinds of electric fields [11]: one created by electric charges and the other produced by a changing magnetic field. Likewise, there are two kinds of magnetic fields: one generated by a electric current and another produced by a changing electric field.

Gauss's Law for Electric Fields

Gauss's law for electric fields is a fundamental law of electromagnetism that relates the behavior of electric fields to the distribution of electric charges in space.

Gauss's law describes how the electric field emanating from a charge is related to the charge itself, and how this electric field is affected by other charges in the vicinity. In mathematical terms, Gauss's law for electric fields can be expressed as the divergence of the electric field being proportional to the electric charge density at a given point:

$$\nabla \cdot \mathbf{E} = \frac{\rho_c}{\epsilon_o}$$

In other words, the electric field is stronger in regions where there is a higher charge density. Conversely, in regions where there is no electric charge, the divergence of the electric field is zero.

$$\nabla \cdot \mathbf{E} = 0$$

Faraday's Law of Induction

Faraday's law of induction describes the relationship between a changing magnetic field and the production of an electric field. It is named after Michael Faraday, an English physicist who discovered this phenomenon during the 19th century. According to the law, a circulating electric field is generated by a magnetic field that is changing over time. This is mathematically expressed as follows:

$$\nabla \times \mathbf{E} = -\frac{\partial \mathbf{B}}{\partial t}$$

The curl of the electric field vector equals the negative partial derivative of the magnetic field vector with respect to time. In simpler terms, Faraday's law of induction states that a changing magnetic field induces an electric field.

Gauss's Law for Magnetic Fields

Gauss's law for magnetic fields states that the divergence of the magnetic field vector is always zero.

Gauss's law can be expressed mathematically as:

$$\nabla \cdot \mathbf{B} = 0$$

This equation implies that the magnetic field lines are always continuous and do not have any sources or sinks (i.e., magnetic monopoles), unlike electric field lines which originate from positive charges and terminate at negative charges.

The Ampere-Maxwell Law

The Ampere-Maxwell law relates the curl of the magnetic field vector to the sources of the magnetic field, which are steady electric currents and changing electric fields.

Mathematically, the equation can be expressed as:

$$\nabla \times \mathbf{B} = \mu_0 \mathbf{J} + \mu_0 \epsilon_0 \frac{\partial \mathbf{E}}{\partial t}$$

The first term on the right-hand side of the equation represents the contribution to the magnetic field from a steady current, while the second term represents the contribution from a changing electric field. The latter term is known as displacement current, and it was added to Ampere's law by Maxwell to account for the behavior of electric fields that change in time.

3.2 Maxwell Equations in Matter

Maxwell's equations describe the behavior of electromagnetic fields in both free space and matter. However, when we consider matter, we must modify Gauss's law and the Ampere-Maxwell law to include the effects of bound charges and currents [11, 16]. Bound charges are those that are fixed in a material, while bound currents arise due to the motion of these bound charges. The modified equations account for both bound and free charges and currents. In practice, it is often difficult to determine bound charges and currents, so it is more convenient to work with the modified equations in terms of free charges and currents.

Gauss's Law for Electric Fields

The modified Gauss's law for electric fields states that the divergence of the electric displacement field is equal to the free charge density.

$$\nabla \cdot \mathbf{D} = \rho_f$$

In the absence of free charges, the divergence of the electric displacement field is zero.

$$\nabla \cdot \mathbf{D} = 0$$

Faraday's Law of Induction

Faraday's law of induction remains unchanged in the presence of matter.

$$\nabla \times \mathbf{E} = -\frac{\partial \mathbf{B}}{\partial t}$$

Gauss's Law for Magnetic Fields

Gauss's law for magnetic fields remains unchanged in the presence of matter.

$$\nabla \cdot \mathbf{B} = 0$$

The Ampere-Maxwell Law

The Ampere-Maxwell law in matter includes the effects of both free and bound currents, as well as the time derivative of the electric displacement field.

$$\nabla \times \mathbf{H} = \mathbf{J}_f + \frac{\partial \mathbf{D}}{\partial t}$$

Ampere-Maxwell law states that the curl of the magnetic field intensity is equal to the sum of the free current density and the time derivative of the electric displacement field.

These modified equations provide a more complete description of the behavior of electromagnetic fields in matter.

3.3 Constitutive Relations

The constitutive relations describe how electric and magnetic fields are related to other quantities. Specifically, they relate the electric displacement field to the electric field, and the magnetic flux density to the magnetic field intensity.

The electric displacement field is related to the electric field by a quantity called the electric permittivity, which is the product of the permittivity of free space and the relative permittivity of the material.

$$\mathbf{D} = \epsilon\mathbf{E}$$

where $\epsilon = \epsilon_0\,\epsilon_r$

The magnetic flux density is related to the magnetic field intensity by a quantity called the magnetic permeability, which is the product of the permeability of free space and the relative permeability of the material.

$$\mathbf{B} = \mu\mathbf{H}$$

where $\mu = \mu_0\,\mu_r$

Ohm's law relates the free current density to the electric field, where the proportionality constant is called the conductivity.

$$\mathbf{J}_f = \sigma\mathbf{E}$$

3.4 Ohm's law for Moving Conductors

For moving conductors, Ohm's law is modified to include the additional term, which is the cross product of the velocity of the conductor and the magnetic field.

$$\mathbf{J} = \sigma(\mathbf{E} + \mathbf{U} \times \mathbf{B})$$

3.5 Continuity Equation

The continuity equation [16, 24] is a mathematical expression that describes the conservation of charge in a given region. It states that the rate of change of charge density (ρ_c) within a volume, plus the net current density ($\mathbf{J}$) flowing out of that volume, must be equal to zero.

Mathematically, the continuity equation is formulated as:

$$\nabla \cdot \mathbf{J} + \frac{\partial \rho_c}{\partial t} = 0$$

In cases where there is no net flow of charge into or out of the volume, the total charge within a closed volume remains constant, leading to the simplified form:

$$\nabla \cdot \mathbf{J} = 0$$

Deriving the continuity equation [16, 24] requires the use of two out of the four Maxwell's equations: Gauss's law for electric fields and Ampere's law with Maxwell's addition.

Starting with Ampere's law:

$$\nabla \times \mathbf{B} = \mu_0 \mathbf{J} + \mu_0 \epsilon_0 \frac{\partial \mathbf{E}}{\partial t}$$

By taking the divergence of the above equation, one finds:

$$\nabla \cdot (\nabla \times \mathbf{B}) = \mu_0 \nabla \cdot \mathbf{J} + \mu_0 \epsilon_0 \frac{\partial (\nabla \cdot \mathbf{E})}{\partial t}$$

Note that the divergence of the curl is always zero. By Gauss's law, $\nabla \cdot \mathbf{E} = 0$, one arrives at the conclusion:

$$\nabla \cdot \mathbf{J} = 0$$

For fields in matter, a similar derivation can be performed. Consider Ampere's law in matter:

$$\nabla \times \mathbf{H} = \mathbf{J}_f + \frac{\partial \mathbf{D}}{\partial t}$$

Taking the divergence of the above equation, one obtains:

$$\nabla \cdot (\nabla \times \mathbf{H}) = \nabla \cdot \mathbf{J}_f + \frac{\partial(\nabla \cdot \mathbf{D})}{\partial t}$$

Recall that the divergence of the curl also vanishes in this case. Utilizing Gauss's law for fields in matter, $\nabla \cdot \mathbf{D} = 0$, one can express:

$$\nabla \cdot \mathbf{J}_f = 0$$

Summary of equations:

In terms of total current density,

$$\nabla \cdot \mathbf{J} = 0$$

In terms of free current density,

$$\nabla \cdot \mathbf{J}_f = 0$$

3.6 Displacement Current in Conductors

In conductors, the displacement current, which is an addition made by Maxwell to Ampere's law, is usually insignificant compared to the conduction current [29]. This is because the conduction current, which is related to the conductivity of the material, is much larger than the permittivity, which is related to the displacement current.

Consider the Ampere-Maxwell law

$$\nabla \times \mathbf{B} = \mu_0 \mathbf{J} + \mu_0 \epsilon_o \frac{\partial \mathbf{E}}{\partial t}$$

In the above equation, the conduction current **J** is given by Ohm's law,

$$\mathbf{J}_c = \mathbf{J} = \sigma \mathbf{E}$$

The displacement current in frequency domain is

$$\mathbf{J}_d = \epsilon_o \frac{\partial \mathbf{E}}{\partial t} = i\omega\epsilon_o \mathbf{E} = i2\pi f \epsilon_o \mathbf{E}$$

The ratio of magnitude of conduction current to displacement current is

$$\frac{J_c}{J_d} = \left| \frac{\sigma \mathbf{E}}{i2\pi f \epsilon_o \mathbf{E}} \right| = \frac{\sigma}{2\pi f \epsilon_o}$$

The frequency at which the conduction current becomes comparable to the displacement current is

$$f = \frac{\sigma}{2\pi\epsilon_o}$$

For copper,

$$f = \frac{5.8 \times 10^7}{2 \times \pi \times 8.854 \times 10^{-12}} = 1.0425 \times 10^{18} Hz$$

In this work, the displacement current is neglected, so the derived governing equations are suitable for low frequencies, significantly below 1.0×10^{18} Hz. However, it is worth noting that 1.0×10^{18} Hz is a tremendously large number, with most practical applications falling well beneath this frequency. This simplifies the Ampere-Maxwell law in conductors and allows it to be expressed in terms of current density.

The simplified form of the Ampere-Maxwell law is given by the equation:

$$\nabla \times \mathbf{B} = \mu_0 \mathbf{J}$$

In terms of free current density, the law is expressed as:

$$\nabla \times \mathbf{H} = \mathbf{J}_f$$

3.7 Non Dimensional Form of Maxwell Equations

The non-dimensional version of the equations are derived to encounter problems that involve significant differences in spatial and temporal scales, such as those that arise when large spatial dimensions coexist with small temporal dimensions, or when small spatial dimensions coexist with large temporal dimensions. In these cases, non-dimensionalization enables us to express the equations in a dimensionless form that reveals the underlying physics of the system, and identify the relevant non-dimensional parameters that govern its behavior.

The non-dimensional form of the Maxwell equations is derived by introducing length scale L_o, time scale t_o, magnetic field scale B_o, and electric conductivity scale σ_o. Initially, E_o serves as the electric field scale, with the intention to update this scale subsequently. Non-dimensional quantities ∇', t', $\mathbf{B}'$, $\mathbf{E}'$, σ' are employed to correspond to ∇, t, $\mathbf{B}$, $\mathbf{E}$, σ respectively.

The relationships among scale factors, dimensional and non-dimensional quantities is given as: $\nabla' = \dfrac{\nabla}{\nabla_o}$, $t' = \dfrac{t}{t_o}$, $\mathbf{B}' = \dfrac{\mathbf{B}}{B_o}$, $\mathbf{E}' = \dfrac{\mathbf{E}}{E_o}$, $\sigma' = \dfrac{\sigma}{\sigma_o}$.

Consider the Maxwell equations by neglecting the displacement current.

$$\nabla \cdot \mathbf{E} = 0$$

$$\nabla \cdot \mathbf{B} = 0$$

$$\nabla \times \mathbf{E} = -\frac{\partial \mathbf{B}}{\partial t}$$

$$\nabla \times \mathbf{B} = \mu_0 \sigma \mathbf{E}$$

Where the Ohm's law ($\mathbf{J} = \sigma \mathbf{E}$) for current density is applied.

In terms of non-dimensional variables and scale factors, Faraday's law in the Maxwell equation becomes:

$$\left(\frac{1}{L_o} E_o\right) \nabla' \times \mathbf{E}' = -\left(\frac{B_o}{t_o}\right) \frac{\partial \mathbf{B}'}{\partial t'}$$

To make this equation non-dimensional, set:

$$\frac{E_o}{L_o} = \frac{B_o}{t_o}$$

The scale for E_o is chosen as:

$$E_o = \frac{B_o L_o}{t_o}$$

This leads to the non-dimensional Faraday's law:

$$\nabla' \times \mathbf{E}' = -\frac{\partial \mathbf{B}'}{\partial t'}$$

Ampere's law becomes

$$\left(\frac{1}{L_o}\ B_o\right) \nabla\,' \times \mathbf{B}\,' = \mu_0\ \left(\sigma_o \frac{B_o L_o}{t_o}\right) \sigma\,' \,\mathbf{E}\,'$$

$$\nabla\,' \times \mathbf{B}\,' = \left(\frac{\mu_0\, \sigma_o L_o^2}{t_o}\right) \sigma\,' \,\mathbf{E}\,'$$

The term on the bracket is non-dimensional.

The non-dimensional Ampere's law can be expressed as: $\nabla' \times \mathbf{B}' = R_m \sigma' \mathbf{E}'$.

where R_m is the non-dimensional magnetic Reynolds number and is defined as:

$$R_m = \frac{\mu_0 \sigma_o L_o^2}{t_o}$$

The procedure for remaining Maxwell equations are straightforward. Gauss laws for electric field becomes

$$\left(\frac{1}{L_o}\ E_o\right) \nabla' \cdot \mathbf{E}' = 0$$

Hence the non-dimensional form of Gauss law for electric field becomes, $\nabla' \cdot \mathbf{E}' = 0$.

Gauss laws for magnetic field becomes

$$\left(\frac{1}{L_o}\ B_o\right) \nabla' \cdot \mathbf{B}' = 0$$

Hence the non-dimensional form of Gauss law for magnetic field becomes

$$\nabla' \cdot \mathbf{B}' = 0$$

Summary of equations:

$$\nabla' \cdot \mathbf{E}' = 0$$

$$\nabla' \cdot \mathbf{B}' = 0$$

$$\nabla' \times \mathbf{E}' = -\frac{\partial \mathbf{B}'}{\partial t'}$$

$$\nabla' \times \mathbf{B}' = R_m\, \sigma'\, \mathbf{E}'$$

Summary of scale factors and non-dimensional numbers:

$$E_o = \frac{B_o L_o}{t_o}$$

$$R_m = \frac{\mu_0 \sigma_o L_o^2}{t_o}$$

3.8 Potential Formulation of Maxwell Equations

The potential formulation of Maxwell's equations is an alternative representation of these equations that expresses electromagnetic fields in terms of scalar and vector potentials instead of electric and magnetic fields. This approach often simplifies the application of Maxwell's equations in various contexts. For example, when using a finite volume framework, directly discretizing Maxwell's equations containing curl operators necessitates storing variables in locations other than cell centers, such as on cell edges. However, with the current finite volume framework employing a collocated approach and the Rhie-Chow interpolation for Navier-Stokes equation, variables are stored at cell centers.

By recasting Maxwell's equations using the potential formulation, the curl operator is eliminated, allowing for the continued use of the collocated approach and simplifying the overall process. The potential formulation of Maxwell's equations is discussed in detail in the textbooks [16, 24]. For the sake of completeness, it is reiterated here, drawing from these sources. The potential formulation of Maxwell's equations is derived by introducing the scalar potential (ϕ) and the vector potential ($\mathbf{A}$).

For any vector, divergence of curl is zero.

$$\nabla \cdot (\nabla \times \mathbf{A}) = 0$$

From Gauss's law, $\mathbf{B}$ is divergence free

$$\nabla \cdot \mathbf{B} = 0$$

From the last two equations, $\mathbf{B}$ can be expressed as curl of some vector quantity.

$$\mathbf{B} = \nabla \times \mathbf{A}$$

Here $\mathbf{A}$ is called magnetic vector potential.

Recall that Faraday's law is given by

$$\nabla \times \mathbf{E} = -\frac{\partial \mathbf{B}}{\partial t}$$

In terms of magnetic vector potential, the equation becomes

$$\nabla \times \mathbf{E} = -\frac{\partial (\nabla \times \mathbf{A})}{\partial t}$$

Changing the order of differentiation yields:

$$\nabla \times \mathbf{E} = -\nabla \times \frac{\partial \mathbf{A}}{\partial t}$$

Simplifying,

$$\nabla \times \mathbf{E} + \nabla \times \frac{\partial \mathbf{A}}{\partial t} = 0$$

Simplifying further,

$$\nabla \times \left(\mathbf{E} + \frac{\partial \mathbf{A}}{\partial t} \right) = 0$$

If a curl of quantity is zero, it can be written as the gradient of scalar field. Therefore, it is possible to write:

$$\mathbf{E} + \frac{\partial \mathbf{A}}{\partial t} = -\nabla\Phi$$

Hence the expression for electric field is given by

$$\mathbf{E} = -\nabla\Phi - \frac{\partial \mathbf{A}}{\partial t}$$

It is important to emphasize that the definitions of the potentials inherently incorporate Gauss's law for magnetic fields and Faraday's law [16, 24]. Consequently, by formulating the potentials in this way, two out of the four Maxwell equations are intrinsically satisfied.

Summary of equations:

$$\mathbf{B} = \nabla \times \mathbf{A}$$

For unsteady fields,

$$\mathbf{E} = -\nabla\Phi - \frac{\partial \mathbf{A}}{\partial t}$$

For steady fields,

$$\mathbf{E} = -\nabla\Phi$$

3.8.1 Evolution Equation for Electric Scalar Potential

In the previous section, the expression for the electric field was derived in terms of electric and magnetic potentials, particularly for time-varying fields.

$$\mathbf{E} = -\nabla\Phi - \frac{\partial \mathbf{A}}{\partial t}$$

By multiplying the equation with the conductivity, σ, we obtain:

$$\sigma\mathbf{E} = -\sigma\nabla\Phi - \sigma\frac{\partial\mathbf{A}}{\partial t}$$

Now, by applying Ohm's law, one can write $\mathbf{J} = \sigma\mathbf{E}$.

$$\mathbf{J} = -\sigma\nabla\Phi - \sigma\frac{\partial\mathbf{A}}{\partial t}$$

Taking the divergence of the previous equation, the following is obtained:

$$\nabla\cdot\mathbf{J} = -\nabla\cdot\sigma\nabla\Phi - \nabla\cdot\left(\sigma\frac{\partial\mathbf{A}}{\partial t}\right)$$

As a consequence of the continuity equation, which dictates that the divergence of the current density must vanish ($\nabla\cdot\mathbf{J} = 0$), the derivation proceeds as follows:

$$\nabla\cdot\sigma\nabla\Phi + \nabla\cdot\left(\sigma\frac{\partial\mathbf{A}}{\partial t}\right) = 0$$

Note that the continuity equation satisfies Gauss's law for electric fields. In the case of steady fields, which exhibit no time dependence, the governing equation becomes more straightforward:

$$\nabla\cdot\sigma\nabla\Phi = 0$$

Or, in the case of constant conductivity, the equation can be further simplified as:

$$\nabla\cdot\nabla\Phi + \frac{\partial(\nabla\cdot\mathbf{A})}{\partial t} = 0$$

It is important to note that only the curl of $\mathbf{A}$ is defined in terms of $\mathbf{B}$.

According to Helmholtz's theorem, both the divergence and curl of $\mathbf{A}$ must be specified in order to determine $\mathbf{A}$. The specification of $\nabla \cdot \mathbf{A}$ is referred to as the choice of gauge [16, 24]. This choice is possible due to the gauge invariance of Maxwell's equations, which means that the physical observables (electric and magnetic fields) remain unchanged under a gauge transformation. There are several common gauge choices used in electrodynamics, each with its advantages and applications. In this context, the Coulomb gauge is employed, where the divergence of the vector potential is set to zero.

$$\nabla \cdot \mathbf{A} = 0$$

It leads to a simplified expression for the scalar potential, satisfying Laplace's equation.

$$\nabla \cdot \nabla \Phi = 0$$

Summary of equations:

For unsteady fields,

$$\nabla \cdot \sigma \nabla \Phi + \nabla \cdot \left(\sigma \frac{\partial \mathbf{A}}{\partial t} \right) = 0$$

For steady fields,

$$\nabla \cdot \sigma \nabla \Phi = 0$$

3.8.2 Evolution Equation for Magnetic Vector Potential

In this section, the evolution equation for the magnetic vector potential is derived. Starting with Ampere's law:

$$\nabla \times \mathbf{B} = \mu_0 \mathbf{J}$$

Using the definition of magnetic vector potential, $\mathbf{B} = \nabla \times \mathbf{A}$, yields:

$$\nabla \times (\nabla \times \mathbf{A}) = \mu_0 \mathbf{J}$$

Applying the vector identity A.4:

$$\nabla(\nabla \cdot \mathbf{A}) - \nabla \cdot \nabla \mathbf{A} = \mu_0 \mathbf{J}$$

Imposing the Coulomb gauge ($\nabla \cdot \mathbf{A} = 0$), results in Poisson equation for vector potential.

$$\nabla \cdot \nabla \mathbf{A} = -\mu_0 \mathbf{J}$$

Employing Ohm's law ($\mathbf{J} = \sigma \mathbf{E}$), we have:

$$\nabla \cdot \nabla \mathbf{A} = -\mu_0 \sigma \mathbf{E}$$

Substituting the expression for the electric field in terms of electric potential for time-varying fields:

$$\nabla \cdot \nabla \mathbf{A} = -\mu_0 \sigma \left(-\nabla \Phi - \frac{\partial \mathbf{A}}{\partial t} \right)$$

Simplifying and rearranging:

$$\mu_0 \sigma \frac{\partial \mathbf{A}}{\partial t} + \mu_0 \sigma \nabla \Phi - \nabla \cdot \nabla \mathbf{A} = 0$$

Defining the current due to the potential as $\mathbf{J}_\Phi = -\sigma \nabla \Phi$, the governing equation becomes:

$$\mu_0 \sigma \frac{\partial \mathbf{A}}{\partial t} - \mu_0 \mathbf{J}_\Phi - \nabla \cdot \nabla \mathbf{A} = 0$$

For steady fields without time dependence:

$$\nabla \cdot \nabla \mathbf{A} + \mu_0 \mathbf{J}_{\Phi} = 0$$

It is worth noting that this magnetic vector potential equation satisfies Ampere's law.

Summary of equations :

For unsteady fields,

$$\mu_0 \sigma \frac{\partial \mathbf{A}}{\partial t} + \mu_0 \sigma \nabla \Phi - \nabla \cdot \nabla \mathbf{A} = 0$$

For steady fields,

$$\nabla \cdot \nabla \mathbf{A} = \mu_0 \sigma \nabla \Phi$$

3.8.3 Non-dimensional form of Potential Formulation of Maxwell Equations for Steady Fields

The governing equation used for steady fields are

$$\nabla \cdot \sigma \nabla \Phi = 0$$

$$\nabla \cdot \nabla \mathbf{A} - \mu_0 \sigma \nabla \Phi = 0$$

The non-dimensional form of the governing equations is derived by introducing length scale L_o, electric conductivity scale be σ_o, electric potential scale be Φ_o and magnetic vector potential scale be A_o. Non-dimensional quantities ∇', σ', Φ', $\mathbf{A}'$ are employed to correspond to ∇, σ, Φ, $\mathbf{A}$. The relationships among scale factors, dimensional and non-dimensional quantities is given as: $\nabla' = \dfrac{\nabla}{\nabla_o}$, $\Phi' = \dfrac{\Phi}{\Phi_o}$, $\mathbf{A}' = \dfrac{\mathbf{A}}{A_o}$, $\sigma' = \dfrac{\sigma}{\sigma_o}$.

By expressing dimensional quantities in terms of non-dimensional quantities and scale factors, the electric scalar potential equation can be rewritten as:

$$\left(\frac{1}{L_o}\,\sigma_o\,\frac{1}{L_o}\,\Phi_o\right)\nabla'\cdot\sigma'\nabla'\Phi' = 0$$

This simplifies to:

$$\nabla'\cdot\sigma'\nabla'\Phi' = 0$$

Similarly, the magnetic vector potential can be expressed as:

$$\left(\frac{1}{L_o}\frac{1}{L_o}A_o\right)\nabla'\cdot\nabla'\mathbf{A}' - \left(\mu_0\sigma_o\frac{1}{L_o}\Phi_o\right)\sigma'\nabla'\Phi' = 0$$

Dividing the above equation by $\left(\frac{A_o}{L_o^2}\right)$,

$$\nabla'\cdot\nabla'\mathbf{A}' - \left(\frac{\mu_0\sigma_o L_o\Phi_o}{A_o}\right)\sigma'\nabla'\Phi' = 0$$

If the above equation has to be non-dimensional, then $A_o = \mu_0\sigma_o L_o\Phi_o$.

$$\nabla'\cdot\nabla'\mathbf{A}' - \sigma'\nabla'\Phi' = 0$$

Similarly, scale factors for associated parameters like current density and magnetic field can be derived.

For current density $\mathbf{J}_\phi$,

$$J_o\mathbf{J}' = -\left(\sigma_o\frac{1}{L_o}\Phi_o\right)\sigma'\nabla'\Phi'$$

Scale factor for current density is then,

$$J_o = \frac{\sigma_o \, \Phi_o}{L_o}$$

The non-dimensional current density is

$$\mathbf{J}' = -\sigma' \nabla' \Phi'$$

For magnetic field,

$$B_o \, \mathbf{B}' = \left(\frac{1}{L_o} A_o \right) \nabla' \times \mathbf{A}'$$

Scale factor for magnetic field is then,

$$B_o = \frac{A_o}{L_o}$$

The non-dimensional magnetic field is

$$\mathbf{B}' = \nabla' \times \mathbf{A}'$$

Summary of equations:

$$\nabla' \cdot \sigma' \nabla' \Phi' = 0$$

$$\nabla' \cdot \nabla' \mathbf{A}' - \sigma' \nabla' \Phi' = 0$$

$$\mathbf{J}' = -\sigma' \nabla' \Phi'$$

$$\mathbf{B}' = \nabla' \times \mathbf{A}'$$

Summary of scale factors:

$$A_o = \mu_0 \sigma_o L_o \Phi_o$$

$$J_o = \frac{\sigma_o \Phi_o}{L_o}$$

$$B_o = \frac{A_o}{L_o}$$

3.8.4 Non-dimensional form of Potential Formulation of Maxwell Equations for Unsteady Fields

The evolution equations for electric potential and magnetic vector potential governing time dependent fields are given by

$$\nabla \cdot \sigma \nabla \Phi = 0$$

$$\mu_0 \sigma \frac{\partial \mathbf{A}}{\partial t} + \mu_0 \sigma \nabla \Phi - \nabla \cdot \nabla \mathbf{A} = 0$$

In this research, the transient term in the electric potential equation is omitted. The only places where conductivity varies are the two-phase flow scenarios involving liquid metal, which has some conductivity, and air, with zero conductivity. The primary interest is in the magnetic field and current density within the liquid metal. Given this context, conductivity is generally considered constant. However, the conductivity (σ) is retained in the first equation to ensure that current flows exclusively within the conducting region for numerical reasons.

The non-dimensional form of the governing equations is derived by introducing length scale L_o, time scale t_o, electric conductivity scale be σ_o, electric potential scale be Φ_o and magnetic vector potential scale be A_o.

Non-dimensional quantities ∇', t', σ', Φ', $\mathbf{A}'$ are employed to correspond to ∇, t, σ, Φ, $\mathbf{A}$. The relationships among scale factors, dimensional and non-dimensional quantities is given as: $\nabla' = \dfrac{\nabla}{\nabla_o}$, $t' = \dfrac{t}{t_o}$, $\Phi' = \dfrac{\Phi}{\Phi_o}$, $\mathbf{A}' = \dfrac{\mathbf{A}}{A_o}$, $\sigma' = \dfrac{\sigma}{\sigma_o}$. By expressing dimensional quantities in terms of non-dimensional quantities and scale factors, the electric scalar potential equation can be rewritten as:

$$\left(\frac{1}{L_o}\,\sigma_o\,\frac{1}{L_o}\,\Phi_o\right)\nabla'\cdot\sigma'\nabla'\Phi' = 0$$

This simplifies to:

$$\nabla'\cdot\sigma'\nabla'\Phi' = 0$$

Similarly, the magnetic vector potential equation for unsteady fields can be expressed in terms of non-dimensional quantities and scale factors:

$$\left(\mu_0\sigma_o\frac{A_o}{t_o}\right)\sigma'\frac{\partial\mathbf{A}'}{\partial t'} + \left(\mu_0\sigma_o\frac{1}{L_o}\Phi_o\right)\sigma'\nabla'\Phi' - \left(\frac{1}{L_o}\frac{1}{L_o}A_o\right)\nabla'\cdot\nabla'\mathbf{A}' = 0$$

Multiply the whole equation, by $\dfrac{L_o^2}{A_o}$ results in:

$$\left(\frac{\mu_0\sigma_o L_o^2}{t_o}\right)\sigma'\frac{\partial\mathbf{A}'}{\partial t'} + \left(\frac{\mu_0\sigma_o L_o\Phi_o}{A_o}\right)\sigma'\nabla'\Phi' - \nabla'\cdot\nabla'\mathbf{A}' = 0$$

Choose the scale factor for magnetic vector potential as $A_o = \mu_0\sigma_o L_o\Phi_o$ yields:

$$\left(\frac{\mu_0\sigma_o L_o^2}{t_o}\right)\sigma'\frac{\partial\mathbf{A}'}{\partial t'} + \sigma'\nabla'\Phi' - \nabla'\cdot\nabla'\mathbf{A}' = 0$$

The term on the bracket is non-dimensional and is called magnetic Reynolds number.

$$R_m = \frac{\mu_0\,\sigma_o L_o^2}{t_o}$$

The non-dimensional vector potential equation is given by:

$$R_m \sigma' \frac{\partial \mathbf{A}'}{\partial t'} + \sigma' \nabla' \Phi' - \nabla' \cdot \nabla' \mathbf{A}' = 0$$

The scale factors for parameters associated with current density and magnetic field remain similar to those for steady fields and are included here for completeness.

It's important to note that the total current density $\mathbf{J}$ is different from the current due to potential $\mathbf{J}_\Phi$ when the magnetic field is unsteady. This is because the changing magnetic field induces a magnetic field that generates eddy currents, which oppose the input current and alter the total current density. For current density due to potential $\mathbf{J}_\phi$,

$$J_{\Phi o} \mathbf{J}'_\Phi = -\left(\sigma_o \frac{1}{L_o} \Phi_o\right) \sigma' \nabla' \Phi'$$

Scale factor for current density is then,

$$J_{\Phi o} = \frac{\sigma_o \Phi_o}{L_o}$$

The non-dimensional current density is given by

$$\mathbf{J}'_\Phi = -\sigma' \nabla' \Phi'$$

For magnetic field,

$$B_o \mathbf{B}' = \left(\frac{1}{L_o} A_o\right) \nabla' \times \mathbf{A}'$$

Scale factor for magnetic field is then,

$$B_o = \frac{A_o}{L_o}$$

The non-dimensional magnetic field is given by

$$\mathbf{B}' = \nabla' \times \mathbf{A}'$$

The total current density $\mathbf{J}$ can be calculated from Ampere's law : $\mathbf{J} = \dfrac{1}{\mu_o}\nabla \times \mathbf{B}$

In-terms of non-dimensional variables,

$$J_o\mathbf{J}' = \frac{1}{\mu_o}\frac{1}{L_o}B_o\nabla' \times \mathbf{B}'$$

The scale factor for J_o is then given by

$$J_o = \frac{B_o}{\mu_o L_o} = \frac{\sigma_o\,\Phi_o}{L_o}$$

The non-dimensional current density is given by : $\mathbf{J}' = \nabla' \times \mathbf{B}'$

Summary of equations :

$$\nabla\,' \cdot \sigma\,'\nabla\,'\Phi\,' = 0$$

$$R_m\sigma\,'\frac{\partial \mathbf{A}\,'}{\partial t\,'} + \sigma\,'\nabla\,'\Phi\,' - \nabla\,' \cdot \nabla\,'\mathbf{A}\,' = 0$$

$$\mathbf{J}'_\Phi = -\sigma'\nabla'\Phi'$$

$$\mathbf{B}' = \nabla' \times \mathbf{A}'$$

$$\mathbf{J}' = \nabla' \times \mathbf{B}'$$

Summary of scale factors :

$$A_o = \mu_0 \sigma_o L_o \Phi_o$$

$$J_{\Phi o} = J_o = \frac{\sigma_o \, \Phi_o}{L_o}$$

$$B_o = \frac{A_o}{L_o}$$

$$R_m = \frac{\mu_0 \, \sigma_o L_o^2}{t_o}$$

3.9 Numerical Simulations with Potential Formulation of Maxwell Equations

3.9.1 Simulation of Steady Current Flow in a Wire Along the Axial Direction

This section presents a simulation study of a long hollow straight wire carrying a steady current due to a constant potential difference between its two ends. The wire has a length of l and inner and outer radii of r_i and r_o, respectively. Numerical simulations are utilized to compute various parameters of the wire, including the potential distribution along its length (Φ), the surface current density inside the wire ($\mathbf{J}$), the magnetic vector potential ($\mathbf{A}$) and the magnetic field inside the wire ($\mathbf{B}$). To model the wire, a long hollow cylinder with a uniform cross-sectional area is used, as depicted in Figure 3.1.

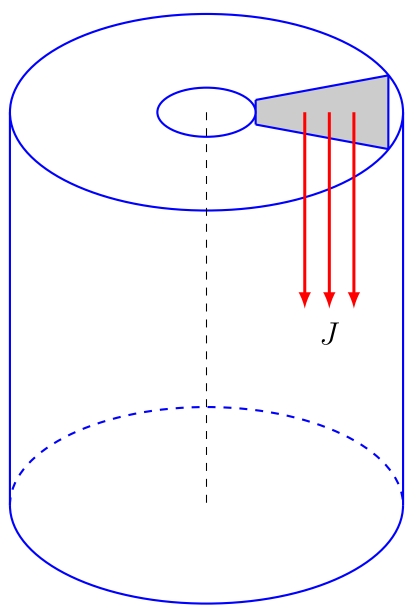

Figure 3.1: Hollow cylindrical geometry representing a wire carrying a steady axial current. The current density is uniform across the cross section of the wire. The computational domain is the shaded wedge geometry.

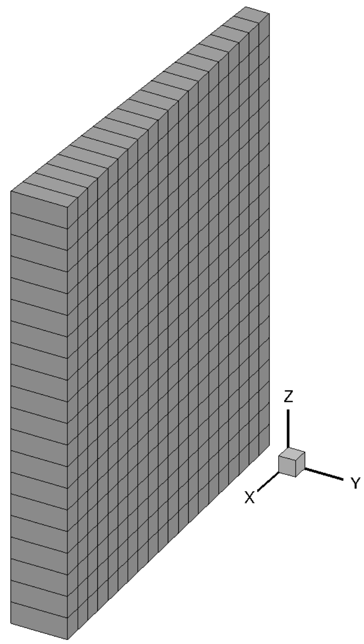

Figure 3.2: Computational domain used for the simulation of wire carrying a steady axial current using the wedge formulation. Presented figure is a representative mesh, not the actual.

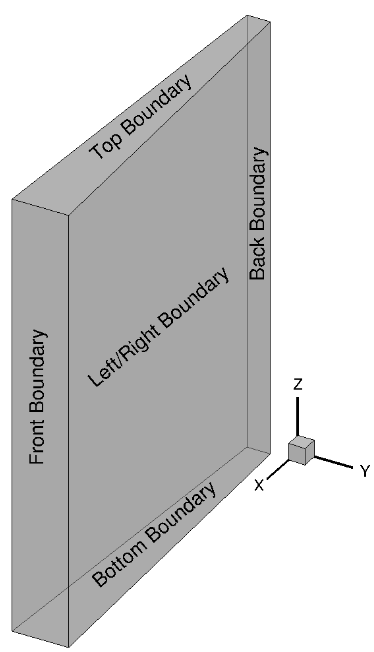

Figure 3.3: Boundary labels for the computational domain used in the wedge formulation. The left boundary corresponds to the front plane, and the right boundary is located on the other side of the geometry as shown. Presented figure is representative and not to scale.

Numerical simulations are conducted in geometry using the wedge formulation. The boundaries in these simulations are labeled according to the picture described in Figure 3.3.

The back boundary aligns with the cylinder's inner surface, while the front boundary is associated with the outer surface. The top and bottom boundaries correspond to the cylinder's upper and lower surfaces, respectively. Lastly, the left and right boundaries pertain to the axially symmetrical surfaces of the cylinder.

Table 3.1: Geometry, physical property and boundary condition parameters used for the numerical simulation of wire carrying a steady current in the axial direction.

Parameter	Description	Value	Units
r_i	Inner radius of wire	0.5	mm
r_o	Outer radius of wire	2.5	mm
l	Length of wire	5	mm
σ	Electrical conductivity	5.8×10^7	S/m
μ_0	Magnetic permeability	$4\pi \times 10^{-7}$	H/m
Φ_b	Potential at bottom boundary	0.0	V
Φ_t	Potential at top boundary	0.5	V
$\mathbf{A}_f$	Vector potential at front boundary	0.0	$\mathrm{T} \cdot \mathrm{m}$

The governing equation used for steady fields are

$$\nabla \cdot \sigma \nabla \Phi = 0$$

$$\nabla \cdot \nabla \mathbf{A} - \mu_0 \sigma \nabla \Phi = 0$$

The governing equation in non-dimensional form is given by

$$\nabla' \cdot \sigma' \nabla' \Phi' = 0$$

$$\nabla' \cdot \nabla' \mathbf{A}' - \sigma' \nabla' \Phi' = 0$$

Table 3.2: Boundary conditions used for the numerical simulation of wire carrying a steady current in the axial direction.

	Boundary Condition	
Boundary	Potential (Φ)	Vector potential ($\mathbf{A}$)
Top boundary	Fixed value	Zero normal gradient
Bottom boundary	Fixed value	Zero normal gradient
Left boundary	Zero normal gradient	Zero normal gradient
Right boundary	Zero normal gradient	Zero normal gradient
Front boundary	Zero normal gradient	Fixed value
Back boundary	Zero normal gradient	Zero normal gradient

Analytical solution:

A hollow cylinder is considered, having an inner radius of r_i and an outer radius of r_o. The top surface of the cylinder is situated at $z = +a$, while the bottom surface is located at $z = -a$. The top surface is maintained at a constant potential of V_o, while the bottom surface is kept at zero potential.

The governing equation for electric potential is given by

$$\nabla \cdot \sigma \nabla \Phi = 0$$

When σ is constant, the equation becomes:

$$\nabla \cdot \nabla \Phi = 0$$

The Laplace equation for the electric potential, expressed in cylindrical coordinates, is:

$$\frac{1}{r}\frac{\partial}{\partial r}\left(r\frac{\partial \Phi}{\partial r}\right) + \frac{1}{r^2}\frac{\partial^2 \Phi}{\partial \theta^2} + \frac{\partial^2 \Phi}{\partial z^2} = 0$$

Since the current flows purely in the z direction, the Laplace equation simplifies to:

$$\frac{\partial^2 \Phi}{\partial z^2} = 0$$

By integrating twice with respect to z, the following expression is obtained:

$$\Phi = C_1 z + C_2$$

Upon applying the boundary conditions, the solution is derived as:

$$\Phi = \frac{V_o}{2a}(z + a)$$

This result shows that the potential is a simple linear function of z, and the potential difference is uniformly distributed along the length of the cylinder. To determine the current density, Ohm's law can be applied:

$$\mathbf{J} = -\sigma \nabla \Phi$$

In cylindrical coordinates, the gradient of the potential is represented as:

$$\nabla\phi = \hat{r}\frac{\partial\phi}{\partial r} + \hat{\theta}\frac{1}{r}\frac{\partial\phi}{\partial\theta} + \hat{z}\frac{\partial\phi}{\partial z}$$

Given that $\Phi(z)$ is solely a function of z, only the axial component is non-vanishing:

$$\mathbf{J} = -\sigma\frac{\partial\Phi}{\partial z}\hat{z}$$

By substituting the expression for $\Phi(z)$, the following result is obtained:

$$J_z = -\frac{\sigma V_o}{2a}$$

Expressed in terms of the length of the wire (l):

$$J_z = -\frac{\sigma V_o}{l}$$

To determine the vector potential, the following equation needs to be solved:

$$\nabla\cdot\nabla\mathbf{A} = -\mu_0\mathbf{J}$$

As the current is purely axial, only the axial component of the vector potential must be considered:

$$\nabla\cdot\nabla A_z = -\mu_0 J_z$$

In cylindrical coordinates, the Laplacian can be expressed as:

$$\frac{1}{r}\frac{\partial}{\partial r}\left(r\frac{\partial A_z}{\partial r}\right) + \frac{1}{r^2}\frac{\partial^2 A_z}{\partial\theta^2} + \frac{\partial^2 A_z}{\partial z^2} = -\mu_0 J_z$$

Taking into account the symmetry, the vector potential varies only along the radius. Thus, the equation simplifies to:

$$\frac{1}{r}\frac{\partial}{\partial r}\left(r\frac{\partial A_z}{\partial r}\right) = -\mu_0 J_z$$

Rearranging the equation results in:

$$\frac{\partial}{\partial r}\left(r\frac{\partial A_z}{\partial r}\right) = -\mu_0 r J_z$$

By integrating the equation once, the following expression is obtained:

$$\frac{\partial A_z}{\partial r} = -\left(\frac{\mu_0 J_z}{2}\right) r + \frac{C_1}{r}$$

Integrating the equation again yields:

$$A_z = -\left(\frac{\mu_0 J_z}{4}\right) r^2 + C_1 \ln r + C_2$$

The constants C_1 and C_2 must be determined based on boundary conditions. To ensure that the magnetic field is continuous at the inner surface of the wire, the vector potential $\mathbf{A}$ must also be continuous across this boundary since $\mathbf{B} = \nabla \times \mathbf{A}$. This implies that the gradient of the vector potential should be zero at this surface, leading to the boundary condition:

$$\left.\frac{\partial \mathbf{A}}{\partial r}\right|_{r=r_i} = \mathbf{0}$$

Furthermore, to confine the magnetic field within the wire and ensure that it decays to zero as we move away from the wire, the vector potential should decay to zero as well. Mathematically, this means that the vector potential should be zero at the outer surface of the wire, leading to the boundary condition:

$$\mathbf{A}\Big|_{r=r_o} = \mathbf{0}$$

Applying the zero gradient boundary condition at the inner surface results in:

$$C_1 = \frac{\mu_0 J_z r_i^2}{2}$$

$$A_z = -\left(\frac{\mu_0 J_z}{4}\right) r^2 + \left(\frac{\mu_0 J_z r_i^2}{2}\right) \ln r + C_2$$

Applying the Dirichlet boundary condition at the outer surface yields:

$$C_2 = \frac{\mu_0 J_z r_o^2}{4} - \frac{\mu_0 J_z r_i^2 \ln r_o}{2}$$

Thus, the expression for the vector potential is given by:

$$A_z = -\left(\frac{\mu_0 J_z}{4}\right) r^2 + \left(\frac{\mu_0 J_z r_i^2}{2}\right) \ln r + \left(\frac{\mu_0 J_z}{4}\right) r_o^2 - \left(\frac{\mu_0 J_z r_i^2}{2}\right) \ln r_o$$

Simplifying the equation leads to:

$$A_z = -\left(\frac{\mu_0 J_z}{4}\right) (r^2 - r_o^2) + \left(\frac{\mu_0 J_z r_i^2}{2}\right) (\ln r - \ln r_o)$$

In terms of potential, one can write

$$A_z = \left(\frac{\mu_0 \sigma V_o}{4l}\right) (r^2 - r_o^2) - \left(\frac{\mu_0 \sigma V_o r_i^2}{2l}\right) (\ln r - \ln r_o)$$

The magnetic field can be calculated using the curl of the vector potential:

$$\mathbf{B} = \nabla \times \mathbf{A} = \left(\frac{1}{r}\frac{\partial A_z}{\partial \theta} - \frac{\partial A_\theta}{\partial z}\right) \hat{r} + \left(\frac{\partial A_r}{\partial z} - \frac{\partial A_z}{\partial r}\right) \hat{\theta} + \frac{1}{r}\left(\frac{\partial}{\partial r}(r A_\theta) - \frac{\partial A_r}{\partial \theta}\right) \hat{z}$$

The only non-vanishing component is (A_z depends solely on r):

$$B_\theta = -\frac{\partial A_z}{\partial r}\hat{\theta}$$

By differentiating the previously derived expression for A_z:

$$B_\theta = \left(\frac{\mu_0 J_z}{2}\right) r - \left(\frac{\mu_0 J_z r_i^2}{2}\right)\frac{1}{r} = \frac{\mu_0 J_z}{2r}(r^2 - r_i^2)$$

Using the expression for current density in terms of potential:

$$B_\theta = -\frac{\mu_0 \sigma V_o}{4ar}(r^2 - r_i^2)$$

Ampere's law can be employed to confirm that the derived magnetic field indeed represents the current supplied:

$$\mathbf{J} = \frac{1}{\mu_0}\nabla \times \mathbf{B}$$

Applying the curl definition in cylindrical coordinates:

$$\nabla \times \mathbf{B} = \left(\frac{1}{r}\frac{\partial B_z}{\partial \theta} - \frac{\partial B_\theta}{\partial z}\right)\hat{r} + \left(\frac{\partial B_r}{\partial z} - \frac{\partial B_z}{\partial r}\right)\hat{\theta} + \frac{1}{r}\left(\frac{\partial}{\partial r}(rB_\theta) - \frac{\partial B_r}{\partial \theta}\right)\hat{z}$$

The only non-vanishing component is:

$$J_z = \frac{1}{\mu_0}\left(\frac{1}{r}\frac{\partial}{\partial r}(rB_\theta)\right)$$

Using the previously derived expression for B_θ: $J(z) = -\dfrac{\sigma V_o}{2a}$

This confirms that the original expression for current density has been recovered.

To express the magnetic field in Cartesian coordinates, the magnetic field in cylindrical coordinates is first represented as $\mathbf{B} = B_r\hat{\mathbf{r}} + B_\theta\hat{\boldsymbol{\theta}} + B_z\hat{\mathbf{z}}$. Next, the relationship between the cylindrical and Cartesian basis vectors must be determined, which are given by:

$$\hat{\mathbf{r}} = cos(\theta)\hat{\mathbf{i}} + sin(\theta)\hat{\mathbf{j}} \qquad \hat{\boldsymbol{\theta}} \ = \text{-}sin(\theta)\hat{\mathbf{i}} + cos(\theta)\hat{\mathbf{j}} \qquad \hat{\mathbf{z}} = \hat{\mathbf{k}}$$

Substituting these expressions results in $\mathbf{B} = B_\theta(-\sin(\theta)\hat{\mathbf{i}} + \cos(\theta)\hat{\mathbf{j}})$. Expanding this equation gives $B_x = -B_\theta \sin(\theta)$, $B_y = B_\theta \cos(\theta)$, and $B_z = 0$, which are the Cartesian components of the magnetic field in terms of the cylindrical components. Along the x axis , $\theta = 0$, resulting in $B_x = 0$, $B_y = B_\theta$, and $B_z = 0$. Similarly, to express the coordinates in Cartesian coordinates, the following relations are used:

$$x = r\cos\theta \qquad y \ = r\sin\theta \qquad z = z$$

Along the x axis, $\theta = 0$, meaning $x = r$.

Solution:

The scale factors for non-dimensionalization are presented in Table 3.3. The length scale L_o is represented by the difference between the outer radius r_o and the inner radius r_i of the wire, $L_o = r_o - r_i$. The electric potential scale Φ_o represents the potential difference $\Delta\Phi$ between the two ends of the wire. The electric conductivity scale σ_o is the conductivity of the material used for the wire. The vector potential scale A_o is given by $\mu_0\sigma_o L_o\Phi_o$. The current density scale J_o is $\sigma_o\Phi_o/L_o$. The magnetic field scale B_o is represented by the vector potential scale divided by the length scale L_o. The actual values can be obtained by multiplying the scale factors. For example, $\mathbf{A} = \mathbf{A}'A_0$.

Table 3.3: Scale factors used for the non-dimensionalization of equations governing the simulation of steady current carrying wire in the axial direction.

Description	Scale	Value	Units
Length scale, L_o	$r_o - r_i$	2.0	mm
Electric potential scale, Φ_o	$\Phi_t - \Phi_b$	0.5	V
Electric conductivity scale, σ_o	σ	5.8×10^7	S/m
Vector potential scale, A_o	$\mu_0 \sigma_o L_o \Phi_o$	$0.0232\ \pi$	$\mathrm{T} \cdot \mathrm{m}$
Current density scale, J_o	$\dfrac{\sigma_o \Phi_o}{L_o}$	1.45×10^{10}	$\mathrm{A/m^2}$
Magnetic field scale, B_o	$\dfrac{A_o}{L_o}$	$11.6\ \pi$	T

Table 3.4: Non-dimensional values used for simulation of steady current carrying wire in the axial direction

Parameter	Dimensional Value	Non-dimensional Value
r_i	0.5 mm	0.25
r_o	2.5 mm	1.25
l	5 mm	2.5
σ	5.8×10^7 S/m	1.0
Φ_b	0.0 V	0.0
Φ_t	0.5 V	1.0
$\mathbf{A}_f$	0.0 Tm	0.0

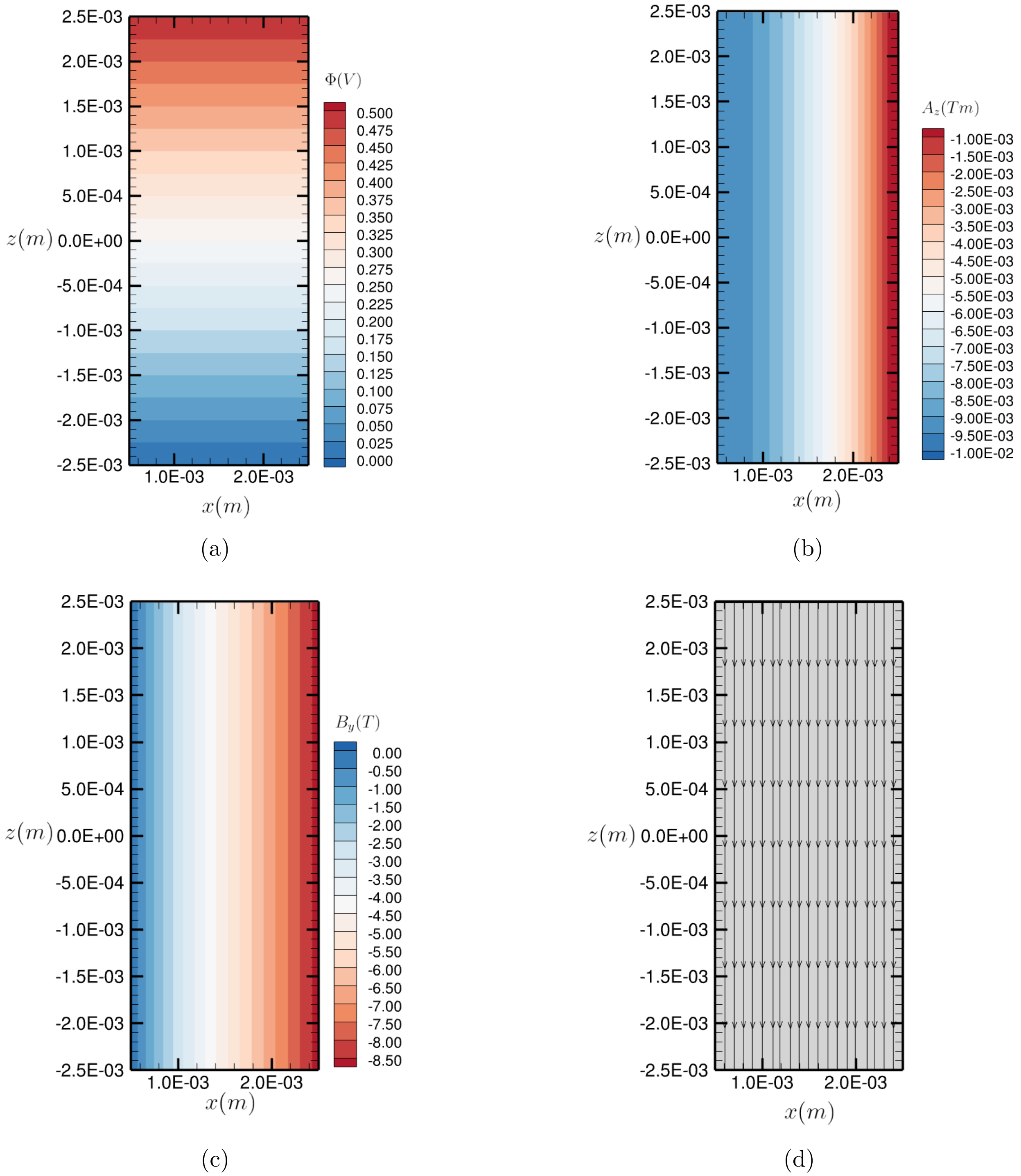

Figure 3.4: Simulation results of steady current flow in a wire along the axial direction. The figures display (a) the electric potential, (b) the magnetic vector potential, (c) the magnetic field and (d) streamlines of current density.

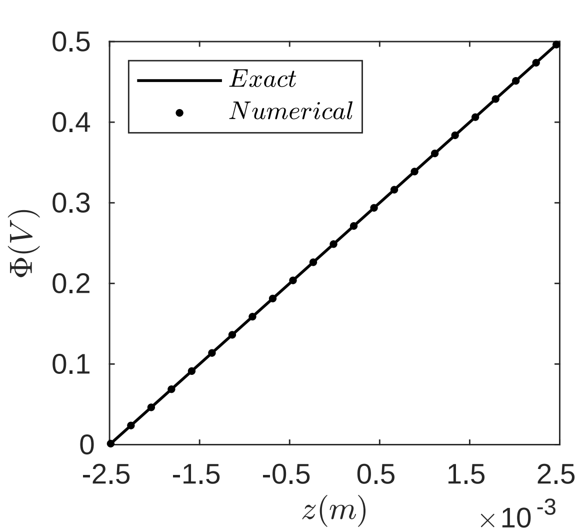

(a)

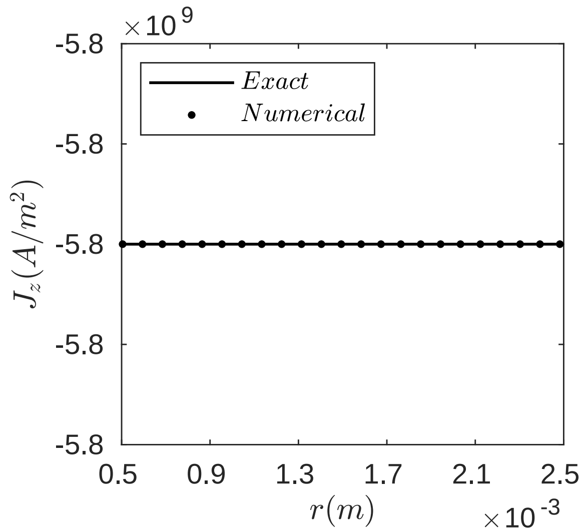

(b)

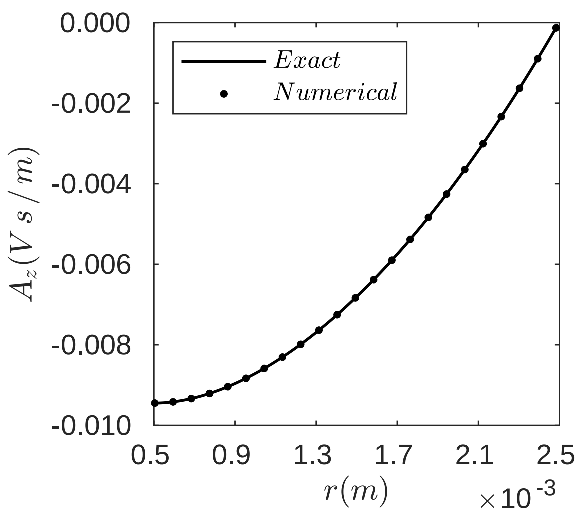

(c)

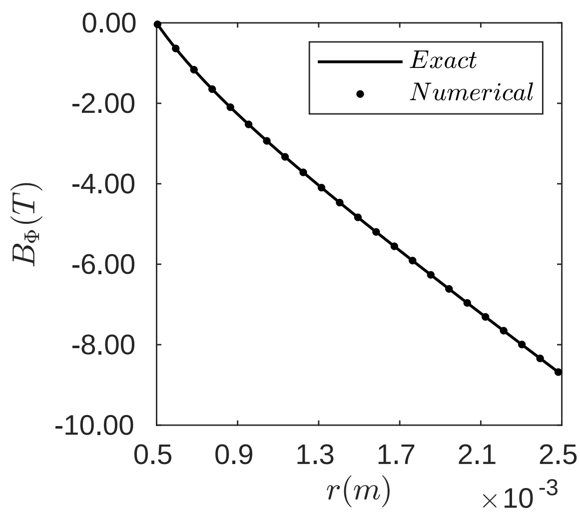

(d)

Figure 3.5: Comparison between the numerical and analytical solutions for a wire carrying steady axial current (a) the electric potential, (b) the current density, (c) the magnetic vector potential and (d) the magnetic field. It is noted that the current density is constant, included here for completeness. In cases of radial current flow, the current density varies, as demonstrated in subsequent simulations.

True Percent Relative Error

True percent relative error (ϵ_t) can be defined as:

$$\epsilon_t = \frac{\text{Exact Value - Numerical Value}}{\text{Exact Value}} * 100$$

Relative L^2 error

Relative L^2 error is a measure of the difference between two vector (arrays of numerical values) which can be used to evaluate the accuracy of numerical simulations. It is based on the L^2 norm, which is a way of calculating the size or length of a vector. The L^2 norm of vector is given by:

$$\|\Phi\|_2 = \sqrt{\sum_i (\Phi_i)^2}$$

The relative L^2 error between exact and numerical solution is defined as:

$$\text{Relative } L^2 \text{ error} = \frac{\|\Phi_{exact} - \Phi\|_2}{\|\Phi_{exact}\|_2}$$

Here, $\|\Phi_{exact} - \Phi\|_2$ represents the L^2 norm of the difference between the two vectors, and $\|\Phi_{exact}\|_2$ is the L^2 norm of the reference vector Φ_{exact}. The relative L^2 error provides a normalized measure of the difference between the two vectors, making it easier to compare the accuracy of different approximations or solutions. A smaller relative L^2 error indicates a more accurate approximation.

Discretization Error in Numerical Solutions:

Discretization error is one of the significant source of error in numerical solutions. It arises from approximating continuous equations and the flow domain with discrete counterparts. The finer the grid, the lower the error, but at an increased computational cost. To determine the ideal mesh size that balances accuracy and computational efficiency, a grid independence study is conducted.

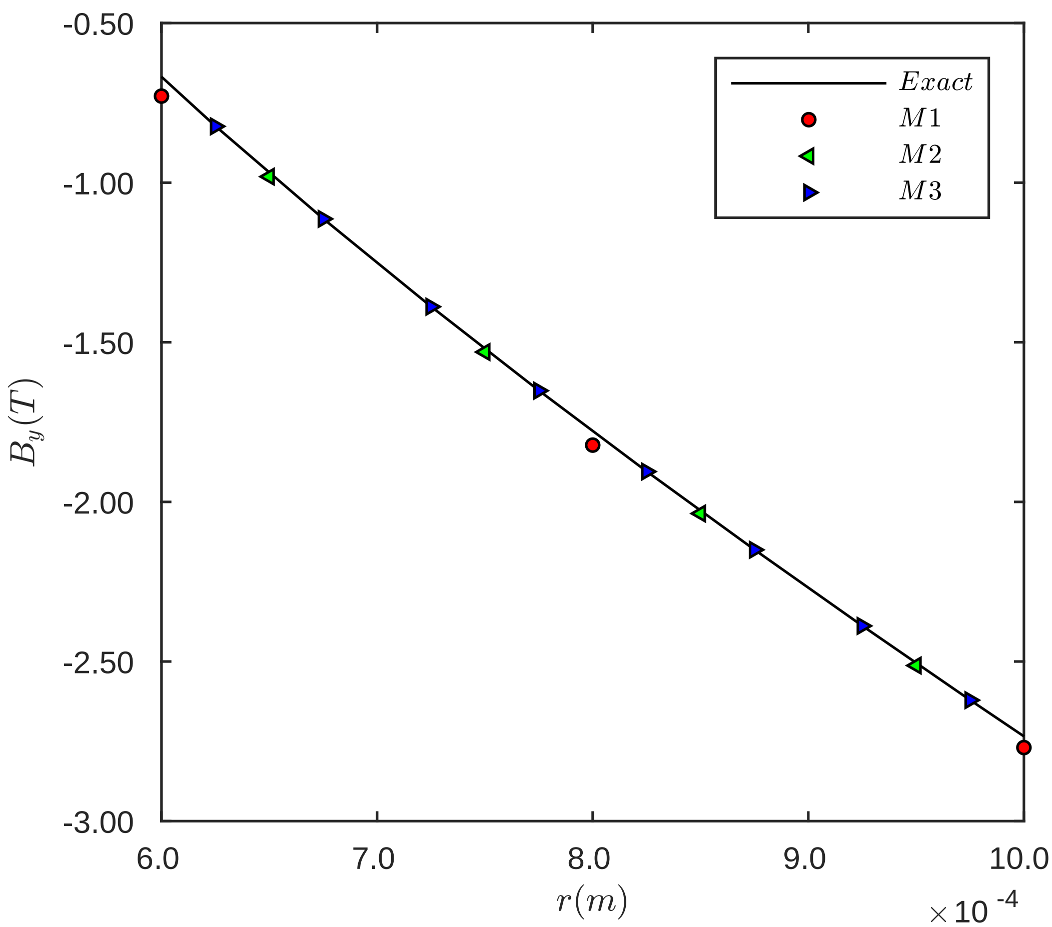

Figure 3.6: Mesh dependency on the magnetic field profile in the simulation of a wire with steady axial current. The plot is zoomed in on a segment of the radial length to more clearly illustrate errors, rather than depicting the entire radial extent.

To verify the grid-independence of the current solutions, the magnetic field is compared with analytical solution using three different mesh sizes: (i) a coarse mesh, designated as M1, with a grid resolution of $N_x \times N_z = 10 \times 15$, (ii) an intermediate mesh, known as M2, with a grid resolution of $N_x \times N_z = 20 \times 30$, and (iii) a fine mesh, termed M3, with a grid resolution of $N_x \times N_z = 40 \times 60$. As the mesh is refined, the results show improved agreement with the analytical solution.

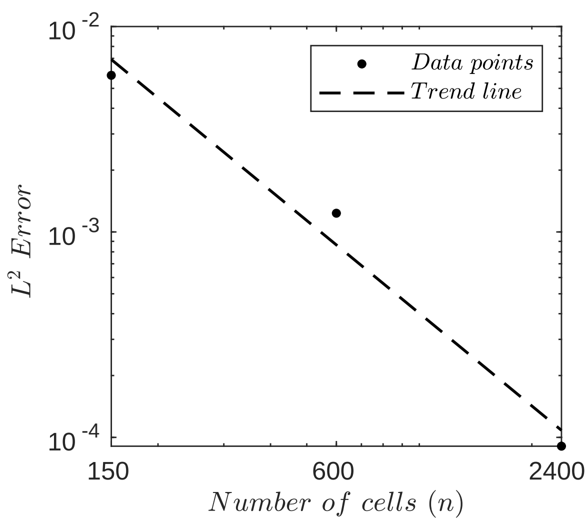

Figure 3.7: Comparison of L^2 error of magnetic field across varying mesh sizes in the simulation of a wire with steady axial current. The variable n denotes the number of cells in each mesh size. The error exhibits a linear decrease and tends toward zero as n increases.

Order of accuracy : In Figure 3.7 logarithm of the grid size against the logarithm of the corresponding error is plotted. A linear relationship in this log-log plot indicates that the error decreases at a certain rate as the grid is refined. The slope of the line in the log-log plot gives the order of accuracy. If p is the slope, the order of accuracy is said to be p. Mathematically, if the error E and the grid size h are related by $E \propto h^p$, then p is the order of accuracy. The calculated order of accuracy for the solver, based on the fitted line shown in Figure 3.7, is 1.499366.

3.9.2 Simulation of Steady Current Flow in a Hollow Cylinder Along the Radial Direction

This section presents a simulation study of a hollow cylinder under the influence of a constant potential difference applied between its inner and outer cylindrical surfaces, as shown in Figure 3.8. The cylinder has a length of l and inner and outer radii of r_i and r_o, respectively. Various parameters of the cylinder are computed using numerical simulations, including the potential distribution along its radius (Φ), the surface current density ($\mathbf{J}$) inside the cylinder, the magnetic vector potential ($\mathbf{A}$) and the magnetic field inside the cylinder ($\mathbf{B}$).

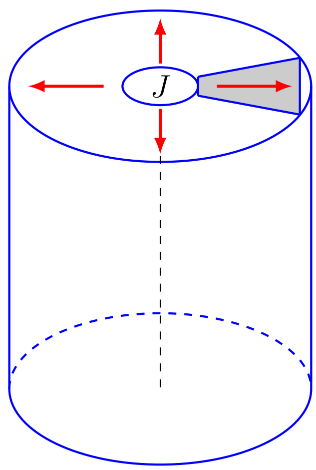

Figure 3.8: Hollow cylindrical geometry with a steady radial current, where the current density is a function of the cylinder radius.

Numerical simulations are conducted in geometry using the wedge formulation as before. The boundaries in these simulations are labeled in the same manner as the previous case according to the picture described in Figure 3.10. The back boundary aligns with the cylinder's inner surface, while the front boundary is associated with the outer surface. The top and bottom boundaries correspond to the cylinder's upper and lower surfaces, respectively. Lastly, the left and right boundaries pertain to the axially symmetrical surfaces of the cylinder.

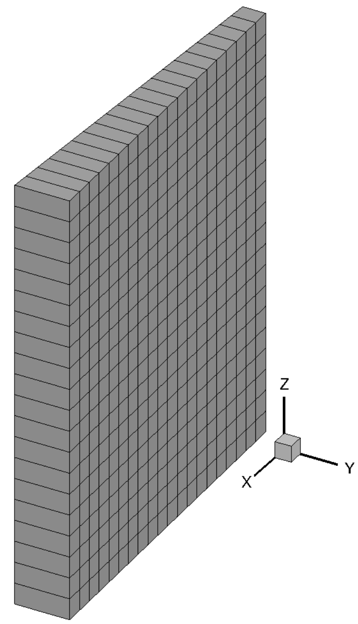

Figure 3.9: Computational mesh used for the simulation of hollow cylinder carrying a steady radial current using the wedge formulation. Presented figure is a representative mesh, not the actual.

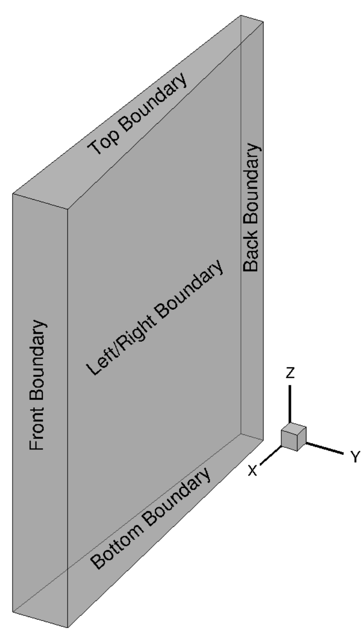

Figure 3.10: Boundary labels for the computational domain of hollow cylinder carrying a steady radial current using the wedge formulation. The left boundary corresponds to the front plane, and the right boundary is located on the other side of the geometry as shown. Presented figure is representative and not to scale.

For this test case, the dimensions of the setup are based on documents provided by General Fusion Inc, obtained through internal communication [43, 44].

Table 3.5: Geometry, physical property and boundary condition parameters used for the numerical simulation of hollow cylinder carrying a steady current in the radial direction.

Parameter	Description	Value	Units
r_i	Inner radius of cylinder	0.1	m
r_o	Outer radius of cylinder	0.15	m
H	Height of cylinder	0.01	m
μ_0	Magnetic permeability	$4\pi \times 10^{-7}$	H/m
σ	Electrical conductivity	5.8×10^{7}	S/m
Φ_b	Potential at back boundary	0.01	V
Φ_f	Potential at front boundary	0.0	V
$\mathbf{A}_t$, $\mathbf{A}_b$	Vector potential at top and bottom boundary	0.0	$\mathrm{T} \cdot \mathrm{m}$

The governing equation used for steady fields are

$$\nabla \cdot \sigma \nabla \Phi = 0$$

$$\nabla \cdot \nabla \mathbf{A} - \mu_0 \sigma \nabla \Phi = 0$$

The governing equation in non-dimensional form is given by

$$\nabla' \cdot \sigma' \nabla' \Phi' = 0$$

$$\nabla' \cdot \nabla' \mathbf{A}' - \sigma' \nabla' \Phi' = 0$$

Table 3.6: Boundary conditions used for the numerical simulation of hollow cylinder carrying a steady current in the radial direction.

	Boundary Condition	
Boundary	Potential (Φ)	Vector potential ($\mathbf{A}$)
Top boundary	Zero normal gradient	Fixed value
Bottom boundary	Zero normal gradient	Fixed value
Left boundary	Zero normal gradient	Zero normal gradient
Right boundary	Zero normal gradient	Zero normal gradient
Front boundary	Fixed value	Zero normal gradient
Back boundary	Fixed value	Zero normal gradient

Analytical solution:

For the case of a hollow cylinder with inner radius r_i and outer radius r_o, and with the outer surface at zero potential and the inner surface at potential V_o, the analytical solution is derived as follows:

Starting with the Laplace equation for the electric potential in cylindrical coordinates

$$\frac{1}{r}\frac{\partial}{\partial r}\left(r\frac{\partial \Phi}{\partial r}\right) + \frac{1}{r^2}\frac{\partial^2 \Phi}{\partial \theta^2} + \frac{\partial^2 \Phi}{\partial z^2} = 0$$

Since the current is purely along the r direction, the Laplace equation simplifies to:

$$\frac{\partial}{\partial r}\left(r\frac{\partial \Phi}{\partial r}\right) = 0$$

Integrating twice with respect to r

$$\Phi = C_1 \ln r + C_2$$

Applying the boundary conditions, the electric potential is obtained as follows:

$$\Phi = \frac{V_o}{\ln(r_i/r_o)} \ln(r/r_o)$$

To calculate the current density, Ohm's law can be used as before $\mathbf{J} = -\sigma\nabla\Phi$. In cylindrical coordinates, the gradient of the potential is given by:

$$\nabla\phi = \hat{r}\frac{\partial\phi}{\partial r} + \hat{\theta}\frac{1}{r}\frac{\partial\phi}{\partial\theta} + \hat{z}\frac{\partial\phi}{\partial z}$$

Since Φ is only a function of r:

$$J(r) = -\sigma\frac{\partial\Phi}{\partial r}\hat{r}$$

Substituting the previously derived expression for ϕ, the result is:

$$J(r) = -\frac{\sigma V_o}{r\ln(r_i/r_o)}$$

To find the vector potential, the following equation must be solved:

$$\nabla \cdot \nabla\mathbf{A} = -\mu_0\mathbf{J}_\Phi$$

where

$$\mathbf{J}_\Phi = -\sigma\nabla\Phi$$

Since the current is purely radial, only the radial component of the vector potential is considered.

$$\nabla \cdot \nabla A_r = -\mu_0 J(r)$$

In cylindrical coordinates, the Laplacian can be expressed as:

$$\frac{1}{r}\frac{\partial}{\partial r}\left(r\frac{\partial A_r}{\partial r}\right) + \frac{1}{r^2}\frac{\partial^2 A_r}{\partial \theta^2} + \frac{\partial^2 A_r}{\partial z^2} = -\mu_0 J(r)$$

The central part of the cylinder far from inner and outer radius is considered. In this region, radial dependence can be neglected. Therefore, the equation simplifies to:

$$\frac{\partial^2 A_r}{\partial z^2} = -\mu_0 J(r)$$

Integrating twice with respect to z, the following is obtained:

$$A_r = -\frac{1}{2}\mu_0 J(r) z^2 + C_1 z + C_2$$

Here, C_1 and C_2 are integration constants, which we can determine using the boundary conditions $A_r(r,\theta,a) = A_r(r,\theta,-a) = 0$. Consequently, the resulting expression is:

$$A_r(r,\theta,z) = \frac{1}{2}\mu_0 J(r)(a^2 - z^2)$$

The magnetic field can be calculated using the curl of the vector potential, which is given by:

$$\mathbf{B} = \nabla \times \mathbf{A} = \left(\frac{1}{r}\frac{\partial A_z}{\partial \theta} - \frac{\partial A_\theta}{\partial z}\right)\hat{r} + \left(\frac{\partial A_r}{\partial z} - \frac{\partial A_z}{\partial r}\right)\hat{\theta} + \frac{1}{r}\left(\frac{\partial}{\partial r}(rA_\theta) - \frac{\partial A_r}{\partial \theta}\right)\hat{z}$$

Only non-vanishing component is

$$\mathbf{B} = \nabla \times \mathbf{A} = \frac{\partial A_r}{\partial z}\hat{\theta}$$

$$B_\theta = -\mu_0 J(r) z$$

$$B_\theta = \frac{\mu_0 \sigma V_o z}{r \ln(r_i/r_o)}$$

It can be verified that this indeed represents the supplied current using Ampere's law:

$$\mathbf{J} = \frac{1}{\mu_0}\nabla \times \mathbf{B}$$

Applying the curl definition in cylindrical coordinates yields:

$$\nabla \times \mathbf{B} = \left(\frac{1}{r}\frac{\partial B_z}{\partial \theta} - \frac{\partial B_\theta}{\partial z}\right)\hat{r} + \left(\frac{\partial B_r}{\partial z} - \frac{\partial B_z}{\partial r}\right)\hat{\theta} + \frac{1}{r}\left(\frac{\partial}{\partial r}(rB_\theta) - \frac{\partial B_r}{\partial \theta}\right)\hat{z}$$

Only non-vanishing component is

$$\mathbf{J} = -\frac{1}{\mu_0}\frac{\partial B_\theta}{\partial z}\hat{r}$$

Using the expression we derived earlier for B_θ, the following expression is obtained:

$$J_r = -\frac{\sigma V_o}{r \ln(r_i/r_o)}$$

Thus, the original expression for current density is recovered.

Solution:

The scale factors for non-dimensionalization are presented in the Table 3.7. The actual values can be obtained by multiplying the scale factors. For example, $\mathbf{A} = \mathbf{A}' A_0$.

Table 3.7: Scale factors used for the numerical simulation of hollow cylinder carrying a steady current in the radial direction.

Description	Scale	Value	Units
Length scale, L_o	H	0.01	m
Electric potential scale, Φ_o	$\Phi_b - \Phi_f$	0.01	V
Electric conductivity scale, σ_o	σ	5.8×10^7	S/m
Vector potential scale, A_o	$\mu_0 \sigma_o L_o \Phi_o$	$0.232 \times 10^{-2}\ \pi$	$\mathrm{T} \cdot \mathrm{m}$
Current density scale, J_o	$\dfrac{\sigma_o \Phi_o}{L_o}$	5.8×10^7	$\mathrm{A/m^2}$
Magnetic field scale, B_o	$\dfrac{A_o}{L_o}$	$0.232\ \pi$	T

Table 3.8: Non-dimensional values used for the numerical simulation of hollow cylinder carrying a steady current in the radial direction.

Parameter	Dimensional Value	Non-dimensional Value
r_i	0.1 m	10
r_o	0.15 m	15
H	0.01 m	1.0
σ	5.8×10^7 S/m	1.0
Φ_f	0.0 V	0.0
Φ_b	0.01 V	1.0
$\mathbf{A}_t$, $\mathbf{A}_b$	0.0 Tm	0.0

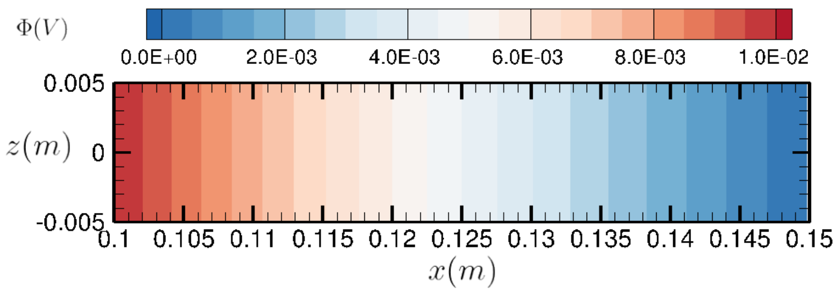

(a)

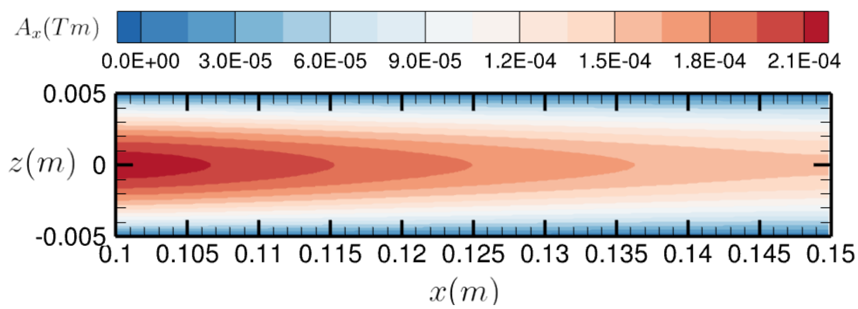

(b)

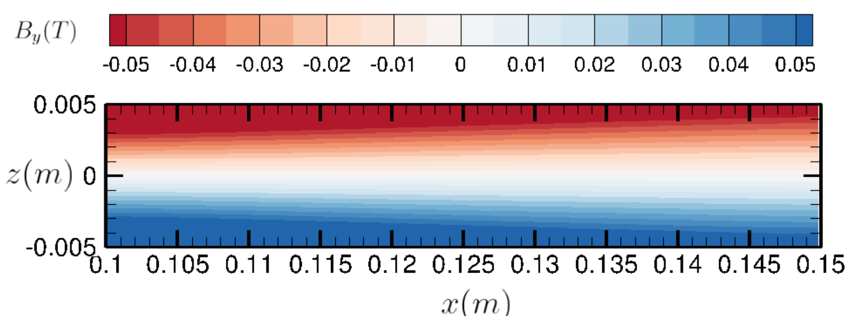

(c)

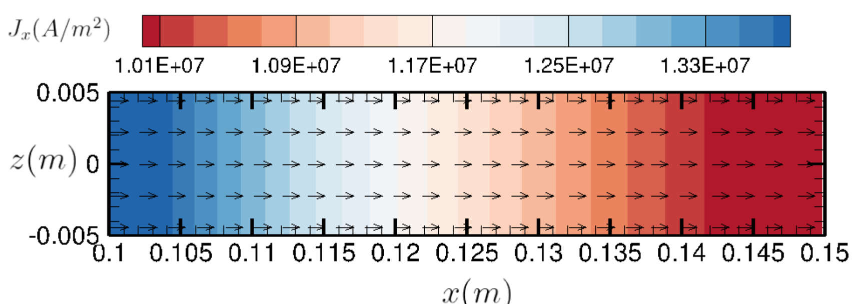

(d)

Figure 3.11: Simulation results of steady current flow in a hollow cylinder along the radial direction. The figures display (a) the electric potential, (b) the magnetic vector potential, (c) the magnetic field, and (d) the current density.

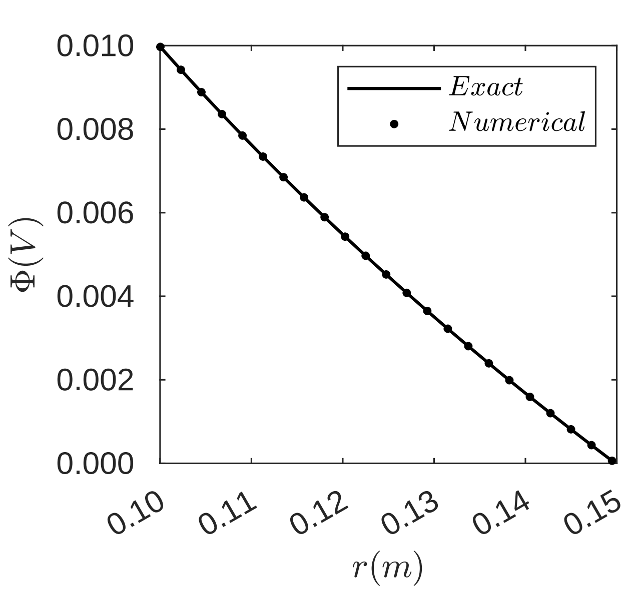

(a)

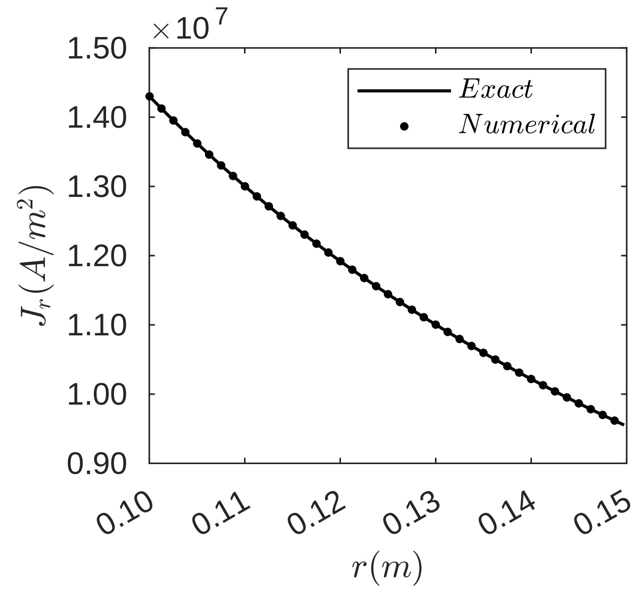

(b)

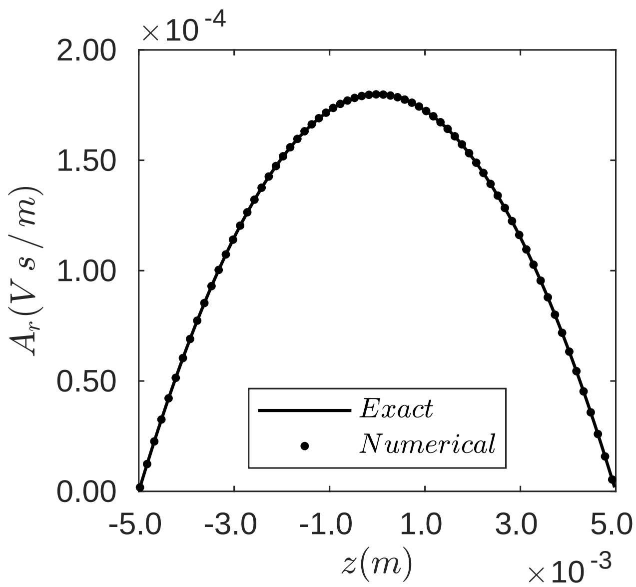

(c)

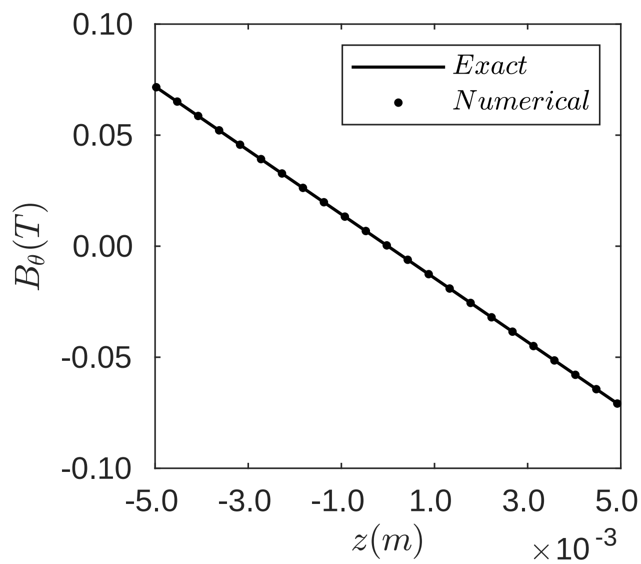

(d)

Figure 3.12: Comparison between the numerical and exact solutions for a hollow cylinder carrying steady radial current (a) the electric potential, (b) the current density, (c) the magnetic vector potential and (d) the magnetic field

Discretization Error in Numerical Solutions:

To verify the grid-independence of the current solutions, the magnetic vector potential is compared with analytical solution using three different mesh sizes: (i) a coarse mesh, designated as M1, with a grid resolution of $N_x \times N_z = 11 \times 5$, (ii) an intermediate mesh, known as M2, with a grid resolution of $N_x \times N_z = 21 \times 10$, and (iii) a fine mesh, termed M3, with a grid resolution of $N_x \times N_z = 41 \times 20$. As the mesh is refined, the results show improved agreement with the analytical solution.

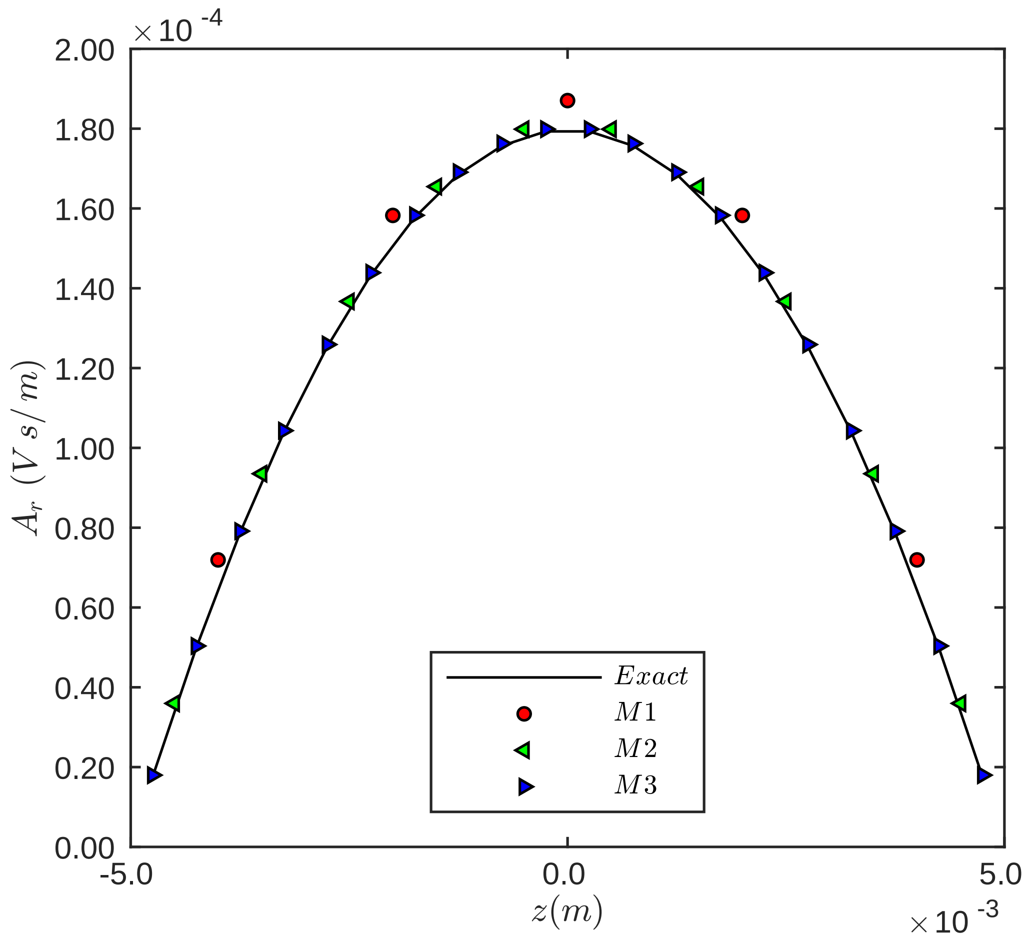

Figure 3.13: Mesh dependency on the magnetic vector potential profile in the simulation of a hollow cylinder with steady radial current.

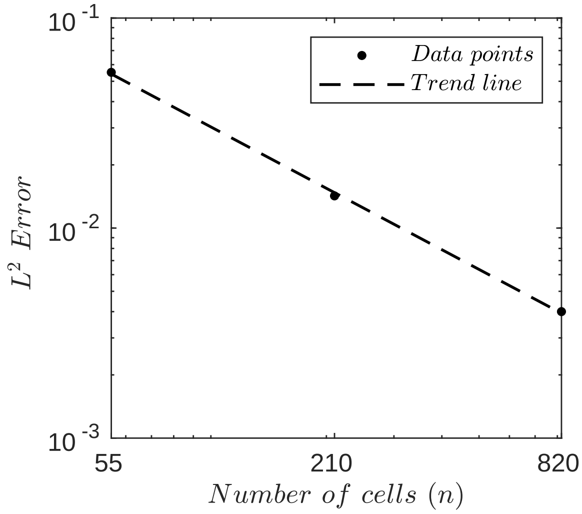

Figure 3.14: Comparison of L^2 error of magnetic vector potential across varying mesh sizes in the simulation of hollow cylinder carrying steady radial current. The variable n denotes the number of cells in each mesh size. The error exhibits a linear decrease and tends toward zero as n increases.

Order of accuracy : In Figure 3.14 logarithm of the grid size against the logarithm of the corresponding error is plotted. The calculated order of accuracy for the solver, based on the fitted line shown in Figure 3.14, is 0.970725. The analytical solution for the magnetic vector potential is derived by focusing on the central part of the cylinder, away from the inner and outer radii. This approach results in an approximate solution, as a precise analytical solution is not readily available. Consequently, the error in this solution is greater compared to cases involving axial current.

Chapter 4

Maxwell-Navier-Stokes Equations

The Maxwell equations describe the fundamental relationship between electric and magnetic fields, representing the essential laws of electromagnetism. On the other hand, fluid flow is governed by the Navier-Stokes equations, which take into account factors such as viscosity, pressure, and inertial effects. The intricate coupling between electromagnetic fields and fluid dynamics can be investigated by combining these equations (Magneto-hydrodynamics) [7, 32]. In this scenario, conductors are liquids that are not only capable of conducting electricity, but also have the ability to flow freely. To account for this characteristic, Ohm's law for moving conductors will be integrated into the Maxwell equations, and subsequently, the potential formulation of the Maxwell equations will be re-derived [30, 41, 49].

Within this framework, when a magnetic field is applied to a moving conductive liquid, it induces an electric current, leading to the generation of a Lorentz force. This force has the potential to alter the velocity and pressure fields within the fluid flow [18, 21, 38]. The induced currents also create secondary magnetic fields [47], which can modify the initially applied magnetic field. Alternatively, when both electric and magnetic fields are applied to a stationary conducting liquid, their interaction generates Lorentz force as well. This force can propel the fluid, providing a mechanism for controlling the fluid flow [3, 9, 15, 28, 48]. Thus, the combined set of Maxwell and Navier-Stokes equations not only reveals the distinct physics associated with fluid dynamics and electromagnetism but also uncovers a unique category of physics that emerges from the interaction of these two domains.

4.1 Potential Formulation of Maxwell Equations For Moving Conductors

4.1.1 Evolution Equation for Electric Scalar Potential

The expression for the electric field in terms of electric and magnetic potentials was derived in the preceding chapters.

This relationship is given by

$$\mathbf{E} = -\nabla\Phi - \frac{\partial \mathbf{A}}{\partial t}$$

Ohm's law for moving conductors is given by,

$$\mathbf{J} = \sigma(\mathbf{E} + \mathbf{U} \times \mathbf{B})$$

When expressed in terms of potentials, Ohm's law becomes

$$\mathbf{J} = -\sigma\nabla\Phi - \sigma\frac{\partial \mathbf{A}}{\partial t} + \sigma\mathbf{U} \times \mathbf{B}$$

Taking the divergence of the previous equation :

$$\nabla \cdot \mathbf{J} = -\nabla \cdot \sigma\nabla\Phi - \nabla \cdot \left(\sigma\frac{\partial \mathbf{A}}{\partial t}\right) + \nabla \cdot (\sigma\mathbf{U} \times \mathbf{B})$$

Using continuity equation, ($\nabla \cdot \mathbf{J} = 0$) [30, 41, 49]:

$$\nabla \cdot \sigma\nabla\Phi + \nabla \cdot \left(\sigma\frac{\partial \mathbf{A}}{\partial t}\right) - \nabla \cdot (\sigma\mathbf{U} \times \mathbf{B}) = 0$$

For steady fields, the governing equation simplifies to:

$$\nabla \cdot \sigma \nabla \Phi - \nabla \cdot (\sigma \mathbf{U} \times \mathbf{B}) = 0$$

Or if the conductivity is constant, it can be simplified to:

$$\nabla \cdot \nabla \Phi + \frac{\partial (\nabla \cdot \mathbf{A})}{\partial t} - \nabla \cdot (\mathbf{U} \times \mathbf{B}) = 0$$

The Coulomb gauge ($\nabla \cdot \mathbf{A} = 0$) is employed, leading to Poisson's equation:

$$\nabla \cdot \nabla \Phi - \nabla \cdot (\mathbf{U} \times \mathbf{B}) = 0$$

Summary of equations:

For unsteady fields,

$$\nabla \cdot \sigma \nabla \Phi + \nabla \cdot \left(\sigma \frac{\partial \mathbf{A}}{\partial t} \right) - \nabla \cdot (\sigma \mathbf{U} \times \mathbf{B}) = 0$$

For steady fields,

$$\nabla \cdot \sigma \nabla \Phi - \nabla \cdot (\sigma \mathbf{U} \times \mathbf{B}) = 0$$

Current due to potential,

$$\mathbf{J}_\phi = -\sigma \nabla \Phi$$

Induced current due to the motion of the conducting liquid,

$$\mathbf{J}_u = \sigma \mathbf{U} \times \mathbf{B}$$

4.1.2 Evolution Equation for Magnetic Vector Potential

The Poisson equation for the vector potential, derived in previous chapters, is given by:

$$\nabla \cdot \nabla \mathbf{A} = -\mu_0 \mathbf{J}$$

Employing Ohm's law for moving conductors, given by $\mathbf{J} = \sigma(\mathbf{E} + \mathbf{U} \times \mathbf{B})$, the equation becomes:

$$\nabla \cdot \nabla \mathbf{A} = -\mu_0 \sigma (\mathbf{E} + \mathbf{U} \times \mathbf{B})$$

Substituting the expression for the electric field in terms of electric potential for time-varying fields:

$$\nabla \cdot \nabla \mathbf{A} = -\mu_0 \sigma \left(-\nabla \Phi - \frac{\partial \mathbf{A}}{\partial t} + \mathbf{U} \times \mathbf{B} \right)$$

Simplifying and rearranging [30, 41, 49]:

$$\mu_0 \sigma \frac{\partial \mathbf{A}}{\partial t} + \mu_0 \sigma \nabla \Phi - \mu_0 \sigma \mathbf{U} \times \mathbf{B} - \nabla \cdot \nabla \mathbf{A} = 0$$

For steady fields without time dependence:

$$\nabla \cdot \nabla \mathbf{A} - \mu_0 \sigma \nabla \Phi + \mu_0 \sigma \mathbf{U} \times \mathbf{B} = 0$$

Summary of equations :

For unsteady fields : $\mu_0 \sigma \frac{\partial \mathbf{A}}{\partial t} - \nabla \cdot \nabla \mathbf{A} + \mu_0 \sigma \nabla \Phi - \mu_0 \sigma \mathbf{U} \times \mathbf{B} = 0$

For steady fields : $\nabla \cdot \nabla \mathbf{A} - \mu_0 \sigma \nabla \Phi + \mu_0 \sigma \mathbf{U} \times \mathbf{B} = 0$

4.1.3 Non-dimensional Form of Potential Formulation of Maxwell Equations for Moving Conductors for Steady Fields

The governing equations for electric potential and magnetic vector potential for steady fields are:

$$\nabla \cdot \sigma \nabla \Phi - \nabla \cdot (\sigma \mathbf{U} \times \mathbf{B}) = 0$$

$$\nabla \cdot \nabla \mathbf{A} - \mu_0 \sigma \nabla \Phi + \mu_0 \sigma \left(\mathbf{U} \times \mathbf{B} \right) = 0$$

The non-dimensional form of the equations is derived by introducing length scale L_o, electric conductivity scale σ_o, electric potential scale Φ_o, velocity scale U_o, vector potential scale A_o. Note that using the definition $\mathbf{B} = \nabla \times \mathbf{A}$, magnetic field scale can be written as $B_o = \dfrac{A_o}{L_o}$. The non-dimensional quantities ∇', σ', Φ', $\mathbf{A}'$, $\mathbf{B}'$,$\mathbf{U}'$ to correspond to ∇, σ, Φ, $\mathbf{A}$, $\mathbf{B}$, $\mathbf{U}$. The relationships among scale factors, dimensional and non-dimensional quantities is given as: $\nabla' = \dfrac{\nabla}{\nabla_o}$, $\sigma' = \dfrac{\sigma}{\sigma_o}$, $\Phi' = \dfrac{\Phi}{\Phi_o}$, $\mathbf{A}' = \dfrac{\mathbf{A}}{A_o}$, $\mathbf{B}' = \dfrac{\mathbf{B}}{B_o}$, $\mathbf{U}' = \dfrac{\mathbf{U}}{U_o}$. In terms of non-dimensional quantities and scale factors, the electric potential equation can be written as

$$\left(\frac{1}{L_o} \sigma_o \frac{1}{L_o} \Phi_o \right) \nabla' \cdot \sigma' \nabla' \Phi' - \left(\frac{1}{L_o} \sigma_o U_o \frac{A_o}{L_o} \right) \nabla' \cdot (\sigma' \mathbf{U}' \times \mathbf{B}') = 0$$

Dividing the equation by $\left(\dfrac{\sigma_o \Phi_o}{L_o^2} \right)$

$$\nabla' \cdot \sigma' \nabla' \Phi' - \left(\frac{L_o^2}{\sigma_o \Phi_o} \frac{\sigma_o U_o A_o}{L_o^2} \right) \nabla' \cdot (\sigma' \mathbf{U}' \times \mathbf{B}') = 0$$

Simplifying,

$$\nabla' \cdot \sigma' \nabla' \Phi' - \left(\frac{U_o A_o}{\Phi_o} \right) \nabla' \cdot (\sigma' \mathbf{U}' \times \mathbf{B}') = 0$$

Choosing the scale factor $A_o = \mu_0 \sigma_o L_o \Phi_o$.

$$\nabla' \cdot \sigma' \nabla' \Phi' - (\mu_0 \sigma_o L_o U_o) \nabla' \cdot (\sigma' \mathbf{U}' \times \mathbf{B}') = 0$$

Another definition of magnetic Reynolds number relating to velocity of the conductor is given by, $Re_m = \mu_0 \sigma_o U_o L_o$. Note that previous definition of magnetic Reynolds number $Re_m = \dfrac{\mu_0 \, \sigma_o L_o^2}{t_o}$, is used even if there is no physical movement of conductors. This earlier definition is related to length and time scales associated time varying electromagnetic fields such as sinusoidal currents (AC current). The non-dimensional electric potential equation is given by

$$\nabla' \cdot \sigma' \nabla' \Phi' - Re_m \nabla' \cdot (\sigma' \mathbf{U}' \times \mathbf{B}') = 0$$

In terms of non-dimensional quantities and scale factors, magnetic vector potential is given by

$$\left(\frac{1}{L_o} \frac{1}{L_o} A_o \right) \nabla' \cdot \nabla' \mathbf{A}' - \left(\mu_0 \sigma_o \frac{1}{L_o} \Phi_o \right) \sigma' \nabla' \Phi' + \left(\mu_0 \sigma_o U_o \frac{A_o}{L_o} \right) \sigma' (\mathbf{U}' \times \mathbf{B}') = 0$$

Multiply the whole equation, by $\dfrac{L_o^2}{A_o}$:

$$\nabla' \cdot \nabla' \mathbf{A}' - \left(\frac{\mu_0 \sigma_o L_o \Phi_o}{A_o} \right) \sigma' \nabla' \Phi' + (\mu_0 \sigma_o U_o L_o) \sigma' (\mathbf{U}' \times \mathbf{B}') = 0$$

Using scale factor for magnetic vector potential, $A_o = \mu_0 \sigma_o L_o \Phi_o$

$$\nabla' \cdot \nabla' \mathbf{A}' - \sigma' \nabla' \Phi' + (\mu_0 \sigma_o U_o L_o) \sigma' (\mathbf{U}' \times \mathbf{B}') = 0$$

Using the definition of magnetic Reynolds number relating to velocity of the conductor, $Re_m = \mu_0 \sigma_o U_o L_o$,

$$\nabla' \cdot \nabla' \mathbf{A}' - \sigma' \nabla' \Phi' + Re_m \, \sigma' \left(\mathbf{U}' \times \mathbf{B}' \right) = 0$$

For convenience, following non-dimensional current densities are defined. The current due to applied potential is

$$\mathbf{J}'_\phi = -\sigma' \nabla' \Phi'$$

The induced current due to the motion of the conducting liquid is

$$\mathbf{J}_u{}' = \sigma' \mathbf{U}' \times \mathbf{B}'$$

The total current due to induced magnetic field is

$$\mathbf{J} = -\frac{1}{\mu_0} \nabla \cdot \nabla \mathbf{A}$$

In terms of non-dimensional parameters,

$$J_o \mathbf{J}' = -\left(\frac{1}{\mu_0} \frac{1}{L_o} \frac{1}{L_o} A_o \right) \nabla' \cdot \nabla' \mathbf{A}'$$

Since $A_o = \mu_0 \sigma_o L_o \Phi_o$, the scale factor simplifies to again $J_o = \dfrac{\sigma_o \Phi_o}{L_o}$ and non-dimensional current is

$$\mathbf{J}' = -\nabla' \cdot \nabla' \mathbf{A}'$$

Summary of equations :

$$\nabla' \cdot \sigma' \nabla' \Phi' - Re_m \nabla' \cdot \left(\sigma' \mathbf{U}' \times \mathbf{B}' \right) = 0$$

$$\nabla' \cdot \nabla' \mathbf{A}' - \sigma' \nabla' \Phi' + Re_m \, \sigma' \left(\mathbf{U}' \times \mathbf{B}' \right) = 0$$

Summary of equations :

$$\mathbf{J}'_{\phi} = -\sigma'\nabla'\Phi'$$

$$\mathbf{J}_u{}' = \sigma{}'\mathbf{U}{}' \times \mathbf{B}{}'$$

$$\mathbf{J}{}' = -\nabla{}' \cdot \nabla{}'\mathbf{A}{}'$$

Summary of scale factors and non-dimensional numbers:

$$A_o = \mu_0 \sigma_o L_o \Phi_o$$

$$J_o = \frac{\sigma_o \, \Phi_o}{L_o}$$

$$B_o = \frac{A_o}{L_o}$$

$$Re_m = \mu_0 \sigma_o U_o L_o$$

4.1.4 Non-dimensional Form of Potential Formulation of Maxwell Equations for Moving Conductors for Unsteady Fields

The governing equations for electric potential and magnetic vector potential are:

$$\nabla \cdot \sigma \nabla \Phi + \nabla \cdot \left(\sigma \frac{\partial \mathbf{A}}{\partial t} \right) - \nabla \cdot (\sigma \mathbf{U} \times \mathbf{B}) = 0$$

$$\mu_0 \sigma \frac{\partial \mathbf{A}}{\partial t} - \nabla \cdot \nabla \mathbf{A} + \mu_0 \sigma \nabla \Phi - \mu_0 \sigma \left(\mathbf{U} \times \mathbf{B} \right) = 0$$

The non-dimensional form of the equations is derived by introducing length scale L_o, electric conductivity scale σ_o, electric potential scale Φ_o, vector potential scale A_o, time scale t_o. Note that velocity scale $U_o = \dfrac{L_o}{t_o}$ and magnetic Field scale $B_o = \dfrac{A_o}{L_o}$. The non-dimensional quantities ∇', σ', Φ', $\mathbf{A}'$, $\mathbf{B}'$,$\mathbf{U}'$, t', to correspond to ∇, σ, Φ, $\mathbf{A}$, $\mathbf{B}$, $\mathbf{U}$, t.

The relationships among scale factors, dimensional and non-dimensional quantities is given as: $\nabla' = \dfrac{\nabla}{\nabla_o}$, $\sigma' = \dfrac{\sigma}{\sigma_o}$, $\Phi' = \dfrac{\Phi}{\Phi_o}$, $\mathbf{A}' = \dfrac{\mathbf{A}}{A_o}$, $\mathbf{B}' = \dfrac{\mathbf{B}}{B_o}$, $\mathbf{U}' = \dfrac{\mathbf{U}}{U_o}$, $t' = \dfrac{t}{t_o}$.

In terms of non-dimensional quantities and scale factors, the electric potential equation can be written as

$$\left(\frac{1}{L_o^2} \sigma_o \, \Phi_o \right) \nabla' \cdot \sigma' \nabla' \Phi' + \left(\frac{1}{L_o} \sigma_o \, \frac{A_o}{t_o} \right) \nabla' \cdot \left(\sigma' \frac{\partial \mathbf{A}'}{\partial t'} \right) - \left(\frac{1}{L_o} \sigma_o \, \frac{L_o}{t_o} \frac{A_o}{L_o} \right) \nabla' \cdot (\sigma' \mathbf{U}' \times \mathbf{B}') = 0$$

Dividing the equation by $\left(\dfrac{\sigma_o \, \Phi_o}{L_o^2} \right)$

$$\nabla' \cdot \sigma' \nabla' \Phi' + \left(\frac{L_o^2}{\sigma_o \, \Phi_o} \frac{\sigma_o A_o}{L_o \, t_o} \right) \nabla' \cdot \left(\sigma' \frac{\partial \mathbf{A}'}{\partial t'} \right) - \left(\frac{L_o^2}{\sigma_o \, \Phi_o} \frac{\sigma_o A_o}{L_o t_o} \right) \nabla' \cdot (\sigma' \mathbf{U}' \times \mathbf{B}') = 0$$

Simplifying,

$$\nabla' \cdot \sigma'\nabla'\Phi' + \left(\frac{L_o A_o}{\Phi_o t_o}\right)\nabla' \cdot \left(\sigma'\frac{\partial \mathbf{A}'}{\partial t'}\right) - \left(\frac{L_o A_o}{\Phi_o t_o}\right)\nabla' \cdot (\sigma'\mathbf{U}' \times \mathbf{B}') = 0$$

Choosing the scale factor $A_o = \mu_0 \sigma_o L_o \Phi_o$.

$$\nabla' \cdot \sigma'\nabla'\Phi' + \left(\frac{\mu_0 \sigma_o L_o^2}{t_o}\right)\nabla' \cdot \left(\sigma'\frac{\partial \mathbf{A}'}{\partial t'}\right) - \left(\frac{\mu_0 \sigma_o L_o^2}{t_o}\right)\nabla' \cdot (\sigma'\mathbf{U}' \times \mathbf{B}') = 0$$

The non-dimensional electric potential equation is,

$$\nabla' \cdot \sigma'\nabla'\Phi' + Re_m\,\nabla' \cdot \left(\sigma'\frac{\partial \mathbf{A}'}{\partial t'}\right) - Re_m\,\nabla' \cdot (\sigma'\mathbf{U}' \times \mathbf{B}') = 0$$

In terms of non-dimensional quantities and scale factors, magnetic vector potential equation is given by

$$\left(\mu_0 \sigma_o \frac{A_o}{t_o}\right)\sigma'\frac{\partial \mathbf{A}'}{\partial t'} - \left(\frac{1}{L_o^2}A_o\right)\nabla' \cdot \nabla'\mathbf{A}' + \left(\mu_0 \sigma_o \frac{\Phi_o}{L_o}\right)\sigma'\nabla'\Phi' - \left(\mu_0 \sigma_o \frac{L_o}{t_o}\frac{A_o}{L_o}\right)\sigma'\mathbf{U}' \times \mathbf{B}' = 0$$

Multiply the whole equation, by $\dfrac{L_o^2}{A_o}$:

$$\left(\frac{\mu_0 \sigma_o L_o^2}{t_o}\right)\sigma'\frac{\partial \mathbf{A}'}{\partial t'} - \nabla' \cdot \nabla'\mathbf{A}' + \left(\frac{\mu_0 \sigma_o L_o \Phi_o}{A_o}\right)\sigma'\nabla'\Phi' - \left(\frac{\mu_0 \sigma_o L_o^2}{t_o}\right)\sigma'\mathbf{U}' \times \mathbf{B}' = 0$$

Using scale factor for magnetic vector potential, $A_o = \mu_0 \sigma_o L_o \Phi_o$.

$$\left(\frac{\mu_0 \sigma_o L_o^2}{t_o}\right)\sigma'\frac{\partial \mathbf{A}'}{\partial t'} - \nabla' \cdot \nabla'\mathbf{A}' + \sigma'\nabla'\Phi' - \left(\frac{\mu_0 \sigma_o L_o^2}{t_o}\right)\sigma'\mathbf{U}' \times \mathbf{B}' = 0$$

Using definition of magnetic Reynolds number, $Re_m = \dfrac{\mu_0\, \sigma_o L_o^2}{t_o}$, the non-dimensional vector potential equation is given by:

$$Re_m\, \sigma\,' \frac{\partial \mathbf{A}\,'}{\partial t\,'} - \nabla\,' \cdot \nabla\,' \mathbf{A}\,' + \sigma\,' \nabla\,' \Phi\,' - Re_m\, \sigma\,' \mathbf{U}\,' \times \mathbf{B}\,' = 0$$

Summary of equations :

$$\nabla\,' \cdot \sigma\,' \nabla\,' \Phi\,' + Re_m\, \nabla\,' \cdot \left(\sigma\,' \frac{\partial \mathbf{A}\,'}{\partial t\,'} \right) - Re_m\, \nabla\,' \cdot (\sigma\,' \mathbf{U}\,' \times \mathbf{B}\,') = 0$$

$$Re_m\, \sigma\,' \frac{\partial \mathbf{A}\,'}{\partial t\,'} - \nabla\,' \cdot \nabla\,' \mathbf{A}\,' + \sigma\,' \nabla\,' \Phi\,' - Re_m\, \sigma\,' (\mathbf{U}\,' \times \mathbf{B}) = 0$$

$$\mathbf{J}'_\phi = -\sigma' \nabla' \Phi'$$

$$\mathbf{J}_u\,' = \sigma\,' \mathbf{U}\,' \times \mathbf{B}\,'$$

$$\mathbf{J}\,' = -\nabla\,' \cdot \nabla\,' \mathbf{A}\,'$$

Summary of scale factors and non-dimensional numbers:

$$A_o = \mu_0 \sigma_o L_o \Phi_o$$

$$J_o = \frac{\sigma_o\, \Phi_o}{L_o}$$

$$B_o = \frac{A_o}{L_o}$$

$$Re_m = \frac{\mu_0\, \sigma_o L_o^2}{t_o}$$

4.2 Navier-Stokes Equations for Neutral Fluids

The Navier-Stokes equations [2, 51] governing incompressible flow are coupled system of nonlinear partial differential equations that describe the motion of a viscous fluid. The Navier-Stokes equations are expressed in terms of the conservation laws of mass and momentum for a fluid .

Mass-Conservation : The continuity equation in differential form is expressed as:

$$\nabla \cdot \mathbf{U} = 0$$

Momentum-Conservation : The momentum equation in differential form is expressed as:

$$\frac{\partial \rho \mathbf{U}}{\partial t} + \nabla \cdot (\rho \mathbf{U}\mathbf{U}) - \nabla \cdot (\mu \nabla \mathbf{U}) + \nabla p = 0$$

In these equations, the density and viscosity are considered to be constant.

4.2.1 Non-Dimensional Form of Navier-Stokes Equations for Neutral Fluids

The non-dimensional form of the equations [2, 51] is derived by introducing density scale ρ_o, time scale t_o, length scale L_o, velocity scale U_o and pressure scale p_o. The non-dimensional quantities ρ', t', ∇', $\mathbf{U}'$, p' to correspond to ρ, t, ∇, $\mathbf{U}$, p.

The relationships among scale factors, dimensional and non-dimensional quantities is given as: $\rho' = \dfrac{\rho}{\rho_o}$, $t' = \dfrac{t}{t_o}$, $\nabla' = \dfrac{\nabla}{\nabla_o}$, $\mathbf{U}' = \dfrac{\mathbf{U}}{U_o}$, $p' = \dfrac{p}{p_o}$. Note that $\nabla_o = 1/L_o$ and $U_o = L_o/t_o$.

Continuity equation : The non-dimensional continuity equation becomes:

$$\left(\frac{1}{L_o}\frac{L_o}{t_o}\right)\nabla'\cdot\mathbf{U}'=0$$

which simplifies to

$$\nabla'\cdot\mathbf{U}'=0$$

Momentum equation : Consider the momentum equation with constant viscosity,

$$\frac{\partial\rho\mathbf{U}}{\partial t}+\nabla\cdot(\rho\mathbf{U}\mathbf{U})-\mu\nabla\cdot(\nabla\mathbf{U})+\nabla p=0$$

The non-dimensional momentum equation becomes:

$$\left(\frac{\rho_o}{t_o}\frac{L_o}{t_o}\right)\frac{\partial\rho'\mathbf{U}'}{\partial t'}+\left(\frac{1}{L_o}\rho_o\frac{L_o^2}{t_o^2}\right)\nabla'\cdot(\rho'\mathbf{U}'\mathbf{U}')-\mu\left(\frac{1}{L_o^2}\frac{L_o}{t_o}\right)\nabla'\cdot(\nabla'\mathbf{U}')+\left(\frac{1}{L_o}p_o\right)\nabla'p'=0$$

Dividing by $(\rho_o L_o/t_o^2)$:

$$\frac{\partial\rho'\mathbf{U}'}{\partial t'}+\nabla'\cdot(\rho'\mathbf{U}'\mathbf{U}')-\left(\frac{\mu}{U_o\rho_o L_o}\right)\nabla'\cdot(\nabla'\mathbf{U}')+\left(\frac{p_o}{\rho_o U_o^2}\right)\nabla'p'=0$$

The equation becomes non-dimensional when selecting the pressure scale as $p_o = \rho_o U_o^2$ (Inertial scaling for pressure [52])

$$\frac{\partial\rho'\mathbf{U}'}{\partial t'}+\nabla'\cdot(\rho'\mathbf{U}'\mathbf{U}')-\left(\frac{\mu}{U_o\rho_o L_o}\right)\nabla'\cdot(\nabla'\mathbf{U}')+\nabla'p'=0$$

Defining $Re=\dfrac{U_o\rho_o L_o}{\mu}$, the non-dimensional momentum equation becomes:

$$\frac{\partial\rho'\mathbf{U}'}{\partial t'}+\nabla'\cdot(\rho'\mathbf{U}'\mathbf{U}')-\frac{1}{Re}\nabla'\cdot(\nabla'\mathbf{U}')+\nabla'p'=0$$

Summary of equations:

$$\nabla' \cdot \mathbf{U}' = 0$$

$$\frac{\partial \rho' \mathbf{U}'}{\partial t'} + \nabla' \cdot (\rho' \mathbf{U}' \mathbf{U}') - \frac{1}{Re} \nabla' \cdot (\nabla' \mathbf{U}') + \nabla' p' = 0$$

Summary of scale factors and non-dimensional numbers:

$$p_o = \rho_o U_o^2$$

$$U_o = L_o / t_o$$

$$Re = \frac{U_o \rho_o L_o}{\mu}$$

4.2.2 Lorentz force

The momentum source in Navier-Stokes equation due to electromagnetic force is the Lorentz force. The Lorentz force density $\mathbf{F}$ is the Lorentz force per unit volume which has the unit of N/m^3 [7, 32].

$$\mathbf{F} = \mathbf{J} \times \mathbf{B}$$

It will be useful to cast the Lorenz force purely in terms of magnetic field [5]. From Ampere's law :

$$\mathbf{F} = \left(\frac{\nabla \times \mathbf{B}}{\mu_0} \right) \times \mathbf{B}$$

Using vector identity A.5

$$\mathbf{F} = -\frac{1}{\mu_0} \mathbf{B} \times (\nabla \times \mathbf{B})$$

Using vector identity A.9, Lorentz force becomes

$$\mathbf{F} = -\nabla \left(\frac{B^2}{2\mu_0} \right) + \frac{1}{\mu_0} (\mathbf{B}.\nabla)\mathbf{B}$$

Using vector identity A.11

$$\mathbf{F} = -\nabla \left(\frac{B^2}{2\mu_0} \right) + \frac{1}{\mu_0} \left(\nabla \cdot (\mathbf{B}\ \mathbf{B}) - (\nabla \cdot \mathbf{B}\ )\mathbf{B}\ \right)$$

Letting $\nabla \cdot \mathbf{B}\ = 0$

$$\mathbf{F} = -\nabla \left(\frac{B^2}{2\mu_0} \right) + \nabla \cdot \left(\frac{1}{\mu_0} \mathbf{B}\mathbf{B} \right)$$

The last equation represents Lorentz force in conservative form.

4.2.3 Navier-Stokes Equations for Conducting Fluids

Electrically conducting fluids experience the Lorentz force in presence of electromagnetic fields. To account for this additional body force, the fluid momentum equation needs to be modified [5, 32].

In the $\mathbf{J} \times \mathbf{B}$ formulation, the modified fluid momentum equation is given by:

$$\frac{\partial \rho \mathbf{U}}{\partial t} + \nabla \cdot (\rho \mathbf{U}\mathbf{U}) - \mu \nabla \cdot (\nabla \mathbf{U}) + \nabla p - \mathbf{J} \times \mathbf{B} = 0$$

Alternatively, in the $\mathbf{B}$ formulation, the modified fluid momentum equation becomes:

$$\frac{\partial \rho \mathbf{U}}{\partial t} + \nabla \cdot (\rho \mathbf{U}\mathbf{U}) - \mu \nabla \cdot (\nabla \mathbf{U}) + \nabla p + \nabla \left(\frac{B^2}{2\mu_0} \right) - \nabla \cdot \left(\frac{1}{\mu_0} \mathbf{B}\mathbf{B} \right) = 0$$

These equations capture the impact of electromagnetic fields on the fluid flow dynamics.

4.2.4 Non-Dimensional form of Navier-Stokes Equations for Conducting Fluids

In the $\mathbf{J} \times \mathbf{B}$ formulation, following the same procedure as in previous chapters, the non-dimensionalized momentum equation becomes:

$$\left(\frac{\rho_o}{t_o}\frac{L_o}{t_o}\right)\frac{\partial \rho' \mathbf{U}'}{\partial t'} + \left(\frac{1}{L_o}\rho_o\frac{L_o}{t_o}\frac{L_o}{t_o}\right)\nabla' \cdot (\rho' \mathbf{U}'\mathbf{U}') - \mu\left(\frac{1}{L_o}\frac{1}{L_o}\frac{L_o}{t_o}\right)\nabla' \cdot (\nabla' \mathbf{U}') + \left(\frac{1}{L_o}p_o\right)\nabla' p' - (J_o B_o)\,\mathbf{J}' \times \mathbf{B}' = 0$$

The term $J_o B_o$ can be expressed as follows:

$$J_o B_o = \sigma_o E_o B_o = \sigma_o \frac{\Phi_o}{L_o} B_o$$

Since $A_o = \mu_o \sigma_o L_o \Phi_o$ and $B_o = A_o / L_o$,

$$J_o B_o = \frac{B_o^2}{\mu_o L_o}$$

$$\left(\frac{\rho_o}{t_o}\frac{L_o}{t_o}\right)\frac{\partial \rho' \mathbf{U}'}{\partial t'} + \left(\frac{1}{L_o}\rho_o\frac{L_o}{t_o}\frac{L_o}{t_o}\right)\nabla' \cdot (\rho' \mathbf{U}'\mathbf{U}') - \mu\left(\frac{1}{L_o}\frac{1}{L_o}\frac{L_o}{t_o}\right)\nabla' \cdot (\nabla' \mathbf{U}') + \left(\frac{1}{L_o}p_o\right)\nabla' p' - \frac{B_o^2}{\mu_o L_o}\,\mathbf{J}' \times \mathbf{B}' = 0$$

By dividing by $(\rho_o L_o / t_o^2)$:

$$\frac{\partial \rho' \mathbf{U}'}{\partial t'} + \nabla' \cdot (\rho' \mathbf{U}'\mathbf{U}') - \left(\frac{\mu}{U_o \rho_o L_o}\right)\nabla' \cdot (\nabla' \mathbf{U}') + \left(\frac{p_o}{\rho_o U_o^2}\right)\nabla' p' - \left(\frac{t_o^2}{\rho_o L_o}\frac{B_o^2}{\mu_o L_o}\right)\mathbf{J}' \times \mathbf{B}' = 0$$

The term $\left(\frac{t_o^2}{\rho_o L_o}\frac{B_o^2}{\mu_o L_o}\right)$ can be simplified as follows

$$
\begin{aligned}
\frac{t_o^2}{\rho_o L_o}\frac{B_o^2}{\mu_o L_o} &= \frac{L_o^2}{U_o^2 \rho_o L_o}\frac{B_o^2}{\mu_o L_o} \\
&= \frac{\mu}{U_o \rho_o L_o}\frac{B_o^2 L_o^2}{\mu \mu_o L_o U_o} \\
&= \frac{\mu}{U_o \rho_o L_o}\frac{B_o^2 L_o^2 \sigma_o}{\mu}\frac{1}{\mu_o \sigma_o L_o U_o} \\
&= \frac{1}{Re} Ha^2 \frac{1}{Re_m}
\end{aligned}
$$

Here, Ha is Hartmann number, dimensionless parameter that characterizes the strength of the magnetic field relative to the viscous forces in the fluid.

$$
Ha = B_o L_o \sqrt{\frac{\sigma_o}{\mu}}
$$

Using inertial scaling for pressure, the non-dimensional momentum equation is

$$
\frac{\partial \rho' \mathbf{U}'}{\partial t'} + \nabla' \cdot (\rho' \mathbf{U}' \mathbf{U}') - \frac{1}{Re} \nabla' \cdot (\nabla' \mathbf{U}') + \nabla' p' - \frac{Ha^2}{Re\, Re_m} \mathbf{J}' \times \mathbf{B}' = 0
$$

In the $\mathbf{B}$ formulation, the momentum equation in terms of non-dimensional variable becomes

$$
\begin{aligned}
\left(\frac{\rho_o}{t_o}\frac{L_o}{t_o}\right)\frac{\partial \rho' \mathbf{U}'}{\partial t'} + \left(\frac{1}{L_o}\rho_o \frac{L_o}{t_o}\frac{L_o}{t_o}\right)\nabla' \cdot (\rho' \mathbf{U}' \mathbf{U}') - \mu \left(\frac{1}{L_o}\frac{1}{L_o}\frac{L_o}{t_o}\right)\nabla' \cdot (\nabla' \mathbf{U}') + \left(\frac{1}{L_o} p_o\right)\nabla' p' \\
+ \left(\frac{1}{\mu_0}\frac{1}{L_o} B_o^2\right)\nabla \left(\frac{B'^2}{2}\right) - \left(\frac{1}{\mu_0}\frac{1}{L_o} B_o^2\right)\nabla \cdot (\mathbf{B}' \mathbf{B}') = 0
\end{aligned}
$$

Dividing by $(\rho_o L_o/t_o^2)$:

$$\frac{\partial \rho' \mathbf{U}'}{\partial t'} + \nabla' \cdot (\rho' \mathbf{U}' \mathbf{U}') - \left(\frac{\mu}{U_o \rho_o L_o}\right) \nabla' \cdot (\nabla' \mathbf{U}') + \left(\frac{p_o}{\rho_o U_o^2}\right) \nabla' p' + \left(\frac{t_o^2}{\rho_o L_o}\frac{B_o^2}{\mu_0 L_o}\right) \nabla \left(\frac{B'^2}{2}\right) - \left(\frac{t_o^2}{\rho_o L_o}\frac{B_o^2}{\mu_0 L_o}\right) \nabla \cdot (\mathbf{B}'\mathbf{B}') = 0$$

The non-dimensional momentum equation is

$$\frac{\partial \rho' \mathbf{U}'}{\partial t'} + \nabla' \cdot (\rho' \mathbf{U}' \mathbf{U}') - \frac{1}{Re} \nabla' \cdot (\nabla' \mathbf{U}') + \nabla' p' + \frac{Ha^2}{Re\, Re_m} \nabla \left(\frac{B'^2}{2}\right) - \frac{Ha^2}{Re\, Re_m} \nabla \cdot (\mathbf{B}'\mathbf{B}') = 0$$

Summary of equations:

In $\mathbf{J} \times \mathbf{B}$ formulation,

$$\frac{\partial \rho' \mathbf{U}'}{\partial t'} + \nabla' \cdot (\rho' \mathbf{U}' \mathbf{U}') - \frac{1}{Re} \nabla' \cdot (\nabla' \mathbf{U}') + \nabla' p' - \frac{Ha^2}{Re\, Re_m} \mathbf{J}' \times \mathbf{B}' = 0$$

In $\mathbf{B}$ formulation,

$$\frac{\partial \rho' \mathbf{U}'}{\partial t'} + \nabla' \cdot (\rho' \mathbf{U}' \mathbf{U}') - \frac{1}{Re} \nabla' \cdot (\nabla' \mathbf{U}') + \nabla' p' + \frac{Ha^2}{Re\, Re_m} \nabla \left(\frac{B'^2}{2}\right) - \frac{Ha^2}{Re\, Re_m} \nabla \cdot (\mathbf{B}'\mathbf{B}') = 0$$

4.3 Maxwell-Navier-Stokes System

The Maxwell-Navier-Stokes system of equations can be formulated by integrating the suitable Maxwell systems, with the Navier-Stokes equations for conducting liquids, which were derived in earlier sections. The prime notation, indicating non-dimensional quantities, has been removed for clarity. All quantities in the equations are still non-dimensional.

4.3.1 Maxwell-Navier-Stokes With Steady Fields

$$\nabla \cdot \sigma \nabla \Phi - Re_m \, \nabla \cdot (\sigma \mathbf{U} \times \mathbf{B}) = 0$$

$$\nabla \cdot \nabla \mathbf{A} - \sigma \nabla \Phi + Re_m \, \sigma \, (\mathbf{U} \times \mathbf{B}) = 0$$

$$\nabla \cdot \mathbf{U} = 0$$

$$\frac{\partial \rho \mathbf{U}}{\partial t} + \nabla \cdot (\rho \mathbf{U}\mathbf{U}) - \frac{1}{Re} \nabla \cdot (\nabla \mathbf{U}) + \nabla p + \frac{Ha^2}{Re\, Re_m} \nabla \left(\frac{B^2}{2} \right) - \frac{Ha^2}{Re\, Re_m} \nabla \cdot (\mathbf{B}\mathbf{B}) = 0$$

This model neglects the unsteadiness in the electromagnetic field due to the unsteady velocity field. Here $\mathbf{B} = \nabla \times \mathbf{A}$.

4.3.2 Maxwell-Navier-Stokes With Unsteady Fields

$$\nabla' \cdot \sigma' \nabla' \Phi' + Re_m \, \nabla' \cdot \left(\sigma' \frac{\partial \mathbf{A}'}{\partial t'} \right) - Re_m \, \nabla' \cdot (\sigma' \mathbf{U}' \times \mathbf{B}') = 0$$

$$R_m \, \sigma' \frac{\partial \mathbf{A}'}{\partial t'} - \nabla' \cdot \nabla' \mathbf{A}' + \sigma' \nabla' \Phi' - R_m \, \sigma' \mathbf{U}' \times \mathbf{B}' = 0$$

$$\nabla \cdot \mathbf{U} = 0$$

$$\frac{\partial \rho \mathbf{U}}{\partial t} + \nabla \cdot (\rho \mathbf{U}\mathbf{U}) - \frac{1}{Re} \nabla \cdot (\nabla \mathbf{U}) + \nabla p + \frac{Ha^2}{Re\, Re_m} \nabla \left(\frac{B^2}{2} \right) - \frac{Ha^2}{Re\, Re_m} \nabla \cdot (\mathbf{B}\mathbf{B}) = 0$$

4.3.3 Maxwell-Navier-Stokes With Steady Fields for electrically driven flows

In the systems previously discussed, the magnetic field arises solely from an applied current, with no external magnetic fields introduced. However, in electrically driven flows, such as those detailed in Khalzov (2008) [26], both an applied current, denoted as $\mathbf{J} = \mathbf{J}_{ap}$, and an external magnetic field, represented as $\mathbf{B} = \mathbf{B}_{ext}$, are present. In these scenarios, the Lorentz force is given by $\mathbf{F} = \mathbf{J} \times \mathbf{B} = \mathbf{J}_{ap} \times \mathbf{B}_{ext}$. To understand the dynamics of such systems, the following set of equations can be employed:

The evolution equation for the applied current is given by:

$$\nabla \cdot \sigma \nabla \Phi - \nabla \cdot (\sigma \mathbf{U} \times \mathbf{B}) = 0$$

The current density, $\mathbf{J}$, can then be calculated as: $\mathbf{J} = -\sigma \nabla \Phi + \sigma \mathbf{U} \times \mathbf{B}$. Similarly, the evolution equation for the applied magnetic field (Note that source due to applied current is removed) is given by:

$$\nabla \cdot \nabla \mathbf{A} + \mu_0 \sigma (\mathbf{U} \times \mathbf{B}) = 0$$

The magnetic field, $\mathbf{B}$, can be updated using: $\mathbf{B} = \nabla \times \mathbf{A}$. Although not necessary for the current analysis, if deemed essential for further investigation, the magnetic field resulting from the applied current can also be calculated using the Poisson equation for the vector potential:

$$\nabla \cdot \nabla \mathbf{A}_J = -\mu_0 \mathbf{J}$$

Magnetic field is then calculated based on curl of vector potential, $\mathbf{B}_J = \nabla \times \mathbf{A}_J$.

The Navier-Stokes equations remain unchanged and are expressed as:

$$\nabla \cdot \mathbf{U} = 0$$

$$\frac{\partial \rho \mathbf{U}}{\partial t} + \nabla \cdot (\rho \mathbf{U}\mathbf{U}) - \mu \nabla \cdot (\nabla \mathbf{U}) + \nabla p - \mathbf{J} \times \mathbf{B} = 0$$

These equations describe the evolution of the applied current, magnetic field, and fluid flow in the system under consideration.

Non-Dimensional Form : The non-dimensional equations for electrically driven flows differ from those previously derived. This section will focus on deriving the non-dimensional equations specific to electrically driven flows.

The non-dimensional form of the Maxwell equations is derived by introducing length scale L_o, electric conductivity scale σ_o, electric potential scale Φ_o, velocity scale U_o, magnetic field scale B_o. Note that the scale factor for magnetic field is based on externally applied magnetic field strength and by using the definition $\mathbf{B} = \nabla \times \mathbf{A}$, vector potential scale can be written as $A_o = B_o\, L_o$.

The non-dimensional quantities ∇', σ', Φ', $\mathbf{A}'$, $\mathbf{B}'$,$\mathbf{U}'$ to correspond to ∇, σ, Φ, $\mathbf{A}$, $\mathbf{B}$, $\mathbf{U}$. The relationships among scale factors, dimensional and non-dimensional quantities is given as: $\nabla' = \dfrac{\nabla}{\nabla_o}$, $\sigma' = \dfrac{\sigma}{\sigma_o}$, $\Phi' = \dfrac{\Phi}{\Phi_o}$, $\mathbf{A}' = \dfrac{\mathbf{A}}{A_o}$, $\mathbf{B}' = \dfrac{\mathbf{B}}{B_o}$, $\mathbf{U}' = \dfrac{\mathbf{U}}{U_o}$.

Evolution Equation for Applied Current : In terms of non-dimensional quantities and scale factors, the electric potential equation takes the form:

$$\left(\frac{1}{L_o}\,\sigma_o\,\frac{1}{L_o}\,\Phi_o\right)\nabla' \cdot \sigma'\nabla'\Phi' - \left(\frac{1}{L_o}\,\sigma_o\,U_o B_o\right)\nabla' \cdot (\sigma'\mathbf{U}' \times \mathbf{B}') = 0$$

Utilizing Ohm's law, the equation can be expressed as:

$$\left(\frac{1}{L_o}\sigma_o E_o\right)\nabla'\cdot\sigma'\nabla'\Phi' - \left(\frac{1}{L_o}\sigma_o U_o B_o\right)\nabla'\cdot(\sigma'\mathbf{U}'\times\mathbf{B}') = 0$$

In electrically driven flows, velocity isn't determined by a specific boundary condition. Instead, the fluid's motion is a result of the Lorentz force. This means there isn't a direct velocity scale. From the given equation, it can be made non-dimensional when $E_o = U_o B_o$.

$$\left(\frac{1}{L_o}\sigma_o U_o B_o\right)\nabla'\cdot\sigma'\nabla'\Phi' - \left(\frac{1}{L_o}\sigma_o U_o B_o\right)\nabla'\cdot(\sigma'\mathbf{U}'\times\mathbf{B}') = 0$$

The simplified form of the equation becomes:

$$\nabla'\cdot\sigma'\nabla'\Phi' - \nabla'\cdot(\sigma'\mathbf{U}'\times\mathbf{B}') = 0$$

As mentioned previously, although not necessary for the current analysis, the magnetic field resulting from the applied current can still be computed for further investigation if required. The following current densities are defined for clarity. The current density due to applied potential is

$$\mathbf{J}'_\phi = -\sigma'\nabla'\Phi'$$

The induced current due to the motion of the conducting liquid is

$$\mathbf{J}_u{}' = \sigma'\mathbf{U}'\times\mathbf{B}'$$

The total current is $\mathbf{J}' = \mathbf{J}'_\phi + \mathbf{J}_u{}'$. The magnetic field due to current is then calculated by first solving Poisson equation for vector potential

$$\nabla'\cdot\nabla'\mathbf{A}'_J = -\mathbf{J}'$$

And taking curl of the potential again

$$\mathbf{B}_J = \nabla' \times \mathbf{A}'_J$$

Evolution Equation External Magnetic Field : In terms of non-dimensional quantities and scale factors, magnetic vector potential equation takes the form:

$$\left(\frac{1}{L_o}\frac{1}{L_o}A_o\right)\nabla' \cdot \nabla'\mathbf{A}' + \left(\mu_0\sigma_o U_o \frac{A_o}{L_o}\right)\sigma'\left(\mathbf{U}' \times \mathbf{B}'\right) = 0$$

Multiplying the entire equation by $\dfrac{L_o^2}{A_o}$, it becomes:

$$\nabla' \cdot \nabla'\mathbf{A}' + \left(\mu_0\sigma_o U_o L_o\right)\sigma'\left(\mathbf{U}' \times \mathbf{B}'\right) = 0$$

Using the definition of magnetic Reynolds number relating to velocity of the conductor, $Re_m = \mu_0\sigma_o U_o L_o$,

$$\nabla' \cdot \nabla'\mathbf{A}' + Re_m\,\sigma'\left(\mathbf{U}' \times \mathbf{B}'\right) = 0$$

In numerical simulations, the test cases correspond to scenarios with a low magnetic Reynolds number, where $Re_m \ll 1$. In these cases, the equation simplifies to:

$$\nabla' \cdot \nabla'\mathbf{A}' = 0$$

Hence, in such cases where the initial magnetic field is fully diffused throughout the domain, the equation above need not be solved as the magnetic vector potential and the external magnetic field remain constant during the simulation.

Momentum Equation : Using $\mathbf{J} \times \mathbf{B}$ formulation and following the same procedure as in previous sections, the non-dimensionalized momentum equation becomes:

$$\left(\frac{\rho_o}{t_o}\frac{L_o}{t_o}\right)\frac{\partial \rho' \mathbf{U}'}{\partial t'} + \left(\frac{1}{L_o}\rho_o \frac{L_o}{t_o}\frac{L_o}{t_o}\right)\nabla' \cdot (\rho' \mathbf{U}'\mathbf{U}') - \mu \left(\frac{1}{L_o}\frac{1}{L_o}\frac{L_o}{t_o}\right)\nabla' \cdot (\nabla' \mathbf{U}') + \left(\frac{1}{L_o}p_o\right)\nabla' p' - (J_o B_o)\, \mathbf{J}' \times \mathbf{B}' = 0$$

The term $J_o B_o$ can be expressed as follows:

$$J_o B_o = \sigma_o E_o B_o = \sigma_o U_o B_o^2$$

$$\left(\frac{\rho_o}{t_o}\frac{L_o}{t_o}\right)\frac{\partial \rho' \mathbf{U}'}{\partial t'} + \left(\frac{1}{L_o}\rho_o \frac{L_o}{t_o}\frac{L_o}{t_o}\right)\nabla' \cdot (\rho' \mathbf{U}'\mathbf{U}') - \mu \left(\frac{1}{L_o}\frac{1}{L_o}\frac{L_o}{t_o}\right)\nabla' \cdot (\nabla' \mathbf{U}') + \left(\frac{1}{L_o}p_o\right)\nabla' p' - \sigma_o U_o B_o^2\, \mathbf{J}' \times \mathbf{B}' = 0$$

By dividing by $(\rho_o L_o / t_o^2)$, we obtain:

$$\frac{\partial \rho' \mathbf{U}'}{\partial t'} + \nabla' \cdot (\rho' \mathbf{U}'\mathbf{U}') - \left(\frac{\mu}{U_o \rho_o L_o}\right)\nabla' \cdot (\nabla' \mathbf{U}') + \left(\frac{p_o}{\rho_o U_o^2}\right)\nabla' p' - \left(\frac{t_o^2}{\rho_o L_o}\sigma_o U_o B_o^2\right)\mathbf{J}' \times \mathbf{B}' = 0$$

The term $\left(\frac{t_o^2}{\rho_o L_o}\sigma_o U_o B_o^2\right)$ can be simplified as:

$$\begin{aligned}\frac{t_o^2}{\rho_o L_o}\sigma_o U_o B_o^2 &= \frac{L_o^2}{U_o^2 \rho_o L_o}\sigma_o U_o B_o^2 \\ &= \frac{\mu}{U_o \rho_o L_o}\frac{B_o^2 L_o^2 \sigma_o}{\mu} \\ &= \frac{1}{Re}Ha^2\end{aligned}$$

The non-dimensional momentum equation is

$$\frac{\partial \rho' \mathbf{U}'}{\partial t'} + \nabla' \cdot (\rho' \mathbf{U}'\mathbf{U}') - \frac{1}{Re}\nabla' \cdot (\nabla' \mathbf{U}') + \nabla' p' - \frac{Ha^2}{Re}\mathbf{J}' \times \mathbf{B}' = 0$$

Summary of equations:

For low magnetic Reynolds number,

$$\nabla \cdot \sigma \nabla \Phi - \nabla \cdot (\sigma \mathbf{U} \times \mathbf{B}) = 0$$

$$\nabla \cdot \mathbf{U} = 0$$

$$\frac{\partial \rho \mathbf{U}}{\partial t} + \nabla \cdot (\rho \mathbf{U}\mathbf{U}) - \frac{1}{Re} \nabla \cdot (\nabla \mathbf{U}) + \nabla p - \frac{Ha^2}{Re} \mathbf{J} \times \mathbf{B} = 0$$

Here, $\mathbf{B}$ is constant.

In addition, magnetic field due to applied current can be calculated as

$$\mathbf{J}'_\phi = -\sigma' \nabla' \Phi'$$

$$\mathbf{J}_u{}' = \sigma{}' \mathbf{U}{}' \times \mathbf{B}{}'$$

The total current is $\mathbf{J}{}' = \mathbf{J}'_\phi + \mathbf{J}_u{}'$.

$$\nabla{}' \cdot \nabla{}' \mathbf{A}{}'_J = -\mathbf{J}{}'$$

$$\mathbf{B}_J = \nabla{}' \times \mathbf{A}{}'_J$$

4.3.4 Algorithm for Solving the Maxwell-Navier-Stokes Equation for Electrically Driven Flows

The Maxwell-Navier-Stokes Equations are solved employing the PISO (Pressure-Implicit with Splitting of Operators) algorithm [23, 25]. The procedure for each time step is outlined in the following sequence:

1. **Solve the Maxwell Equation**: Calculate the electric potential by solving the Poisson equation as follows:

$$\nabla \cdot \sigma \nabla \Phi - \nabla \cdot (\sigma \mathbf{U} \times \mathbf{B}) = 0$$

   In this equation, the term $\nabla \cdot (\sigma \mathbf{U} \times \mathbf{B})$ is an explicit source term.

2. **Momentum Predictor**: Estimate the velocity field $\mathbf{U}$ by solving the momentum equation. The pressure gradient term ∇p and the Lorentz force term $\mathbf{J} \times \mathbf{B}$ are incorporated as explicit source terms based on the initial conditions or values from the previous time step.

3. **Construct the H Operator**: The discretized momentum equation can be expressed as follows :

$$a_P \mathbf{U}_P + \sum_{N=1}^{nfaces} a_N \mathbf{U}_N = b_P$$

   Considering Rhie-Chow interpolation [25, 36, 55] , the momentum equation is discretized excluding the pressure gradient.

$$a_P \mathbf{U}_P + \sum_{N=1}^{nfaces} a_N \mathbf{U}_N = b_P - \nabla p$$

or, in a more simplified form: $a_P \mathbf{U}_P = \mathbf{H}[\mathbf{U}] - \nabla p$

where:

$$\mathbf{H}[\mathbf{U}] = b_P - \sum_{N=1}^{nfaces} a_N \mathbf{U}_N$$

4. **Construct and Solve the Pressure Equation**: The velocity obtained from the predictor step is given by the following equation:

$$\mathbf{U} = \frac{1}{a_P}\mathbf{H}[\mathbf{U}] - \frac{1}{a_P}\nabla p$$

Taking divergence of the equation and then setting the resultant expression to zero

$$\nabla \cdot \left(\frac{1}{a_P}\mathbf{H}[\mathbf{U}]\right) - \nabla \cdot \left(\frac{1}{a_P}\nabla p\right) = 0$$

This leads to a Poisson equation for the pressure. Solving this equation provides the pressure field necessary to correct the velocity field.

5. **Correct the Velocity Field**: Update the velocity field using the corrected pressure:

$$\mathbf{U} = \frac{1}{a_P}\mathbf{H}[\mathbf{U}] - \frac{1}{a_P}\nabla p$$

6. **Correct the Velocity Flux**: Compute the corrected velocity flux at the cell faces using Rhie-Chow interpolation:

$$\mathbf{U} \cdot \mathbf{S}_f = \left(\frac{1}{a_P}\mathbf{H}[\mathbf{U}]\right) \cdot \mathbf{S}_f - \left(\frac{1}{a_P}\nabla p\right) \cdot \mathbf{S}_f$$

Iterate steps 3 to 6 until convergence is achieved.

4.4 Numerical Simulations with Navier-Stokes Equations for Neutral Fluids

4.4.1 Numerical Simulation of Lid Driven Cavity Flow

This section examines the fluid dynamics of a lid-driven cavity flow, which serves as one of the classical problem for validating computational fluid dynamics algorithms [14, 39]. The computational model consists of a square cavity with a moving lid. The top boundary of the cavity moves at a constant velocity U_0, initiating shear-driven flow within the fluid. This setup creates a primary vortex within the cavity and possibly secondary vortices at the corners, depending on the Reynolds number of the flow. A schematic representation of this setup is shown in Figure 4.1. The cavity has a uniform depth of d with solid, no-slip walls on three sides and a moving no-slip lid on the top boundary. The steady state velocity profile is compared with with benchmark solutions reported in literature [14].

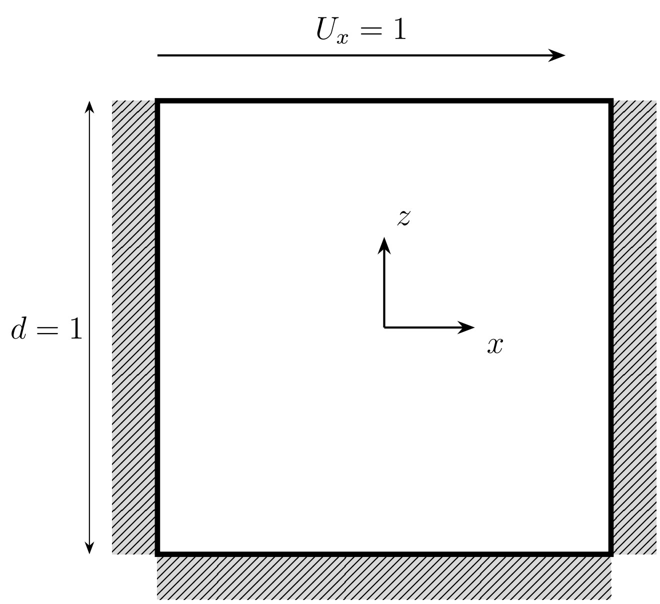

Figure 4.1: Sketch of computational domain used for numerical simulation of lid-driven cavity flow using Navier-Stokes equation. Dimensions are presented in non-dimensional form.

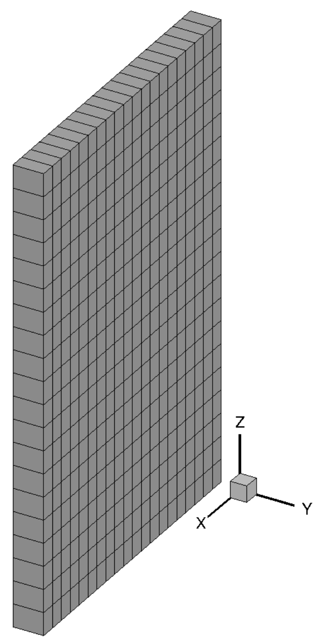

Figure 4.2: Computational mesh used for numerical simulation of lid-driven cavity flow using Navier-Stokes equation. The domain is a rectangular Cartesian grid with only one cell in the y-direction. Presented figure is a representative mesh, not the actual.

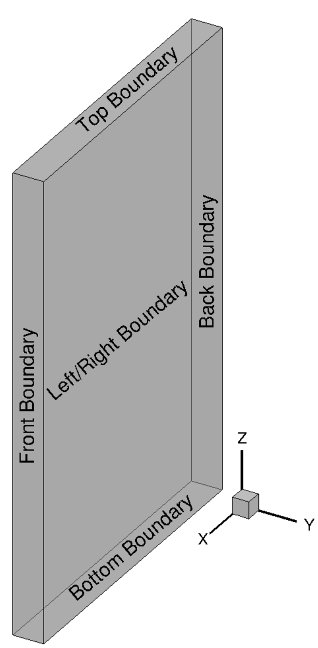

Figure 4.3: Boundary labels for the computational domain used for numerical simulation of lid-driven cavity flow using Navier-Stokes equation. Presented figure is representative and not to scale.

Table 4.1: Geometry, physical property and boundary condition parameters used for numerical simulation of lid-driven cavity flow using Navier-Stokes equation. All the parameters used are non-dimensional.

Parameter	Description	Value
d	Depth of square cavity	1.0
ρ	Density of the fluid	1.0
p	Pressure	1.0
ts	Total simulation time	1.0
Re	Reynolds number	1.0

Table 4.2: Boundary conditions used for numerical simulation of lid-driven cavity flow using Navier-Stokes equation.

	Boundary Condition	
Boundary	Velocity ($\mathbf{U}$)	Pressure (p)
Top boundary	Fixed value	Zero normal gradient
Bottom boundary	Fixed value	Zero normal gradient
Left boundary	Zero normal gradient	Zero normal gradient
Right boundary	Zero normal gradient	Zero normal gradient
Front boundary	Fixed value	Zero normal gradient
Back boundary	Fixed value	Zero normal gradient

Solution:

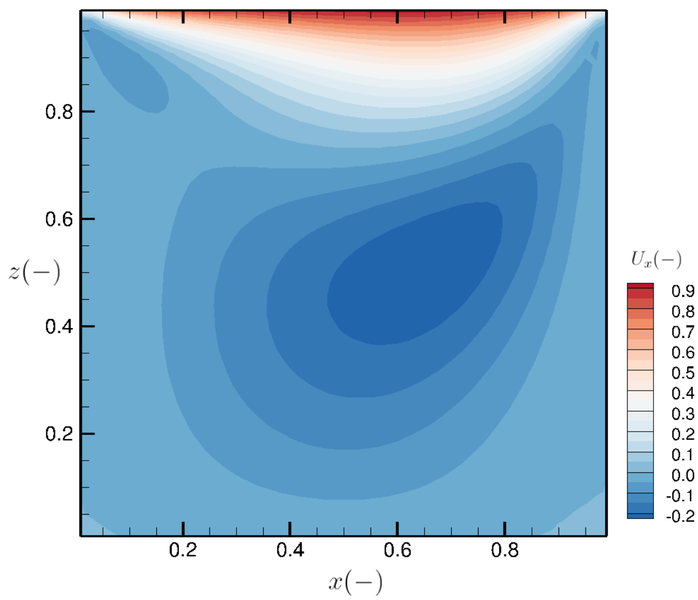

(a)

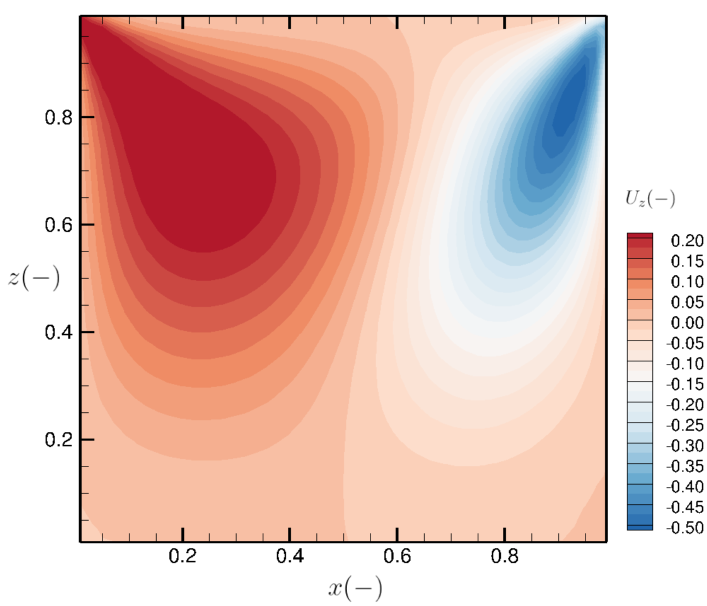

(b)

Figure 4.4: Simulation results of lid-driven cavity flow using Navier-Stokes equation. The figures display (a) non-dimensional U_x velocity and (b) non-dimensional U_z velocity.

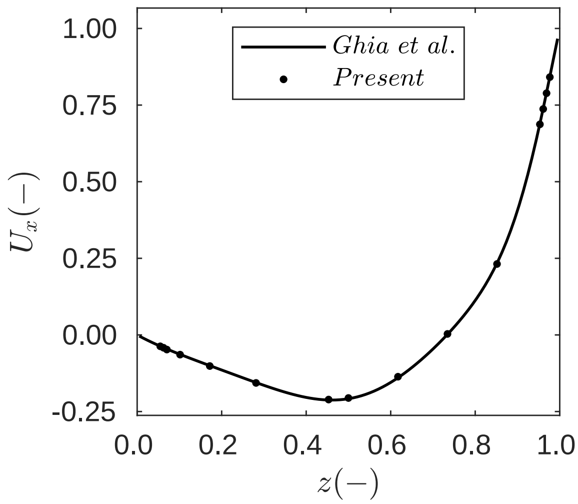

(a)

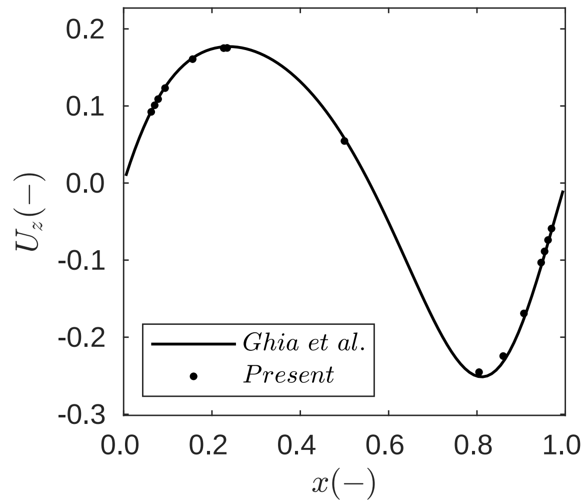

(b)

Figure 4.5: Comparison of the computed results for the lid-driven cavity flow with the benchmark study by Ghia et al. [14], using the Navier-Stokes equations. The figures display (a) velocity profile along the vertical central line (U_x versus z at $x = 0.5$), and (b) velocity profile along the horizontal central line (U_z versus x at $z = 0.5$).

Discretization Error in Numerical Solutions:

To verify the grid-independence of the current solutions, the U_x velocity profile is compared with benchmark solution using three different mesh sizes: (i) a coarse mesh, designated as M1, with a grid resolution of $N_x \times N_z = 11 \times 11$, (ii) an intermediate mesh, known as M2, with a grid resolution of $N_x \times N_z = 21 \times 21$, and (iii) a fine mesh, termed M3, with a grid resolution of $N_x \times N_z = 41 \times 41$. As the mesh is refined, the results show improved agreement with the benchmark solution. U_x velocity at the midpoint is considered for the calculation of error.

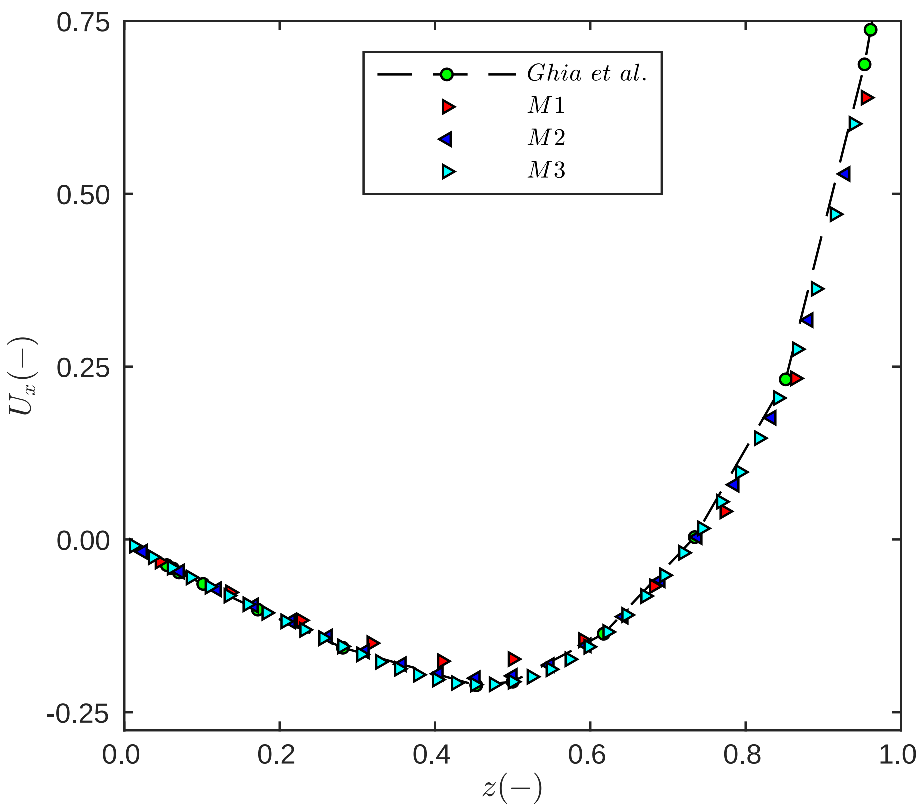

Figure 4.6: Mesh dependency on the U_x velocity profile in the simulation of lid-driven cavity flow using the Navier-Stokes equations.

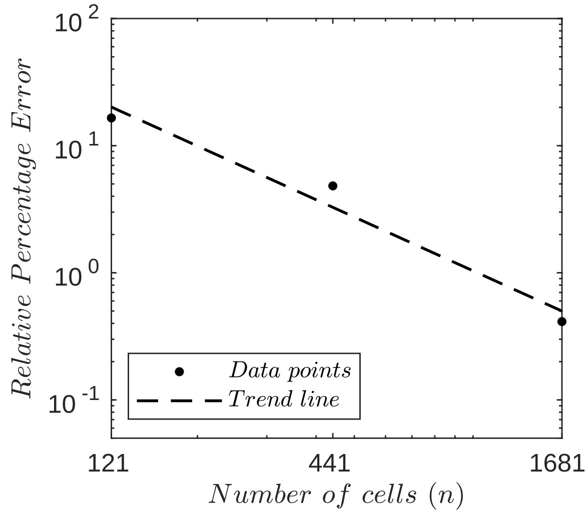

Figure 4.7: Comparison of true percentage relative error across varying mesh sizes in the simulation of lid-driven cavity flow using the Navier-Stokes equations. The variable n denotes the number of cells in each mesh size. The error exhibits a linear decrease and tends toward zero as n increases.

Order of accuracy : In Figure 4.7 logarithm of the grid size against the logarithm of the corresponding error is plotted. The calculated order of accuracy for the solver, based on the fitted line shown in Figure 4.7, is 1.4044.

4.5 Numerical Simulations with Maxwell-Navier-Stokes Equations

4.5.1 Numerical Simulation of Axisymmetric Electrically driven Flow in Annular Channel

This section provides a simulation study investigating the phenomena of liquid metal propelled by an applied electric current and transverse magnetic field. The simulation setup consists of two coaxial cylinders filled with liquid metal [43, 44]. A uniform axial magnetic field, referred to as B_z=B_o, permeates the liquid metal. When an electric current I_o is applied from the inner to the outer cylinder through the liquid metal medium, it triggers the metal to spin in azimuthal direction. A schematic illustration of this computational domain is depicted in Figure 4.8. The cylinder has a length of l and inner and outer radii of r_i and r_o respectively. Angular momentum along the z axis, away from the side walls, is compared with the exact solutions in literature [26, 46].

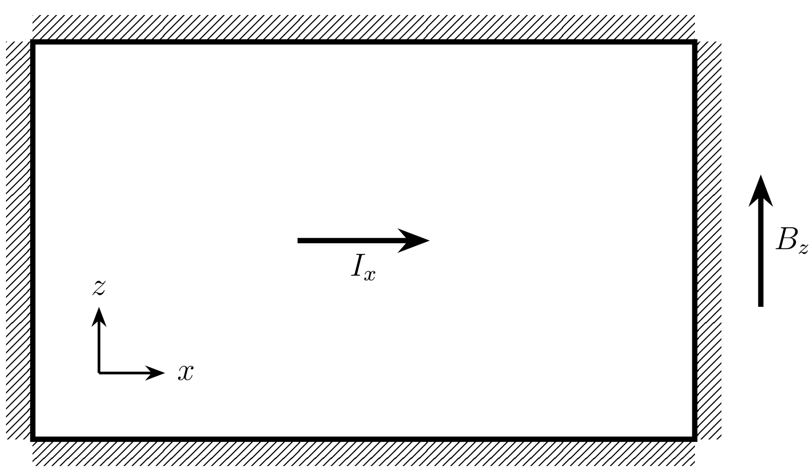

Figure 4.8: Sketch of computational domain used for numerical simulation of axisymmetric electrically driven flow in an annular channel. The picture is a cross section of an annular cylinder. The left and right surfaces correspond to the inner and outer radii of the cylinder.

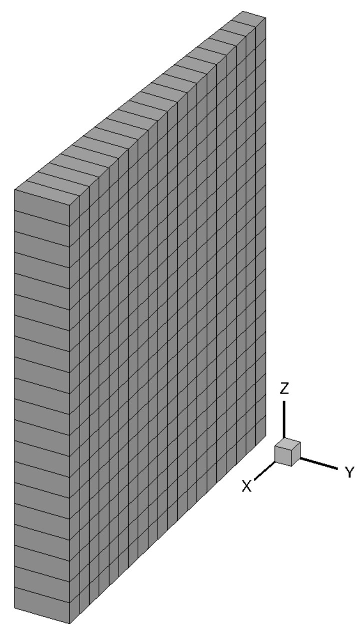

Figure 4.9: Computational mesh used for numerical simulation of axisymmetric electrically driven flow in annular channel. Presented figure is a representative mesh, not the actual.

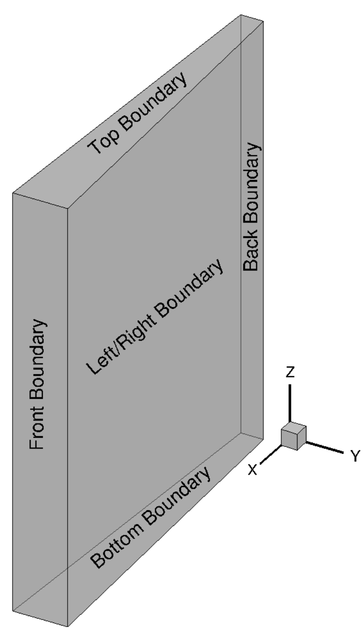

Figure 4.10: Boundary labels for the computational domain used for numerical simulation of axisymmetric electrically driven flow in annular channel. The left boundary corresponds to the front plane, and the right boundary is located on the other side of the geometry as shown. Presented figure is representative and not to scale.

For this test case, the dimensions of the setup are based on Khalzov's dissertation [26].

Table 4.3: Geometry, physical property and boundary condition parameters used for numerical simulation of axisymmetric electrically driven flow in annular channel. All the parameters used are non-dimensional.

Parameter	Description	Value
r_i	Inner radius of cylinder	1
r_o	Outer radius of cylinder	5
H	Height of cylinder	2.0
σ	Electrical conductivity	1.0
Φ_b	Potential at back boundary	$\frac{\ln(r_i/r_o)}{2\pi H\sigma}$
Φ_f	Potential at front boundary	0.0
$\mathbf{A}_{t/b}$	Vector potential at top and bottom boundary	0.0
B_z	Imposed External Magnetic Field	1.0
ρ	Density of the fluid	1.0
p	Pressure	1.0
ts	Total simulation time	1.0
Re	Reynolds number	1.0
Ha	Hartmann number	0.1

At the boundary wall, the velocity vector $\mathbf{U}$ becomes zero. In this scenario, the pressure force must counterbalance the Lorentz force. This relationship is expressed as:

$$\nabla p = \frac{Ha^2}{Re}\mathbf{J} \times \mathbf{B}$$

To determine the boundary condition for pressure, the momentum equation is projected onto the wall [25], providing insight into how the pressure behaves at the boundary.

Considering the component of this equation that's normal to the wall:

$$\nabla p \cdot \hat{n} = \frac{Ha^2}{Re} \left(\mathbf{J} \times \mathbf{B} \right) \cdot \hat{n}$$

In the given test case, the current at the boundaries is exclusively radial, while the external magnetic field remains purely axial throughout the domain. Hence the Lorentz force is purely in azimuthal direction. Given these conditions, the right-hand side of the equation becomes zero at the walls, leading to:

$$\nabla p \cdot \hat{n} = 0$$

Table 4.4: Boundary conditions used for numerical simulation of axisymmetric electrically driven flow in annular channel.

	Boundary Condition		
Boundary	Velocity ($\mathbf{U}$)	Pressure (p)	Potential (Φ)
Top boundary	Fixed value	Zero normal gradient	Zero normal gradient
Bottom boundary	Fixed value	Zero normal gradient	Zero normal gradient
Left boundary	Zero normal gradient	Zero normal gradient	Zero normal gradient
Right boundary	Zero normal gradient	Zero normal gradient	Zero normal gradient
Front boundary	Fixed value	Zero normal gradient	Fixed value
Back boundary	Fixed value	Zero normal gradient	Fixed value

Exact solution:

The focus is on identifying a steady-state solution for comparison with an analytical solution. The analysis particularly concerns the specific angular momentum of the conducting liquid. The specific angular momentum h of the conducting liquid in an annular channel [26, 46] is defined as follows:

$$h = r\,U_\theta$$

where

U_θ : azimuthal velocity,

r : radial coordinate.

The equilibrium solution for this electrically driven flow, especially in the central portion of the channel where the effects of the side walls can be disregarded, has been thoroughly discussed in Khalzov (2008) [26]. Within this core region, radial dependence can be neglected, and the angular momentum can be characterized as follows:

$$h(z) = \frac{\cosh(Ha\,z) - \cosh(Ha)}{\sinh(Ha)}$$

The results outlined in Khalzov (2008) [26] pertain to the current flowing from the outer cylinder to the inner cylinder. Conversely, the simulation discussed in this section deals with the current flowing from the inner cylinder to the outer cylinder, leading to a reversal in sign. The analytical solution for the magnetic field is also presented in terms of the poloidal stream function for current density in Khalzov's dissertation [26].

Solution:

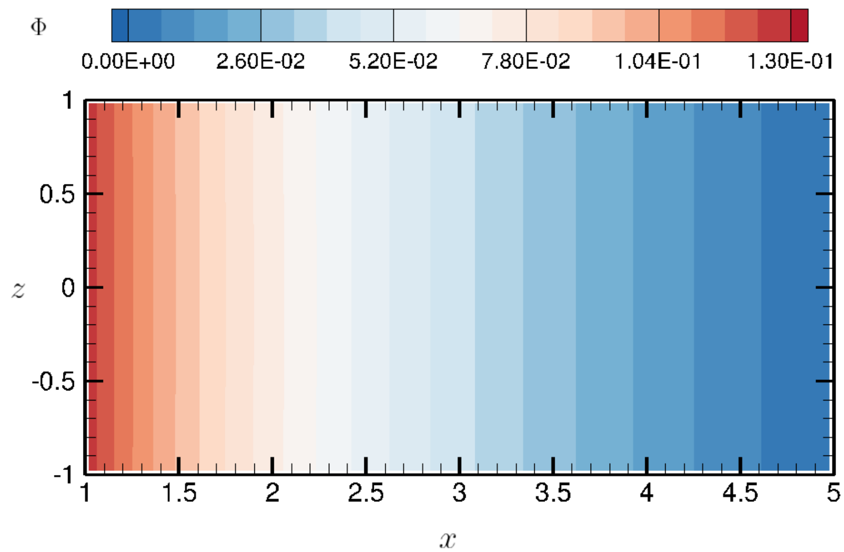

(a)

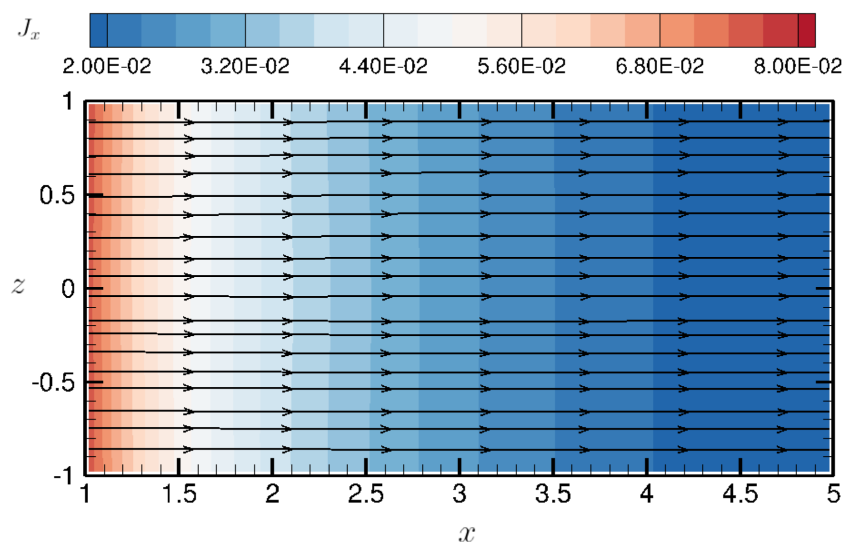

(b)

Figure 4.11: Simulation results of steady electrically driven flow in annular channel. The figures display (a) the electric potential, (b) stream lines of current density coloured with x component of current density. The variables presented in the plot are non-dimensional.

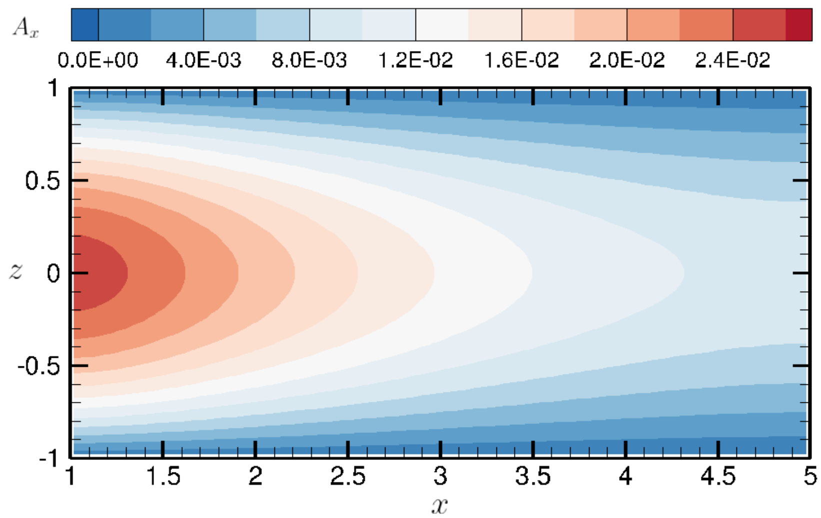

(a)

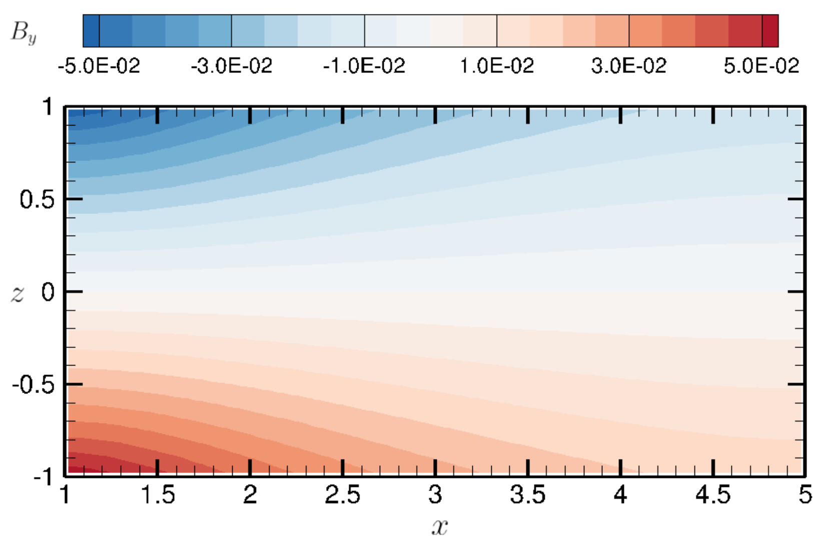

(b)

Figure 4.12: Simulation results of steady electrically driven flow in annular channel. The figures display (a) the magnetic vector potential, (b) the induced magnetic field due to applied current. The variables presented in the plot are non-dimensional.

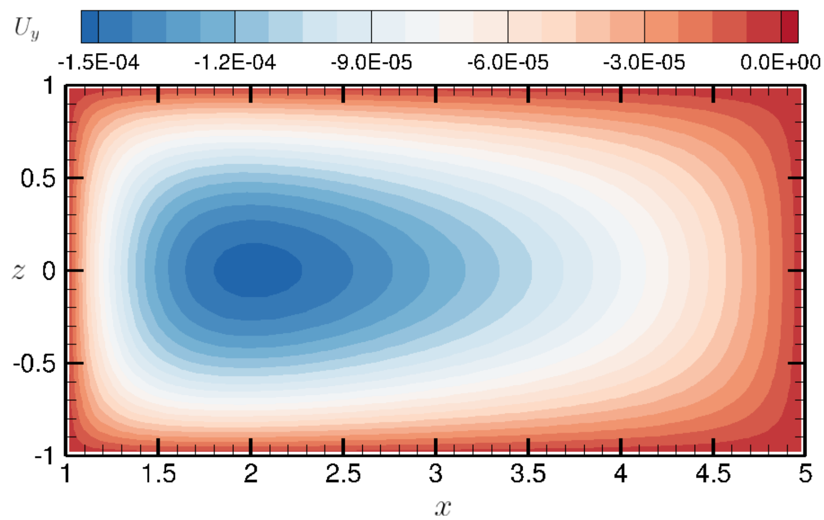

(a)

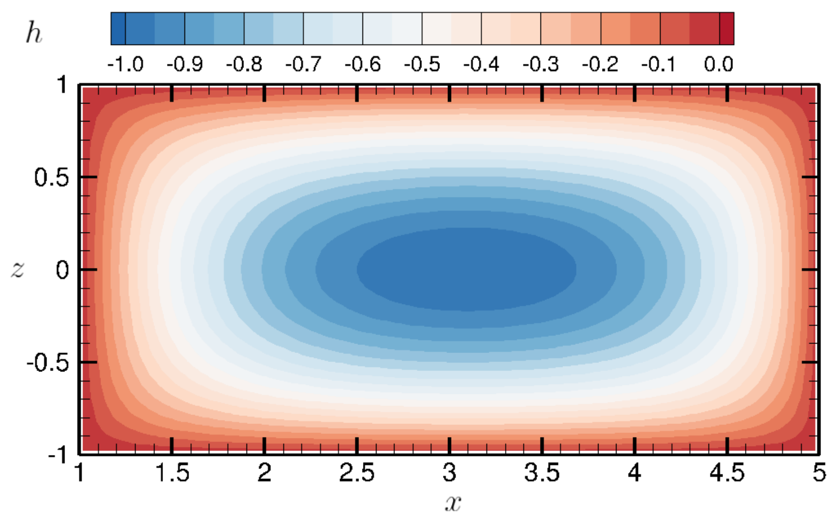

(b)

Figure 4.13: Simulation results of steady electrically driven flow in annular channel. The figures display (a) the azimuthal velocity field $U_y(U_\theta)$, (b) the angular momentum of the rotating fluid ($h = x\,U_y = r\,U_\theta$). The variables presented in the plot are non-dimensional.

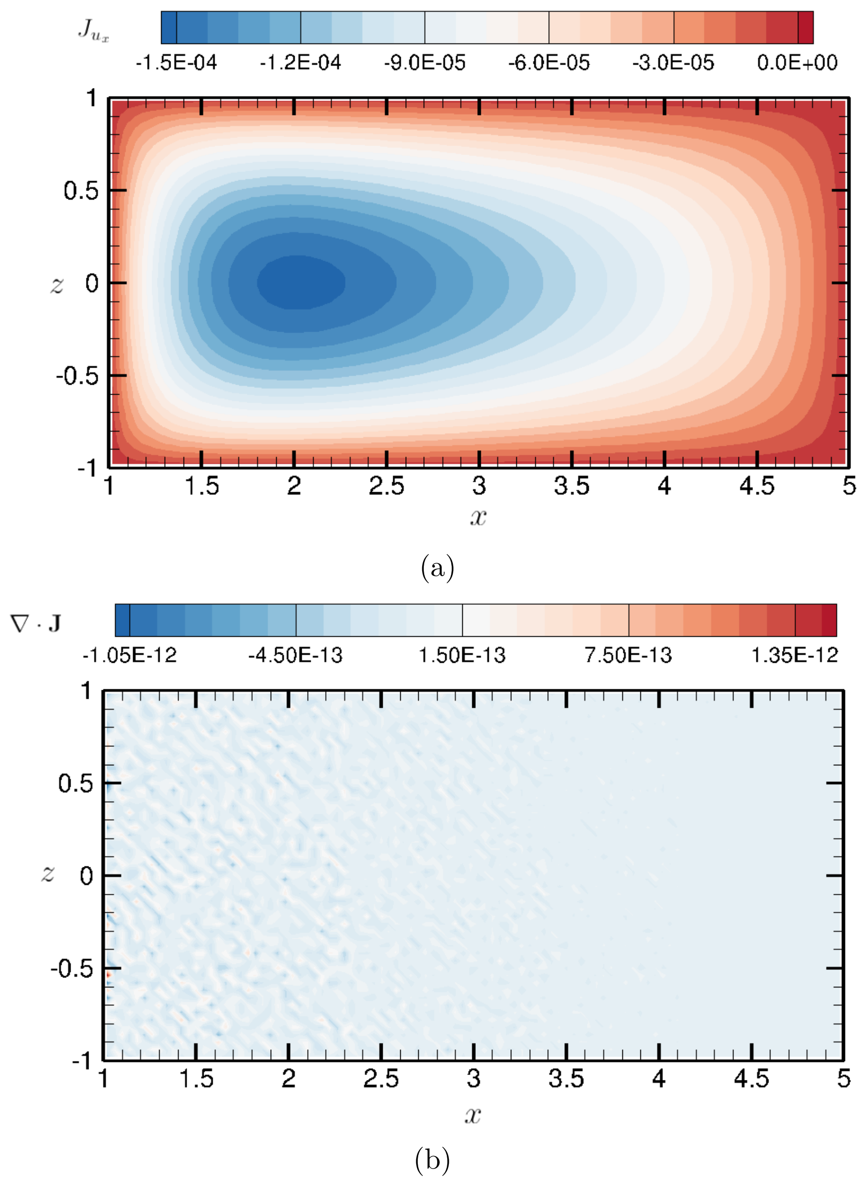

Figure 4.14: Simulation results of steady electrically driven flow in annular channel. The figures display (a) the induced current due to motion of the conducting liquid $\mathbf{J}_u = \sigma \mathbf{U} \times \mathbf{B}$, (b) divergence of current density. The variables presented in the plot are non-dimensional.

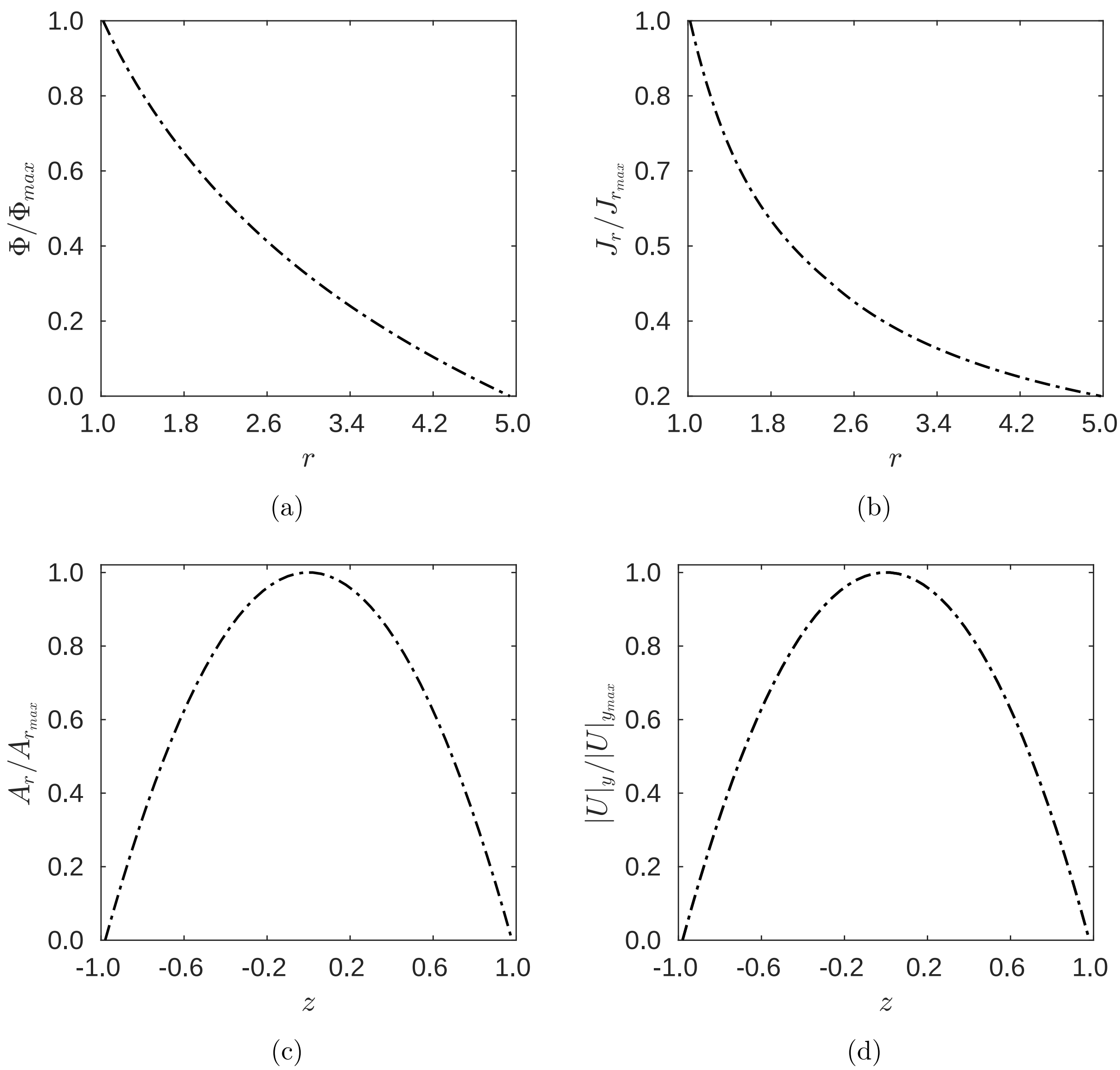

Figure 4.15: Simulation results of steady electrically driven flow in annular channel. The figures display (a) normalized electric potential, (b) normalized current density, (c) normalized vector potential, (d) absolute and normalized azimuthal velocity. The results display value along the vertical center-line away from side walls. The variables in the plot are presented in non-dimensional terms.

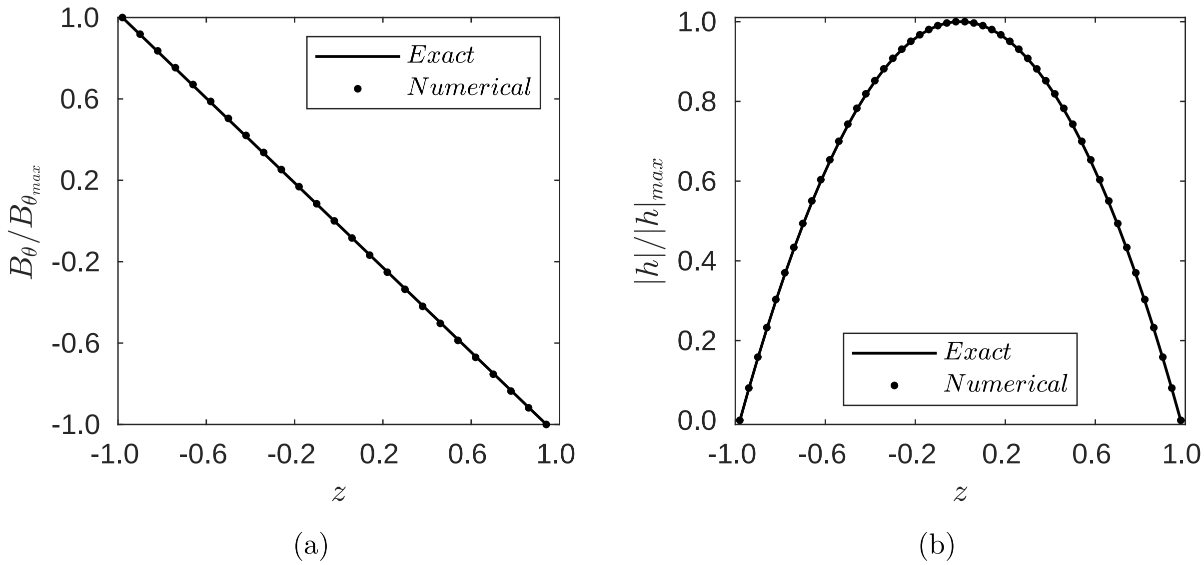

Figure 4.16: Comparison between the numerical and exact solutions for steady electrically driven flow in annular channel [26, 43, 44]. The figures display (a) normalized magnetic field due to current, (b) normalized absolute values of angular momentum. The variables in the plot are presented in non-dimensional terms.

Discretization Error in Numerical Solutions:

To verify the grid-independence of the current solutions, the angular momentum profile is compared with analytical solution using three different mesh sizes: (i) a coarse mesh, designated as M1, with a grid resolution of $N_x \times N_z = 11 \times 6$, (ii) an intermediate mesh, known as M2, with a grid resolution of $N_x \times N_z = 21 \times 10$, and (iii) a fine mesh, termed M3, with a grid resolution of $N_x \times N_z = 41 \times 20$. As the mesh is refined, the results show improved agreement with the analytical solution.

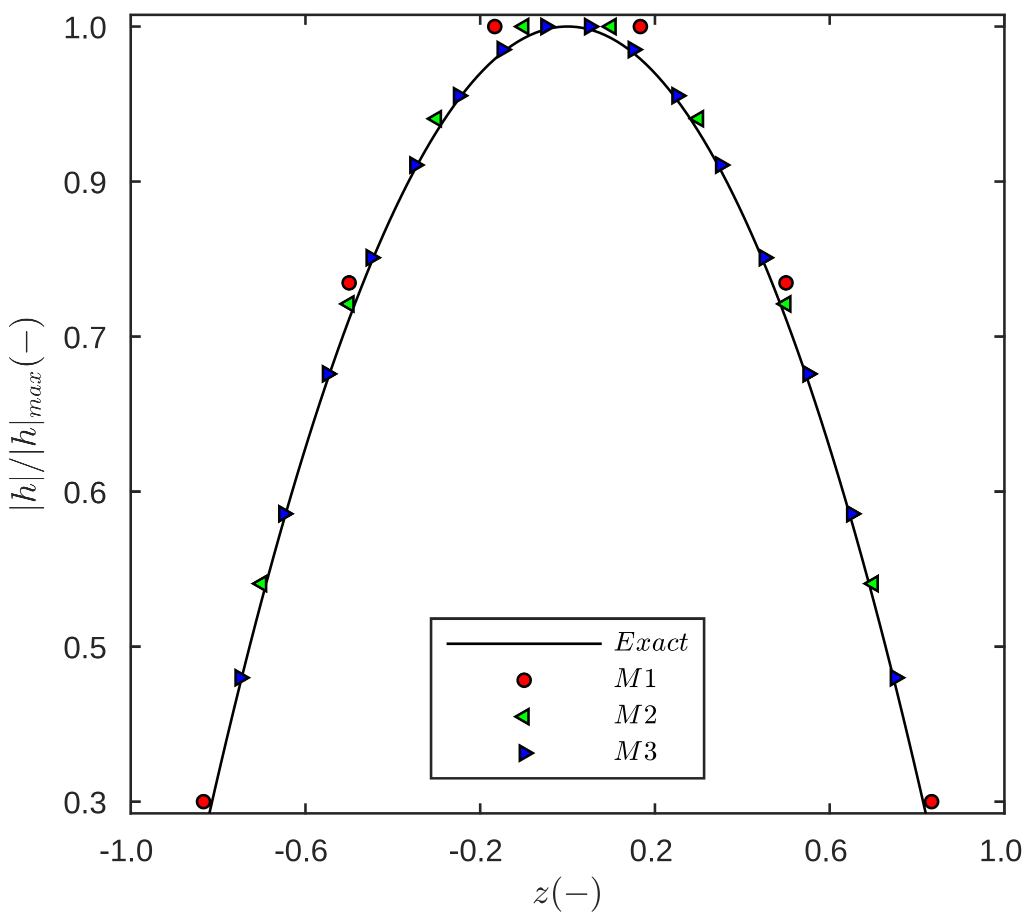

Figure 4.17: Mesh dependency on the angular momentum profile in the simulation of steady electrically driven flow in annular channel.

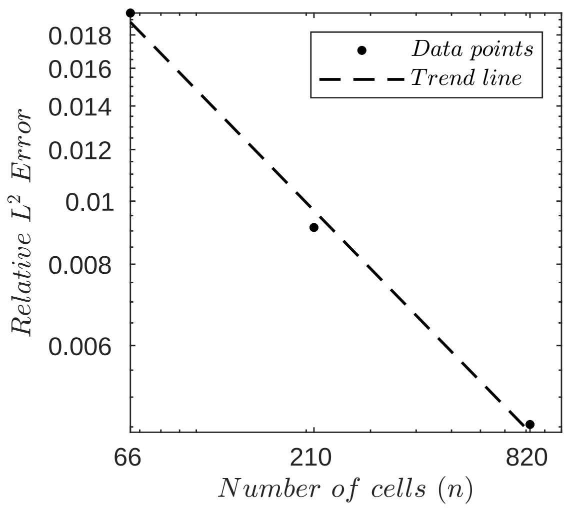

Figure 4.18: Comparison of L^2 error of angular momentum profile across varying mesh sizes in the simulation of steady electrically driven flow in annular channel. The variable n denotes the number of cells in each mesh size. The error exhibits a linear decrease and tends toward zero as n increases.

Order of accuracy : In Figure 4.18 logarithm of the grid size against the logarithm of the corresponding error is plotted. The calculated order of accuracy for the solver, based on the fitted line shown in Figure 4.18, is 0.575638. The numerical solution is compared with the exact solution provided in [26], where the governing equations differ. Khalzov's dissertation models magnetic fields using toroidal field components and poloidal flux functions, whereas this study employs magnetic fields and electric potentials. The observed order of accuracy is attributed to the different equations used in modeling the problem.

Chapter 5

Two-Phase Maxwell-Navier-Stokes Equations

5.1 Two-Phase Maxwell-Navier-Stokes Equations

This section aims to extend the governing equations for single-phase flows, discussed in the preceding chapter, to include two-phase electrically conducting flows. The system under study involves two distinct fluids, characterized by their respective volume fractions. Specifically, $\alpha = 0$ is indicative of an electrically non-conductive gaseous phase, while $\alpha = 1$ represents an electrically conductive liquid phase. Additionally, the equations take into account the influence of gravity.

In this section, the governing equations are specifically formulated for flows influenced by both electrical currents and external magnetic fields. The governing equations for scenarios involving purely electrical currents without external magnetic fields are detailed in the subsequent sections. The equations employ the steady-state form of Maxwell's equations.

The continuity equation can be expressed as follows:

$$\nabla \cdot \mathbf{U} = 0$$

The equation governing fluid momentum can be expressed as:

$$\frac{\partial \rho \mathbf{U}}{\partial t} + \nabla \cdot (\rho \mathbf{U}\mathbf{U}) - \nabla \cdot (\mu \nabla \mathbf{U}) + \nabla p - \rho \mathbf{g} - \mathbf{J} \times \mathbf{B} = 0$$

The density of the mixture ρ is calculated as:

$$\rho = \alpha \rho_l + (1 - \alpha)\rho_g$$

Here, ρ_l is the density of liquid and ρ_g is the density of gas. Similarly, the mixture's fluid viscosity and electrical conductivity can be calculated.

$$\mu = \alpha \mu_l + (1 - \alpha)\mu_g$$

$$\sigma = \alpha \sigma_l + (1 - \alpha)\sigma_g$$

The equation governing the temporal evolution of the liquid volume fraction is [8, 31, 50] :

$$\frac{\partial \alpha}{\partial t} + \nabla \cdot (\alpha \mathbf{U}) = 0$$

The steady Maxwell equations remain unchanged and are presented again here for completeness. For the applied electrical current, the governing equation is:

$$\nabla \cdot \sigma \nabla \Phi - \nabla \cdot (\sigma \mathbf{U} \times \mathbf{B}) = 0$$

Subsequently, the current density $\mathbf{J}$ is calculated as:

$$\mathbf{J} = -\sigma \nabla \Phi + \sigma \mathbf{U} \times \mathbf{B}$$

Likewise, the evolution equation for the applied magnetic field is formulated as:

$$\nabla \cdot \nabla \mathbf{A} + \mu_0 \sigma \left(\mathbf{U} \times \mathbf{B} \right) = 0$$

The magnetic field $\mathbf{B}$ is then updated using the curl of the vector potential $\mathbf{A}$:

$$\mathbf{B} = \nabla \times \mathbf{A}$$

5.1.1 Non-dimensional Form of governing equations:

The non-dimensional representation of the governing equations is obtained by introducing various scaling factors: density scale ρ_o, time scale t_o, length scale L_o, velocity scale U_o, viscosity scale μ_o, pressure scale p_o, the scale for acceleration due to gravity g_o, electric conductivity scale σ_o, electric potential scale Φ_o, magnetic vector potential scale A_o and magnetic field scale B_o.

Corresponding non-dimensional quantities ρ', t', ∇', $\mathbf{U}'$, μ', p', $\mathbf{g}'$, $\sigma\,'$, $\Phi\,'$, $\mathbf{A}\,'$, and $\mathbf{B}\,'$ are defined to relate to ρ, t, ∇, $\mathbf{U}$, μ, p, $\mathbf{g}$, σ, Φ, $\mathbf{A}$, and $\mathbf{B}$ respectively.

The relationships among the scaling factors, dimensional and non-dimensional quantities are expressed as: $\rho' = \dfrac{\rho}{\rho_o}$, $t' = \dfrac{t}{t_o}$, $\nabla' = \dfrac{\nabla}{\nabla_o}$, $\mathbf{U}' = \dfrac{\mathbf{U}}{U_o}$, $\mu' = \dfrac{\mu}{\mu_o}$, $p' = \dfrac{p}{p_o}$, $\mathbf{g}' = \dfrac{\mathbf{g}}{g_o}$, $\sigma\,' = \dfrac{\sigma}{\sigma_o}$, $\Phi\,' = \dfrac{\Phi}{\Phi_o}$, $\mathbf{A}\,' = \dfrac{\mathbf{A}}{A_o}$ and $\mathbf{B}\,' = \dfrac{\mathbf{B}}{B_o}$. Note that $\nabla_o = 1/L_o$ and $U_o = L_o/t_o$.

The scale factor for magnetic field is based on externally applied magnetic field strength and by using the definition $\mathbf{B} = \nabla \times \mathbf{A}$, vector potential scale can be written as $A_o = B_o\, L_o$.

Adopting the same procedure as for single-phase flows, the governing equation in its non-dimensional form becomes:

$$\nabla' \cdot \mathbf{U}' = 0$$

$$\frac{\partial \rho' \mathbf{U}'}{\partial t'} + \nabla' \cdot (\rho' \mathbf{U}' \mathbf{U}') - \frac{1}{Re} \nabla' \cdot (\mu' \nabla' \mathbf{U}') + \nabla' p' - \frac{1}{Fr^2} \rho' \mathbf{g}' - \frac{Ha^2}{Re} \mathbf{J} \times \mathbf{B} = 0$$

The non-dimensional form of Maxwell equations are given by

$$\nabla' \cdot \sigma' \nabla' \Phi' - \nabla' \cdot (\sigma' \mathbf{U}' \times \mathbf{B}') = 0$$

$$\nabla' \cdot \nabla' \mathbf{A}' + Re_m \, \sigma' (\mathbf{U}' \times \mathbf{B}') = 0$$

In numerical simulations, the test cases correspond to scenarios with a low magnetic Reynolds number. As discussed in previous chapter when $Re_m \ll 1$, the external magnetic field is not affected by the flow and can be considered constant. In addition following current densities are defined for clarity:

$$\mathbf{J}'_\phi = -\sigma' \nabla' \Phi'$$

$$\mathbf{J}_u{}' = \sigma' \mathbf{U}' \times \mathbf{B}'$$

The total current is $\mathbf{J}' = \mathbf{J}'_\phi + \mathbf{J}_u{}'$. Here Froude number, $Fr = \dfrac{U_o}{\sqrt{g_o L_o}}$

5.1.2 Algorithm for Solving the Two-Phase-Maxwell-Navier-Stokes Equation

PISO algorithm is employed to solve the two-phase Maxwell-Navier-Stokes equations at each time step. Following the same procedure for single phase flows, the pressure correction equation is given by

$$\nabla \cdot \left(\frac{1}{a_P} \nabla p \right) - \nabla \cdot \left(\frac{1}{a_P} \mathbf{H}[\mathbf{U}] \right) = 0$$

The above pressure Poisson equation is solved to get the pressure field p. The steps of the PISO algorithm for each timestep are outlined as follows:

Algorithm 1 PISO algorithm for two phase Maxwell-Navier-Stokes equations

1: Implicitly solve the momentum equation for $\mathbf{U}$ using old pressure and density fields

2: Construct $\mathbf{H}[\mathbf{U}]$ operator

3: Solve the pressure equation

4: Correct the velocity field using

$$\mathbf{U} = \frac{1}{a_P}\mathbf{H}[\mathbf{U}] - \frac{1}{a_P}\nabla p$$

5: Compute velocity flux at cell faces using RC Interpolation

$$\mathbf{U} \cdot \mathbf{S}_f = \left(\frac{1}{a_P}\mathbf{H}[\mathbf{U}]\right) \cdot \mathbf{S}_f - \left(\frac{1}{a_P}\nabla p\right) \cdot \mathbf{S}_f$$

6: Repeat from step 2 until convergence

7: Solve volume fraction equation

8: Update density, viscosity and electrical conductivity using volume fraction.

5.2 Numerical Simulations with Two-Phase Navier-Stokes Equations

This section examines the fluid dynamics within a lid-driven cavity, modified to include an interface between two immiscible fluids. The computational setup involves a square cavity with a moving lid, where the top boundary is assigned a constant velocity U_o, creating a shear-driven flow. This flow setup is distinct from single-phase flows due to the added complexity of the interface between the immiscible fluids. A schematic representation of this setup is shown in Figure 5.1. Computational fluid dynamics (CFD) simulations incorporate interface tracking to capture the flow behavior accurately. The objective is to understand how the interface affects the overall flow structure within the cavity. The results from the CFD simulations will be compared with the solutions presented in [20] to validate the accuracy of the observed flow patterns.

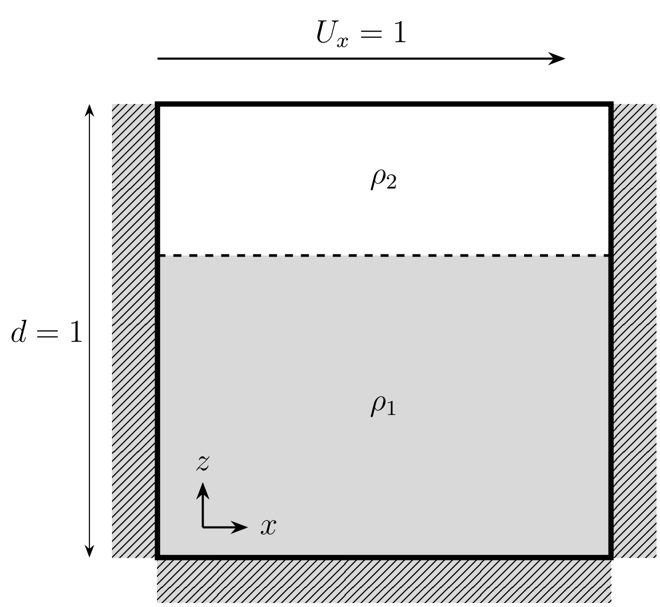

Figure 5.1: Sketch of computational domain used for numerical simulation of two-phase lid-driven cavity flow using Navier-Stokes equation. Dimensions are presented in non-dimensional form.

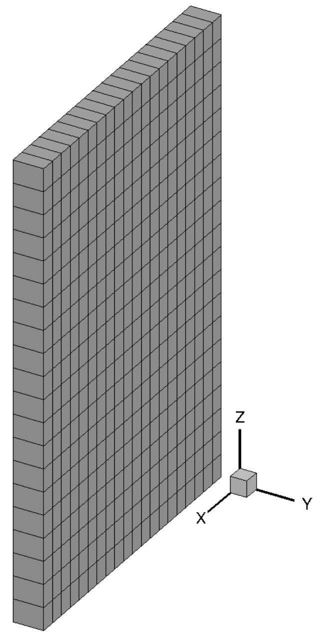

Figure 5.2: Computational mesh used for numerical simulation of two-phase lid-driven cavity flow using Navier-Stokes equation. The domain is a rectangular Cartesian grid with only one cell in the y-direction. Presented figure is a representative mesh, not the actual.

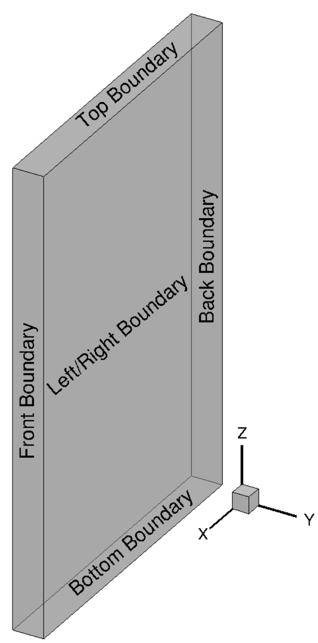

Figure 5.3: Boundary labels of the computational domain used for numerical simulation of two-phase lid-driven cavity flow using Navier-Stokes equation. Presented figure is representative and not to scale.

Table 5.1: Geometry and physical property used for numerical simulation of two-phase lid-driven cavity flow. The parameters used are non-dimensional and same as those in [20].

Parameter	Description	Value
d	Depth of square cavity	1.0
d_1	Depth of fluid 1	$0.75\,d$
d_2	Depth of fluid 2	$0.25\,d$
ρ_1	Density of the fluid 1	1.0
ρ_2	Density of the fluid 2	0.99235
μ_1	Viscosity of the fluid 1	1.0
μ_2	Viscosity of the fluid 2	0.76699
p	Pressure	1.0
ts	Total simulation time	1.0
Re	Reynolds number	12.69
Fr	Froude number	0.029

Table 5.2: Boundary conditions used for numerical simulation of two-phase lid-driven cavity flow.

	Boundary Condition	
Boundary	Velocity ($\mathbf{U}$)	Pressure (p)
Top boundary	Fixed value	Zero normal gradient
Bottom boundary	Fixed value	Zero normal gradient
Left boundary	Zero normal gradient	Zero normal gradient
Right boundary	Zero normal gradient	Zero normal gradient
Front boundary	Fixed value	Zero normal gradient
Back boundary	Fixed value	Zero normal gradient

Solution:

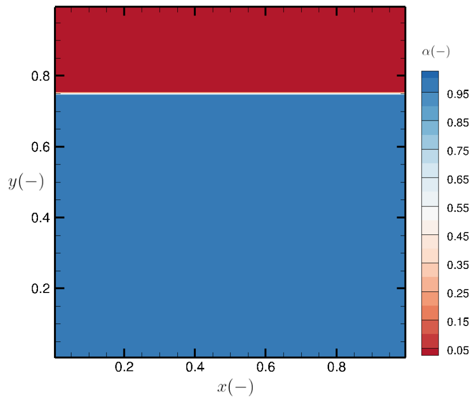

(a) t = 0.0

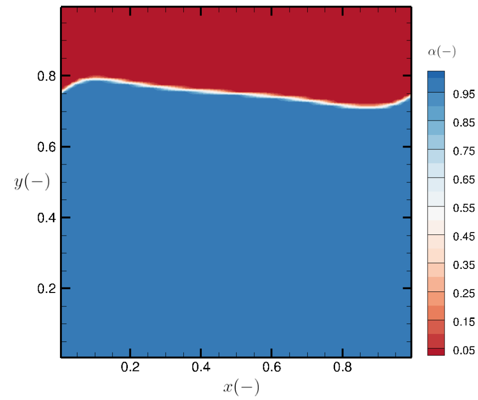

(b) t = 0.2

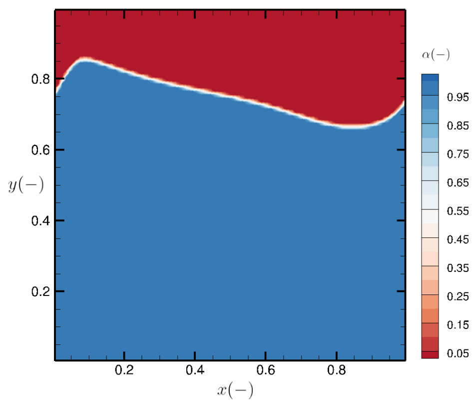

(c) t = 0.4

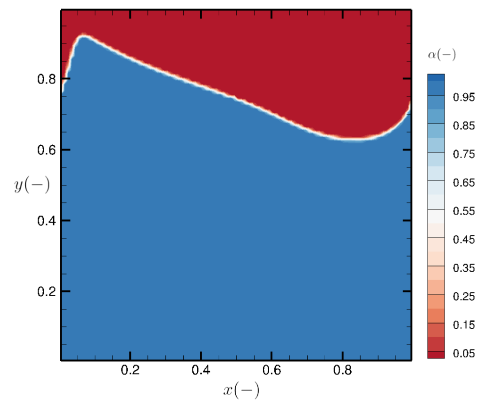

(d) t = 0.6

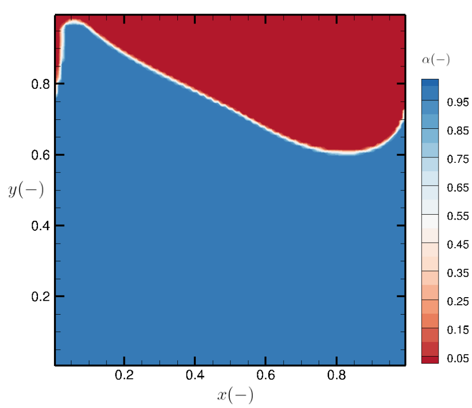

(e) t = 0.8

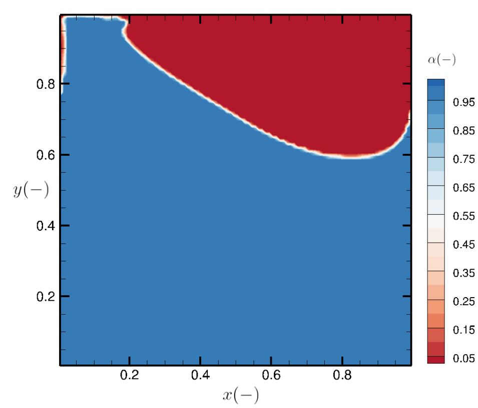

(f) t = 1.0

Figure 5.4: Simulation results of two phase lid-driven cavity flow using Navier-Stokes equation. The figures display volume fractions at non-dimensional times.

Discretization Error in Numerical Solutions:

To verify the grid independence of the current solutions, the free surface profile at a non-dimensional time of $t = 1$ is compared with the numerical simulations from Huang et al. (2019) [20] using three different mesh sizes: (i) a coarse mesh, designated as M1, with a grid resolution of $N_x \times N_z = 50 \times 50$, (ii) an intermediate mesh, known as M2, with a grid resolution of $N_x \times N_z = 75 \times 75$, and (iii) a fine mesh, termed M3, with a grid resolution of $N_x \times N_z = 100 \times 100$. Relative percentage error is calculated for interface location at right wall.

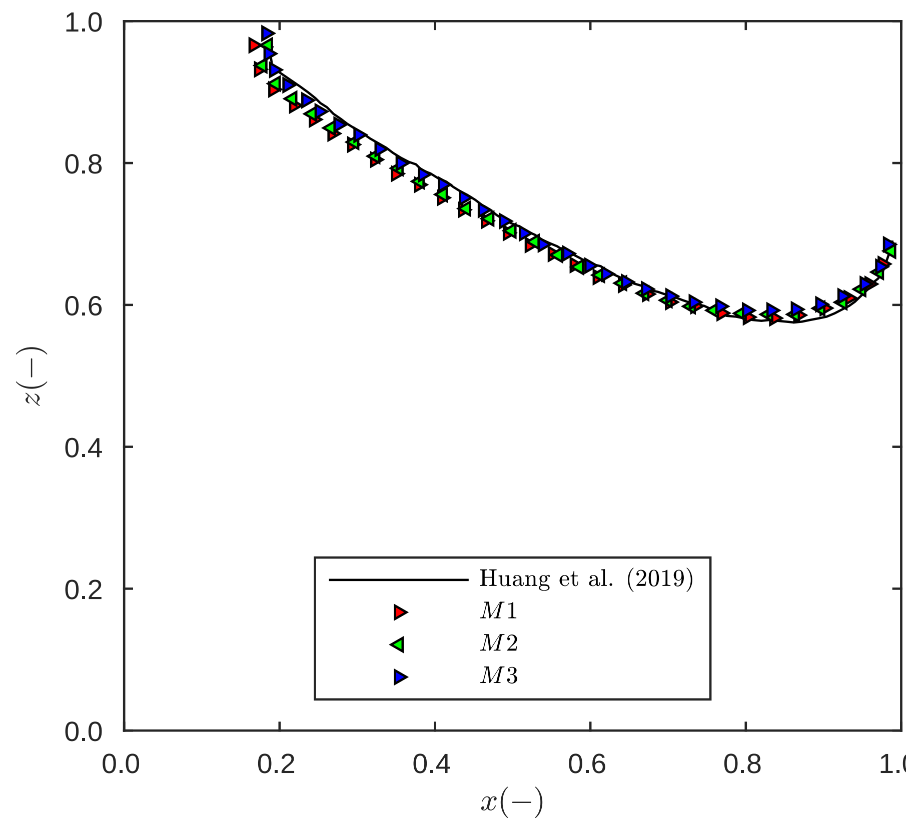

Figure 5.5: Mesh dependency on the interface profile in the simulation of two phase lid-driven cavity flow using Navier-Stokes equation.

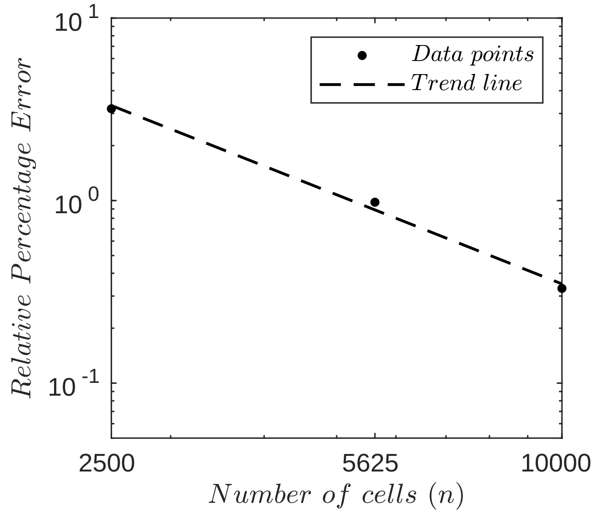

Figure 5.6: Comparison of true percent relative error across varying mesh sizes in the simulation of two-phase lid-driven cavity flow using the Navier-Stokes equations. The variable n denotes the number of cells in each mesh size. The error exhibits a linear decrease and tends toward zero as n increases.

Order of accuracy : In Figure 5.6 logarithm of the grid size against the logarithm of the corresponding error is plotted. The calculated order of accuracy for the solver, based on the fitted line shown in Figure 5.6, is 1.6228.

5.3 Numerical Simulations with Two-Phase Maxwell-Navier-Stokes Equations

5.3.1 Numerical Simulation of Axisymmetric Electrically Driven Flow in an Annular Channel with Free Surface

Building upon the single-phase flow investigation presented in the preceding chapter, this section extends the numerical simulation to consider an axisymmetric electrically driven flow within an annular channel that now includes a free surface, representing a two-phase system. The problem setup is the same as described in [43, 44], extending the single-phase scenario detailed in [26] to a two-phase scenario with a free surface. The bottom region of the channel is occupied by an electrically conducting liquid metal, and the upper region is filled with an electrically non-conducting fluid. To initiate the electric current in the liquid metal, electric potentials are applied at the inner and outer cylinders, establishing a potential difference.

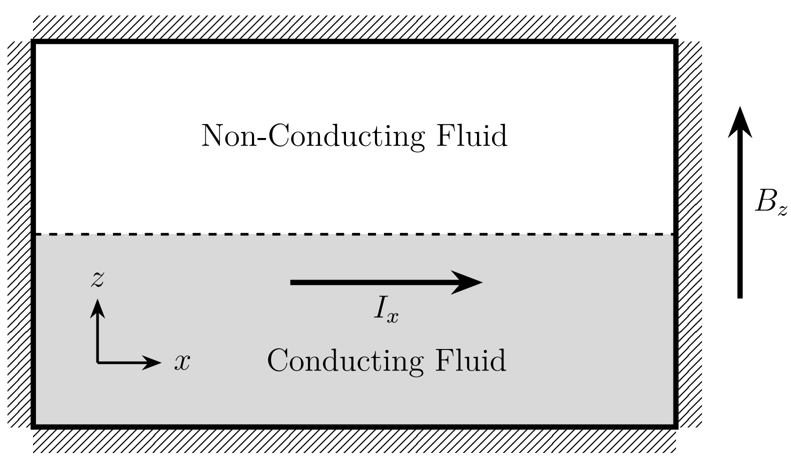

Figure 5.7: Sketch of the computational domain used for numerical simulation of axisymmetric electrically driven two-phase flow in an annular channel. The picture is a cross section of an annular cylinder. The left and right surfaces correspond to the inner and outer radii of the cylinder.

The geometric configuration of the channel is defined by a length l, inner radius r_i, and outer radius r_o. When the potentials are applied, an electric current traverses the conductive liquid metal and interacts with a uniform magnetic field $B_z = B_o$, which is aligned axially with the cylinders. This results in a rotational flow within the liquid metal due to the induced Lorentz forces. A schematic representation of this computational domain is illustrated in Figure 5.7. Additionally, the angular momentum along the z-axis, away from the side walls, is compared with the exact solutions in literature [26, 43, 44, 46] for the two-phase scenario.

Numerical simulations are conducted in geometry using the wedge formulation as before. The boundaries in these simulations are labeled in the same manner as before and is shown in the picture described in Figure 5.9. The back boundary aligns with the cylinder's inner surface, while the front boundary is associated with the outer surface. The top and bottom boundaries correspond to the cylinder's upper and lower surfaces, respectively. Lastly, the left and right boundaries pertain to the axially symmetrical surfaces of the cylinder.

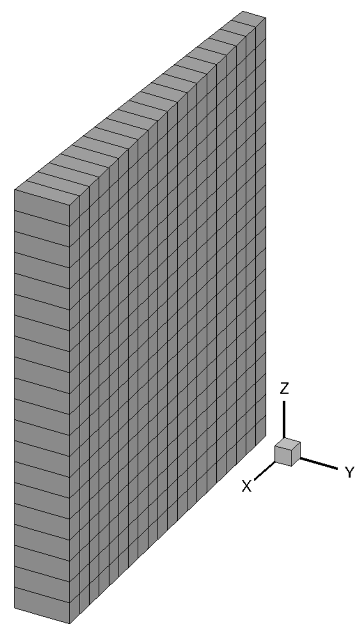

Figure 5.8: Computational mesh used for numerical simulation of axisymmetric electrically driven two-phase flow in an annular channel. Presented figure is a representative mesh, not the actual.

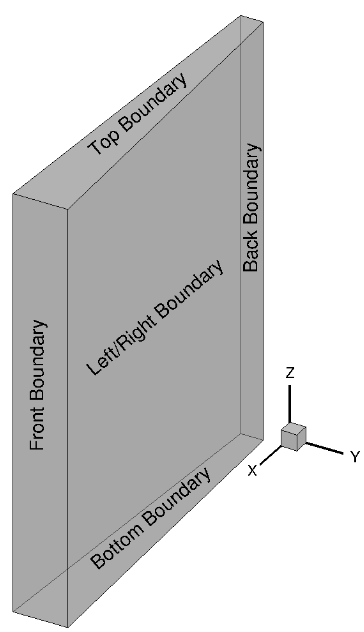

Figure 5.9: Boundary labels for the computational domain used for numerical simulation of axisymmetric electrically driven two-phase flow in an annular channel.The left boundary corresponds to the front plane, and the right boundary is located on the other side of the geometry as shown. Presented figure is representative and not to scale.

For this test case, the dimensions of the setup are based on Khalzov's dissertation [26].

Table 5.3: Geometry, physical property and boundary condition parameters used for numerical simulation of axisymmetric electrically driven two-phase flow in an annular channel. All the parameters used are non-dimensional.

Parameter	Description	Value
r_i	Inner radius of cylinder	1.0
r_o	Outer radius of cylinder	5.0
H	Height of cylinder	2.0
d	depth of conducting fluid	1.0
σ_l	Electrical conductivity of conducting fluid	1.0
σ_g	Electrical conductivity of non-conducting fluid	0.0
Φ_b	Potential at back boundary	$-\dfrac{\ln(r_i/r_o)}{2\pi H\sigma}$
Φ_f	Potential at front boundary	0.0
B_z	Imposed external magnetic Field	1.0
ρ_l	Density of conducting fluid	1.0
ρ_g	Density of non-conducting fluid	0.001
μ_l	Viscosity of conducting fluid	1.0
μ_g	Viscosity of non-conducting fluid	0.1
p	Pressure	1.0
Re	Reynolds number	1.0
Ha	Hartmann number	0.1

Table 5.4: Boundary conditions used for numerical simulation of axisymmetric electrically driven two-phase flow in an annular channel.

	Boundary Condition	
Boundary	Velocity ($\mathbf{U}$)	Pressure (p)
Top boundary	Fixed value	Zero normal gradient
Bottom boundary	Fixed value	Zero normal gradient
Left boundary	Zero normal gradient	Zero normal gradient
Right boundary	Zero normal gradient	Zero normal gradient
Front boundary	Fixed value	Zero normal gradient
Back boundary	Fixed value	Zero normal gradient

Table 5.5: Boundary conditions used for numerical simulation of axisymmetric electrically driven two-phase flow in an annular channel.

	Boundary Condition	
Boundary	Electric Scalar Potential (Φ)	Magnetic Vector Potential ($\mathbf{A}$)
Top boundary	Zero normal gradient	Fixed value
Bottom boundary	Zero normal gradient	Zero normal gradient
Left boundary	Zero normal gradient	Zero normal gradient
Right boundary	Zero normal gradient	Zero normal gradient
Front boundary	Fixed value	Zero normal gradient
Back boundary	Fixed value	Zero normal gradient

Solution:

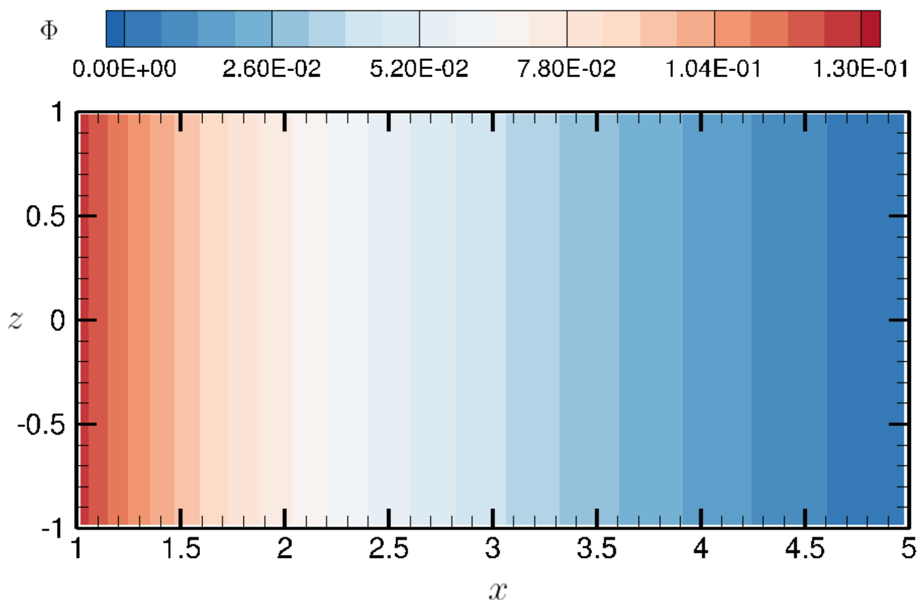

(a)

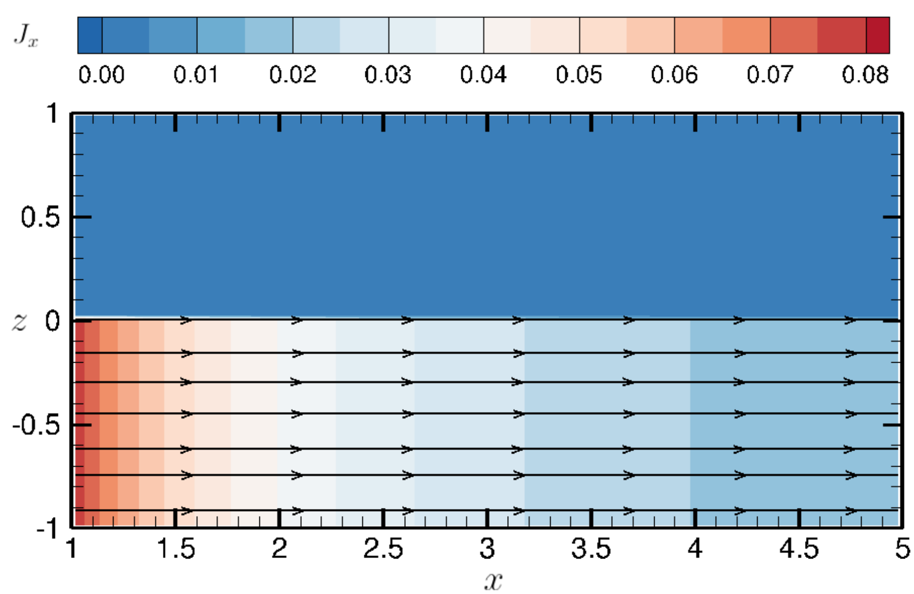

(b)

Figure 5.10: Simulation results of steady electrically driven two-phase flow in annular channel. The figures display (a) the electric potential and (b) stream lines of current density colored with x component of current density. The variables presented in the plot are non-dimensional.

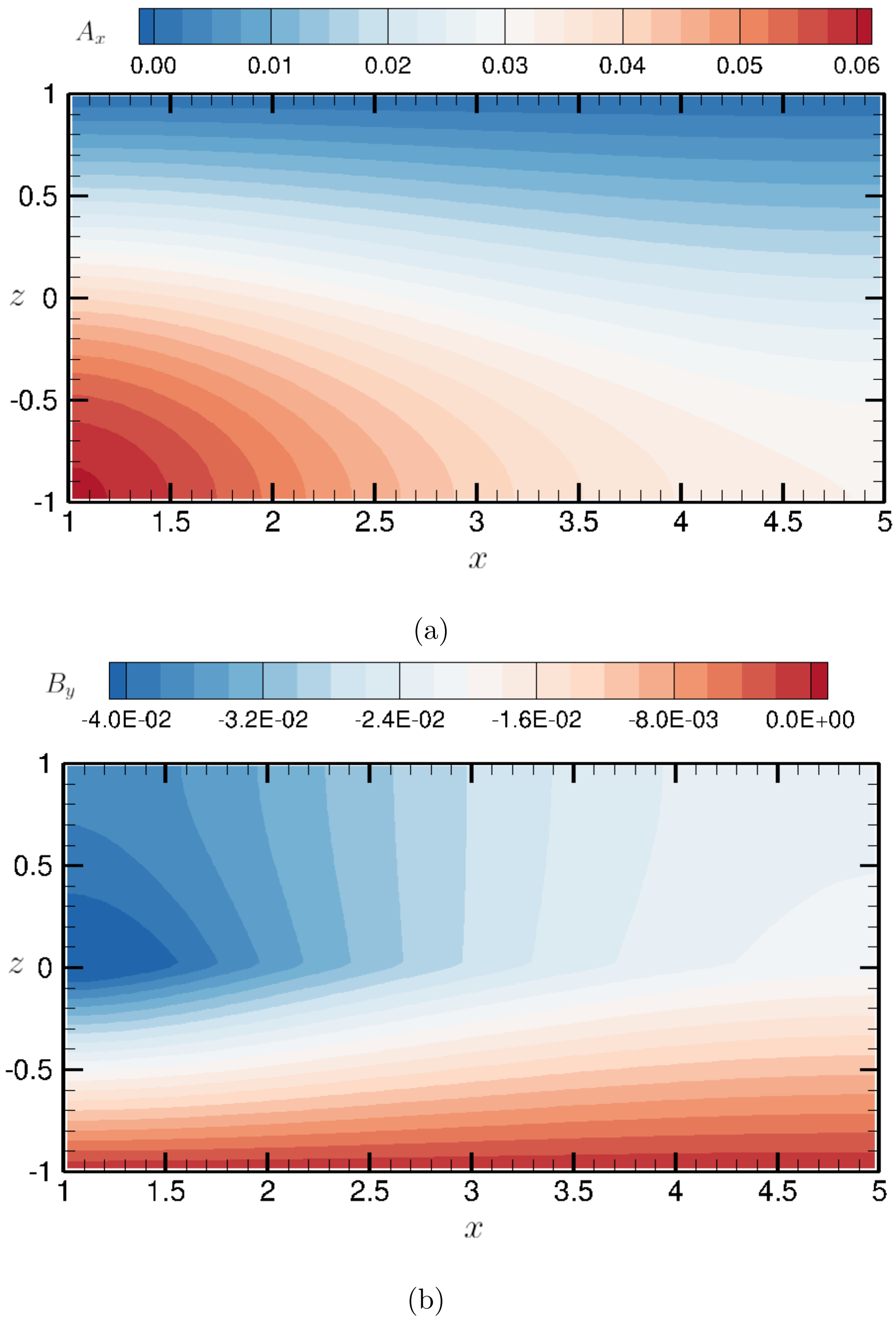

Figure 5.11: Simulation results of steady electrically driven two-phase flow in annular channel. The figures display (a) the magnetic vector potential, (b) the induced magnetic field due to applied current. The variables presented in the plot are non-dimensional.

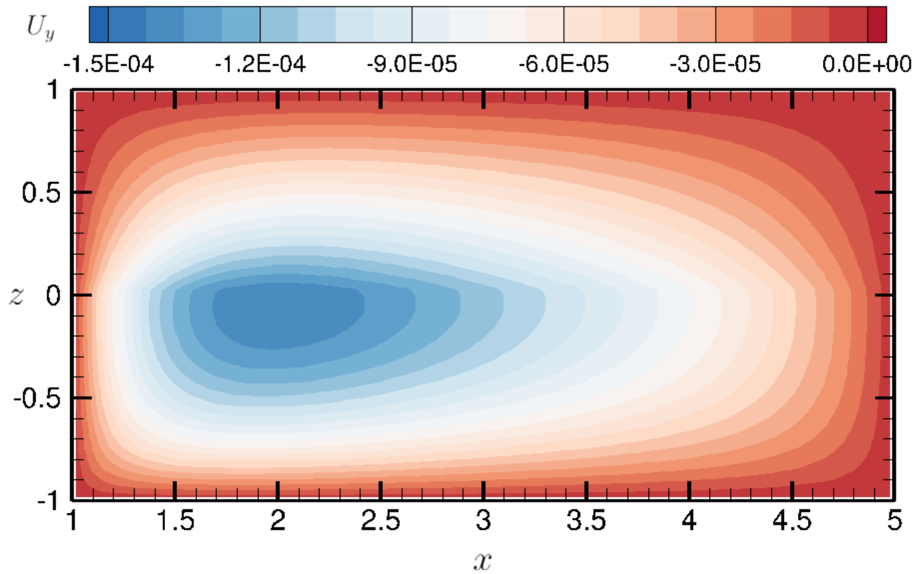

(a)

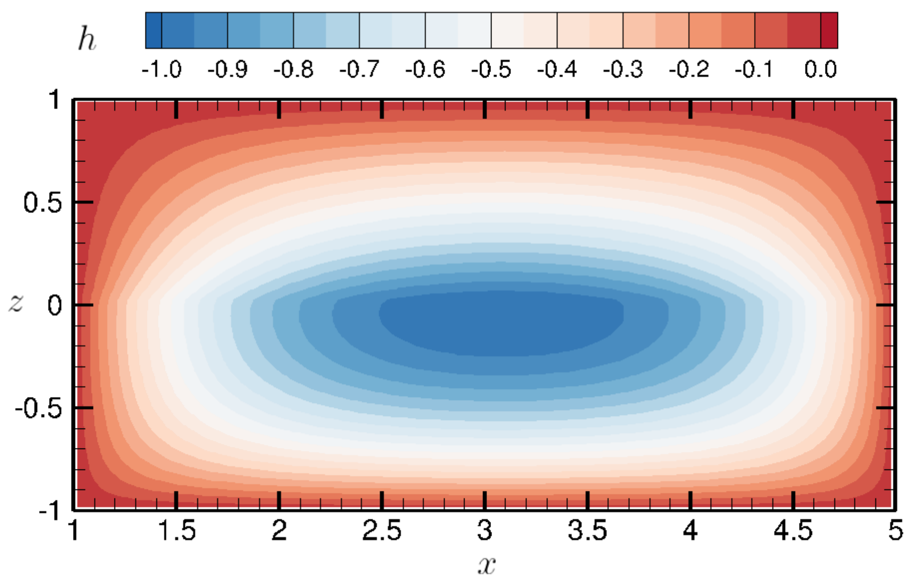

(b)

Figure 5.12: Simulation results of steady electrically driven two-phase flow in annular channel. The figures display (a) the azimuthal velocity field ($U_y = U_\theta$), (b) the angular momentum of the rotating fluid ($h = x\,U_y = r\,U_\theta$). The variables presented in the plot are non-dimensional.

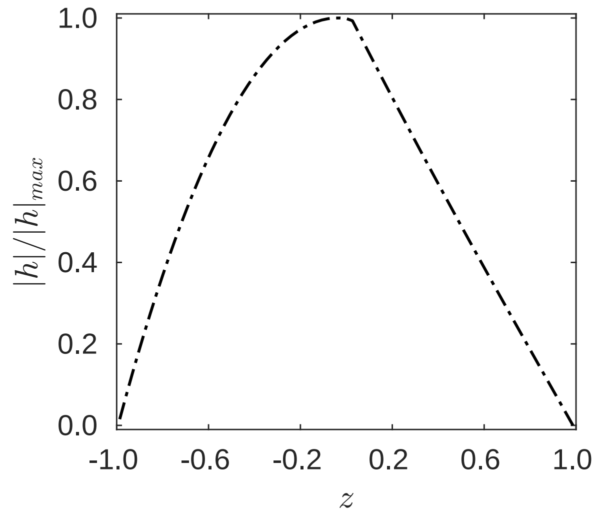

Figure 5.13: Simulation results of steady electrically driven two-phase flow in annular channel. The figure display absolute and normalized angular momentum along the vertical centerline away from side walls. The variables presented in the plot are non-dimensional.

Discretization Error in Numerical Solutions:

The grid independence of the current solutions is studied by comparing the electric potential profile, for which an analytical solution is provided in chapter 3, with numerical simulations conducted on three different mesh sizes.: (i) a coarse mesh, designated as M1, with a grid resolution of $N_x \times N_z = 5 \times 5$, (ii) an intermediate mesh, known as M2, with a grid resolution of $N_x \times N_z = 10 \times 10$, and (iii) a fine mesh, termed M3, with a grid resolution of $N_x \times N_z = 20 \times 20$.

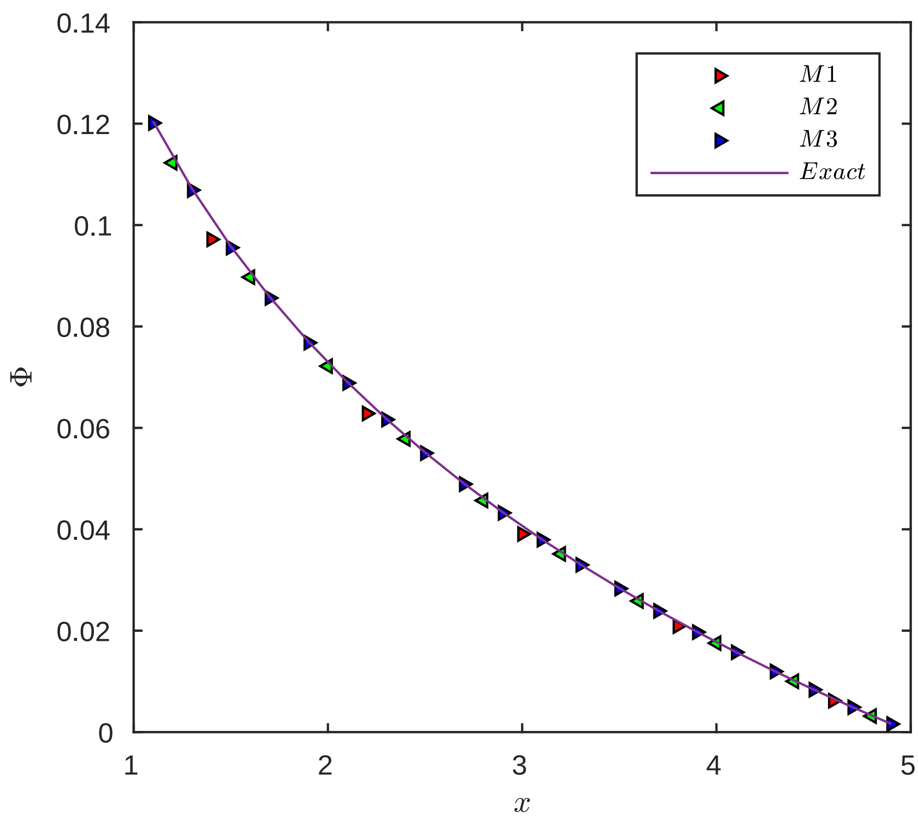

Figure 5.14: Mesh dependency on the electric potential profile in the simulation of steady electrically driven two-phase flow in annular channel. The variables in the plot are presented in non-dimensional terms.

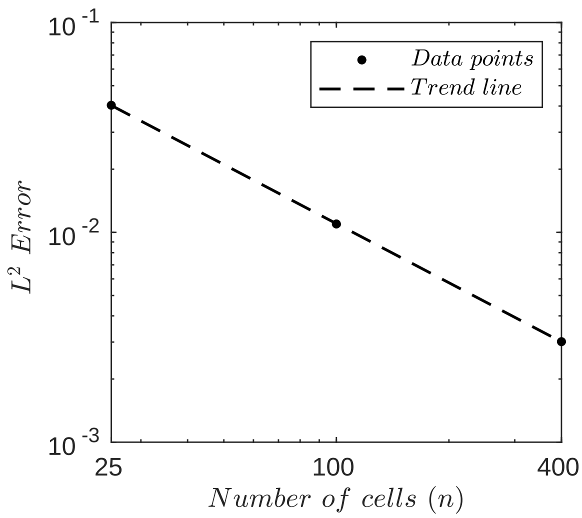

Figure 5.15: Comparison of L^2 error across varying mesh sizes in the simulation of steady electrically driven two-phase flow in annular channel. The variable n denotes the number of cells in each mesh size. The error exhibits a linear decrease and tends toward zero as n increases.

Order of accuracy : In Figure 5.15 logarithm of the grid size against the logarithm of the corresponding error is plotted. The calculated order of accuracy for the solver, based on the fitted line shown in Figure 5.15, is 0.935744.

5.3.2 Maxwell-Navier-Stokes Equations for Fusion Liquid Wall

In the case of fusion liquid walls, there is no external magnetic field present. The current from the wire flows radially inside the liquid metal, as shown in Figure 1.3. For simplicity, this model focuses exclusively on the effects of the radial current flowing through the liquid metal.

The continuity equation can be expressed as follows:

$$\nabla \cdot \mathbf{U} = 0$$

The equation governing fluid momentum can be expressed as:

$$\frac{\partial \rho \mathbf{U}}{\partial t} + \nabla \cdot (\rho \mathbf{U}\mathbf{U}) - \nabla \cdot (\mu \nabla \mathbf{U}) + \nabla p - \rho \mathbf{g} - \mathbf{J} \times \mathbf{B} = 0$$

The density of the mixture ρ is calculated as:

$$\rho = \alpha \rho_l + (1 - \alpha)\rho_g$$

Here, ρ_l is the density of liquid and ρ_g is the density of gas. Similarly, the mixture's fluid viscosity and electrical conductivity can be calculated.

$$\mu = \alpha \mu_l + (1 - \alpha)\mu_g$$
$$\sigma = \alpha \sigma_l + (1 - \alpha)\sigma_g$$

The equation governing the temporal evolution of the liquid volume fraction is [8, 31, 50] :

$$\frac{\partial \alpha}{\partial t} + \nabla \cdot (\alpha \mathbf{U}) = 0$$

The steady Maxwell equations remain unchanged and are presented again here for completeness. For the applied electrical current, the governing equation is:

$$\nabla \cdot \sigma \nabla \Phi - \nabla \cdot (\sigma \mathbf{U} \times \mathbf{B}) = 0$$

Subsequently, the current density $\mathbf{J}$ is calculated as:

$$\mathbf{J} = -\sigma \nabla \Phi + \sigma \mathbf{U} \times \mathbf{B}$$

The governing equation for magnetic vector potential is:

$$\nabla \cdot \nabla \mathbf{A} - \mu_0 \sigma \nabla \Phi + \mu_0 \sigma \mathbf{U} \times \mathbf{B} = 0$$

Using the definition of magnetic vector potential, the magnetic field can be calculated as $\mathbf{B} = \nabla \times \mathbf{A}$.

Non-dimensional form : The governing equations are presented in non-dimensional form as follows :

$$\nabla \cdot \sigma \nabla \Phi - Re_m \, \nabla \cdot (\sigma \mathbf{U} \times \mathbf{B}) = 0$$

$$\nabla \cdot \nabla \mathbf{A} - \sigma \nabla \Phi + Re_m \, \sigma \, (\mathbf{U} \times \mathbf{B}) = 0$$

$$\nabla \cdot \mathbf{U} = 0$$

$$\frac{\partial \rho \mathbf{U}}{\partial t} + \nabla \cdot (\rho \mathbf{U}\mathbf{U}) - \frac{1}{Re} \nabla \cdot (\nabla \mathbf{U}) + \nabla p - \frac{1}{Fr^2} \rho \mathbf{g} - \frac{Ha^2}{Re \, Re_m} \mathbf{J} \times \mathbf{B} = 0$$

5.3.3 Numerical Simulation of Free Surface Deformation in Liquid Metal

This section presents the numerical simulation of radial current flow in liquid metal. Current is injected into the liquid metal by applying potential difference between the inner and outer cylindrical surfaces. The setup for this computational model is similar to those used in previous two-phase Maxwell-Navier-Stokes simulations. It consists of a lower section filled with electrically conductive liquid metal and an upper section with an electrically non-conductive fluid.

The shape of the container is described by its height H, inner radius r_i, and outer radius r_o. When electric potentials are applied, an electric current flows through the conductive liquid metal as illustrated in Figure 5.16. The radial current creates a magnetic field that decays in both the radial and axial directions. This spatially varying magnetic field generates a Lorentz force, causing the interface between the two fluids to deform.

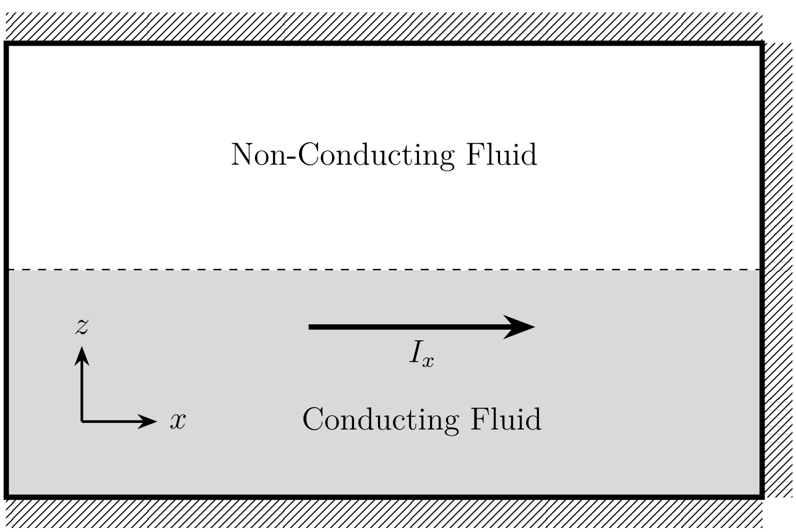

Figure 5.16: Sketch of the computational domain used for the numerical simulation of fusion liquid wall model. The picture is a cross section of an annular cylinder. The left and right surfaces correspond to the inner and outer radii of the cylinder.

Numerical simulations are conducted in geometry using the wedge formulation. The boundaries in these simulations are labeled as shown in Figure 5.18. The back boundary aligns with the cylinder's inner surface, while the front boundary aligns with the outer surface. The top and bottom boundaries correspond to the cylinder's upper and lower surfaces, respectively. Lastly, the left and right boundaries pertain to the axially symmetrical surfaces of the cylinder. The expression for the current density associated with radial current has been previously derived and is given by the following equation:

$$J(r) = -\frac{\sigma V_o}{r \ln(r_i/r_o)}$$

The total current passing through the liquid metal is represented by $I = J(r) \times A(r)$. Here, $A(r)$ denotes the cross-sectional area of the cylinder at a given radius within the liquid metal container. For a liquid metal with a depth of d, the total current can be calculated using the expression for current density.

$$I = -\left(\frac{\sigma V_o}{r \ln\left(\frac{r_i}{r_o}\right)}\right) * (2\pi r d)$$

Given the total current I, the expression for V_o is derived from the above equation. The term r cancels out, resulting in the following simplified expression: $V_o = -\dfrac{I}{2\pi\sigma d} \ln\left(\dfrac{r_i}{r_o}\right)$

For instance, when the current I is set to 1A, the calculated voltage V_o is 1.0×10^{-5} V. The simulation results, obtained by solving the governing equations in non-dimensional form under the low magnetic Reynolds number approximation, correspond to $Re = 1$ and $Fr = 100$.

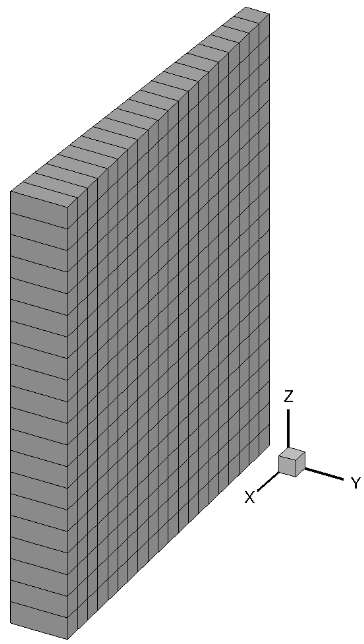

Figure 5.17: Computational mesh used for the numerical simulation of fusion liquid wall model. Presented figure is a representative mesh, not the actual.

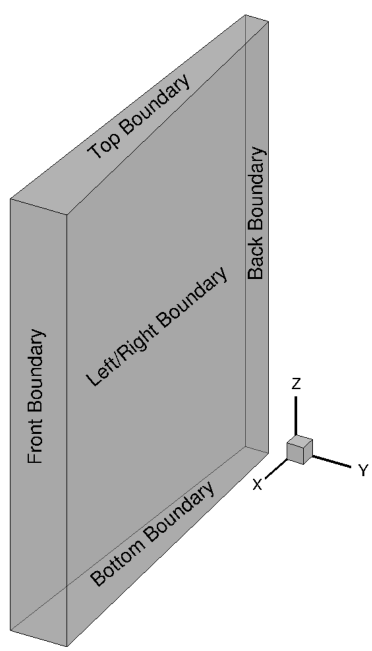

Figure 5.18: Boundary labels for the computational domain used for the numerical simulation of fusion liquid wall model.The left boundary corresponds to the front plane, and the right boundary is located on the other side of the geometry as shown. Presented figure is representative and not to scale.

Table 5.6: Parameters used for numerical simulation of fusion liquid wall model.

Parameter	Description	Value
r_i	Inner radius of cylinder	$2.35\,mm$
r_o	Outer radius of cylinder	$94\,mm$
L	Height of cylinder	$94\,mm$
d	Depth of liquid metal	$47\,mm$
σ_l	Electrical conductivity of liquid metal	$1.3 \times 10^6\,S/m$
μ_o	Magnetic permeability	$4\pi \times 10^{-7}\,H/m$
$\mathbf{A}_t$	Vector potential at top boundary	$0.0\,T\,m$
ρ_g	Density of air	$1.0\ kg/m^3$
ρ_l	Density of liquid metal	$8767\ kg/m^3$
p	Pressure	$1.0\ Pa$

Table 5.7: Boundary conditions used for numerical simulation of fusion liquid wall model.

	Boundary Condition	
Boundary	Velocity ($\mathbf{U}$)	Pressure (p)
Top boundary	Fixed value	Zero normal gradient
Bottom boundary	Fixed value	Zero normal gradient
Left boundary	Zero normal gradient	Zero normal gradient
Right boundary	Zero normal gradient	Zero normal gradient
Front boundary	Fixed value	Zero normal gradient
Back boundary	Fixed value	Zero normal gradient

Table 5.8: Boundary conditions used for numerical simulation of fusion liquid wall model.

	Boundary Condition	
Boundary	Electric Scalar Potential (Φ)	Magnetic Vector Potential ($\mathbf{A}$)
Top boundary	Zero normal gradient	Fixed value
Bottom boundary	Zero normal gradient	Zero normal gradient
Left boundary	Zero normal gradient	Zero normal gradient
Right boundary	Zero normal gradient	Zero normal gradient
Front boundary	Fixed value	Zero normal gradient
Back boundary	Fixed value	Zero normal gradient

Reynolds number :

In this specific problem, there are no boundary conditions that prescribe velocity; instead, the fluid motion is entirely driven by the Lorentz force. The Lorentz force is balanced by inertial forces as follows:

$$\nabla \cdot (\rho \mathbf{U}\mathbf{U}) = \mathbf{J} \times \mathbf{B}$$

Applying the scale factors for each variable and using Ampere's results in:

$$\left(\frac{1}{L_o}\right) \rho_o U_o^2 = J_o B_o = J_o(\mu_o L_o J_o)$$

Rearranging,

$$U_o^2 = J_o^2 L_o^2 \frac{\mu_o}{\rho_o}$$

$$U_o = J_o L_o \sqrt{\frac{\mu_o}{\rho_o}}$$

The current density scale can be expressed in-terms of current I_o and characteristic area A

$$U_o = \frac{I_o L_o}{A}\sqrt{\frac{\mu_o}{\rho_o}}$$

The characteristic area A is taken as $A = 2\pi r_o L_o$. Here r_o is outer radius of cylinder. The Reynolds number can then be calculated based on this velocity scale:

$$Re = \frac{U_o\,\rho_o\,L_o}{\mu_{vo}} = \frac{I_o\,L_o^2}{A\,\mu_{vo}}\sqrt{\mu_o\,\rho_o}$$

This Reynolds number definition is convenient as it correlates directly with the applied current. Here μ_{vo} is the viscosity scale factor for μ_v. Using these scale factors, the non-dimensional group N becomes 1, since magnetic field is generated by applied current itself and there are no external magnetic fields.

$$N = \frac{Ha^2}{Re\,Re_m} = 1$$

Solution:

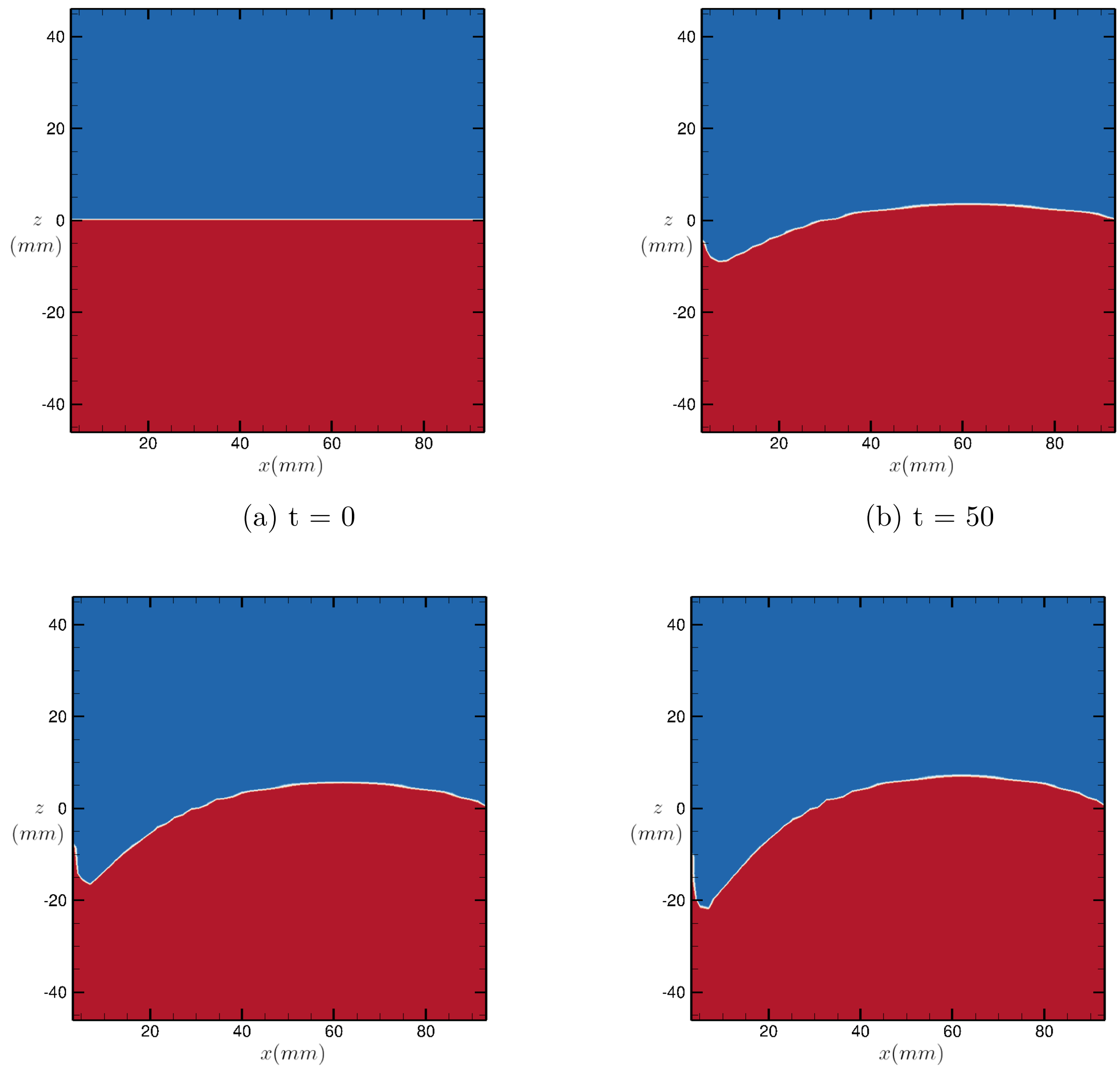

(a) t = 0

(b) t = 50

(c) t = 100

(d) t = 150

Figure 5.19: Simulation results of free surface deformation in liquid metal. The results are presented at non-dimensional time for clarity. The figures display evolution of free surface at different times. The red color corresponds to electrically conducting liquid metal corresponds to volume fraction ($\alpha = 1$) and blue corresponds to electrically non-conducting fluid air corresponds to volume fraction ($\alpha = 0$). The initial horizontal free surface at time $t = 0$, deforms due to applied electric current

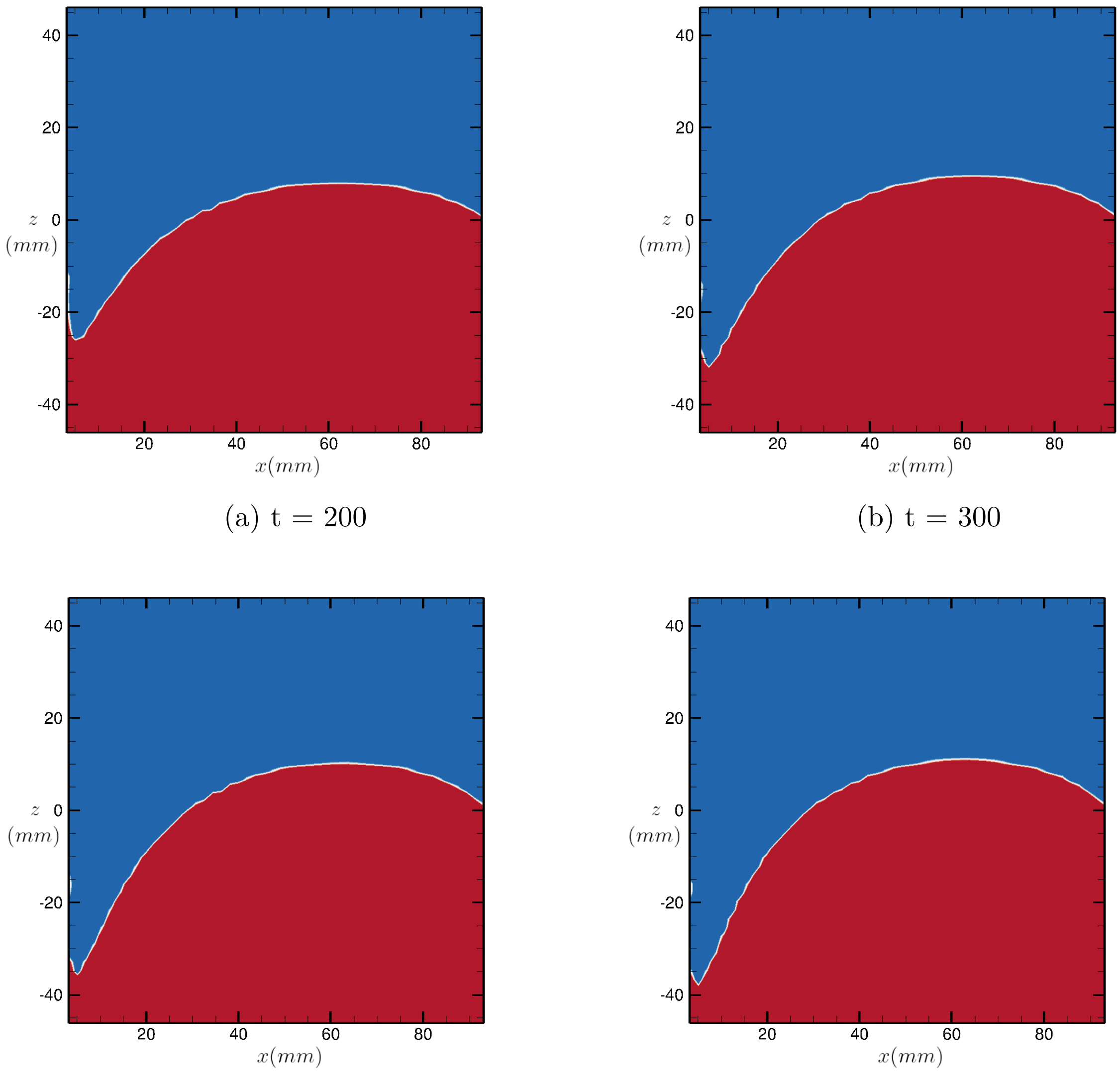

(a) t = 200

(b) t = 300

(c) t = 400

(d) t = 500

Figure 5.20: Simulation results of free surface deformation in liquid metal. The results are presented at non-dimensional time for clarity. The figures display evolution of free surface at different times. The red color corresponds to electrically conducting liquid metal corresponds to volume fraction ($\alpha = 1$) and blue corresponds to electrically non-conducting fluid air corresponds to volume fraction ($\alpha = 0$). The initial horizontal free surface at time $t = 0$, deforms due to applied electric current

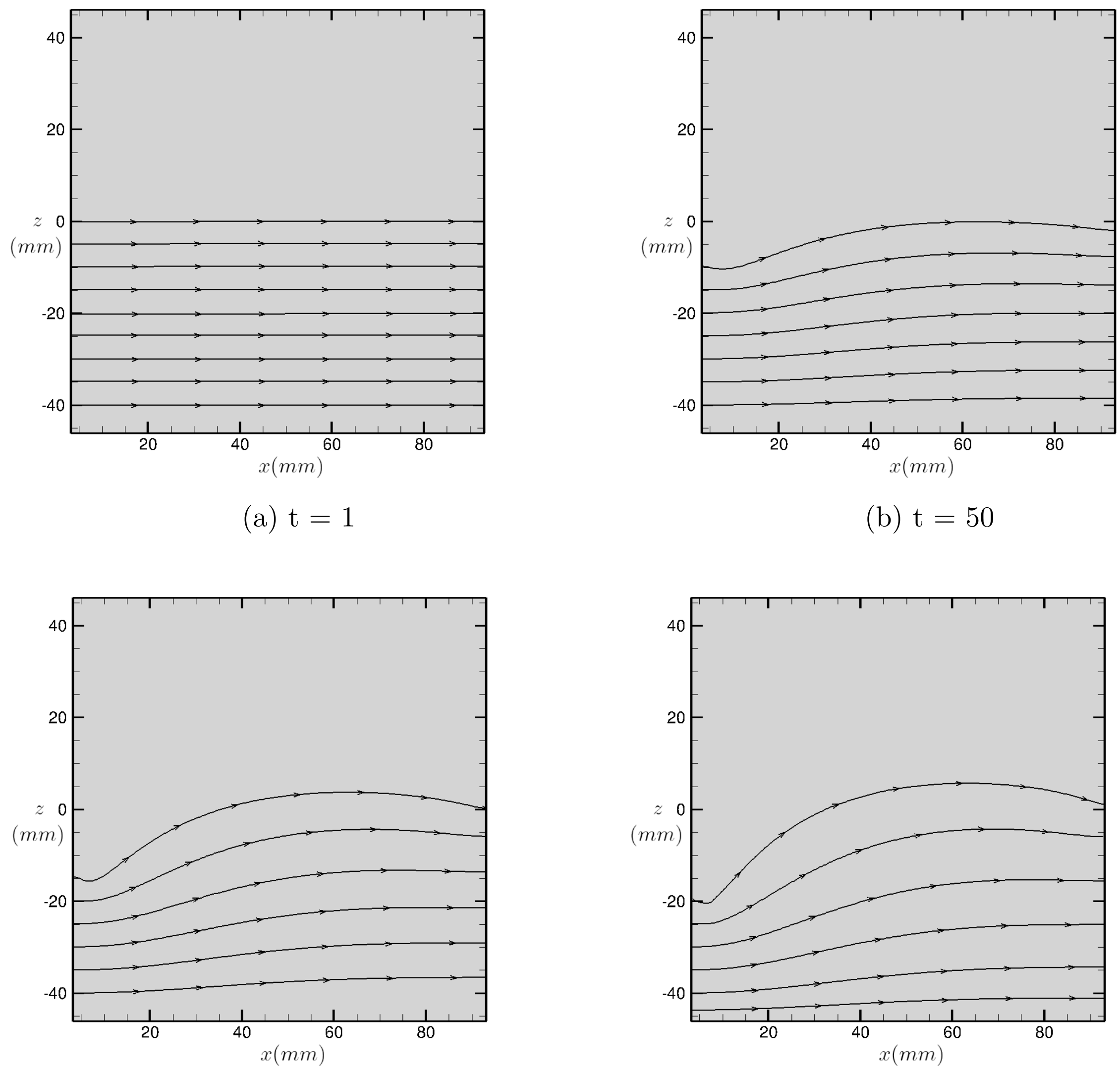

(a) t = 1

(b) t = 50

(c) t = 100

(d) t = 150

Figure 5.21: Simulation results of free surface deformation in liquid metal. The results are presented at non-dimensional time for clarity. The figures display evolution of current density streamlines at different times.

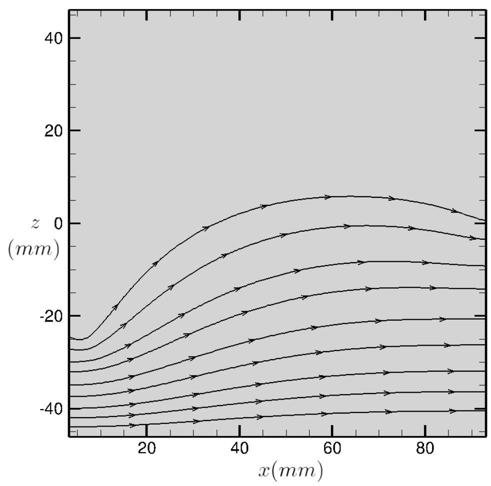

(a) t = 200

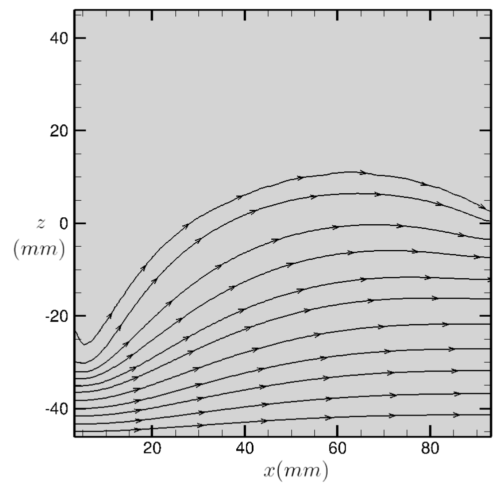

(b) t = 300

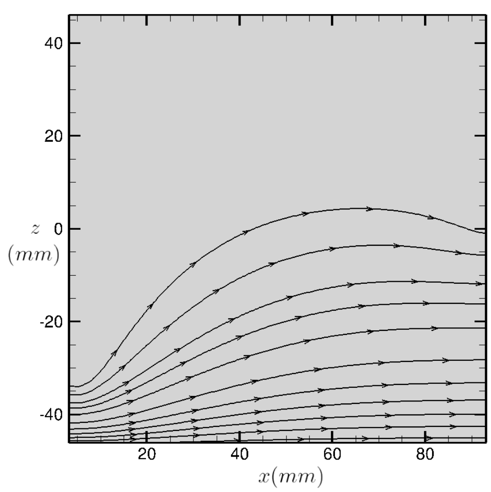

(c) t = 400

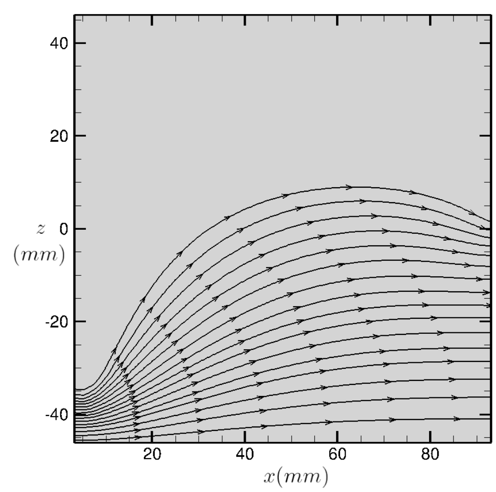

(d) t = 500

Figure 5.22: Simulation results of free surface deformation in liquid metal. The results are presented at non-dimensional time for clarity. The figures display evolution of current density streamlines at different times.

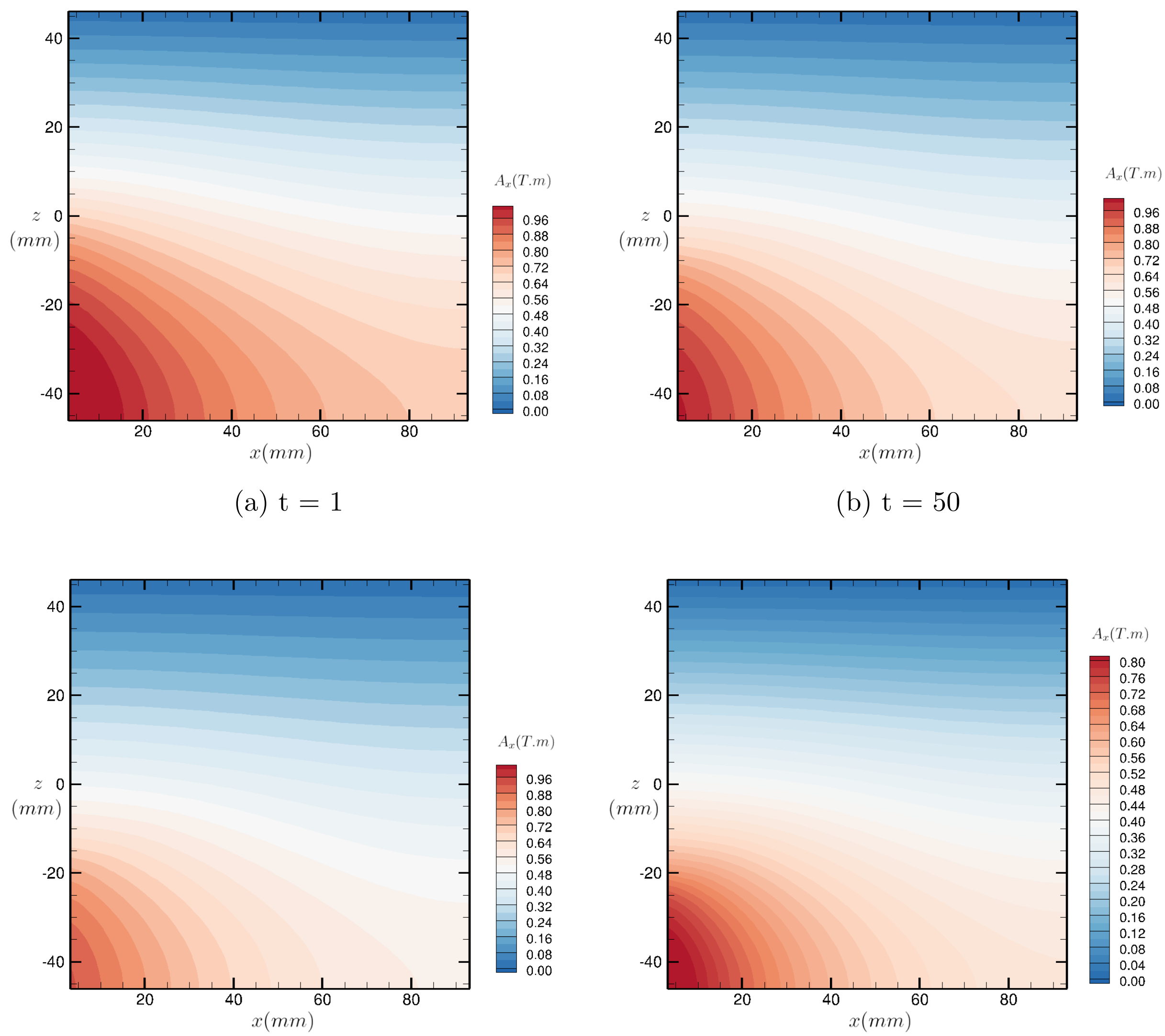

(a) t = 1 (b) t = 50

(c) t = 100 (d) t = 150

Figure 5.23: Simulation results of free surface deformation in liquid metal. The results are presented at non-dimensional time for clarity. The figures display evolution of magnetic vector potential at different times.

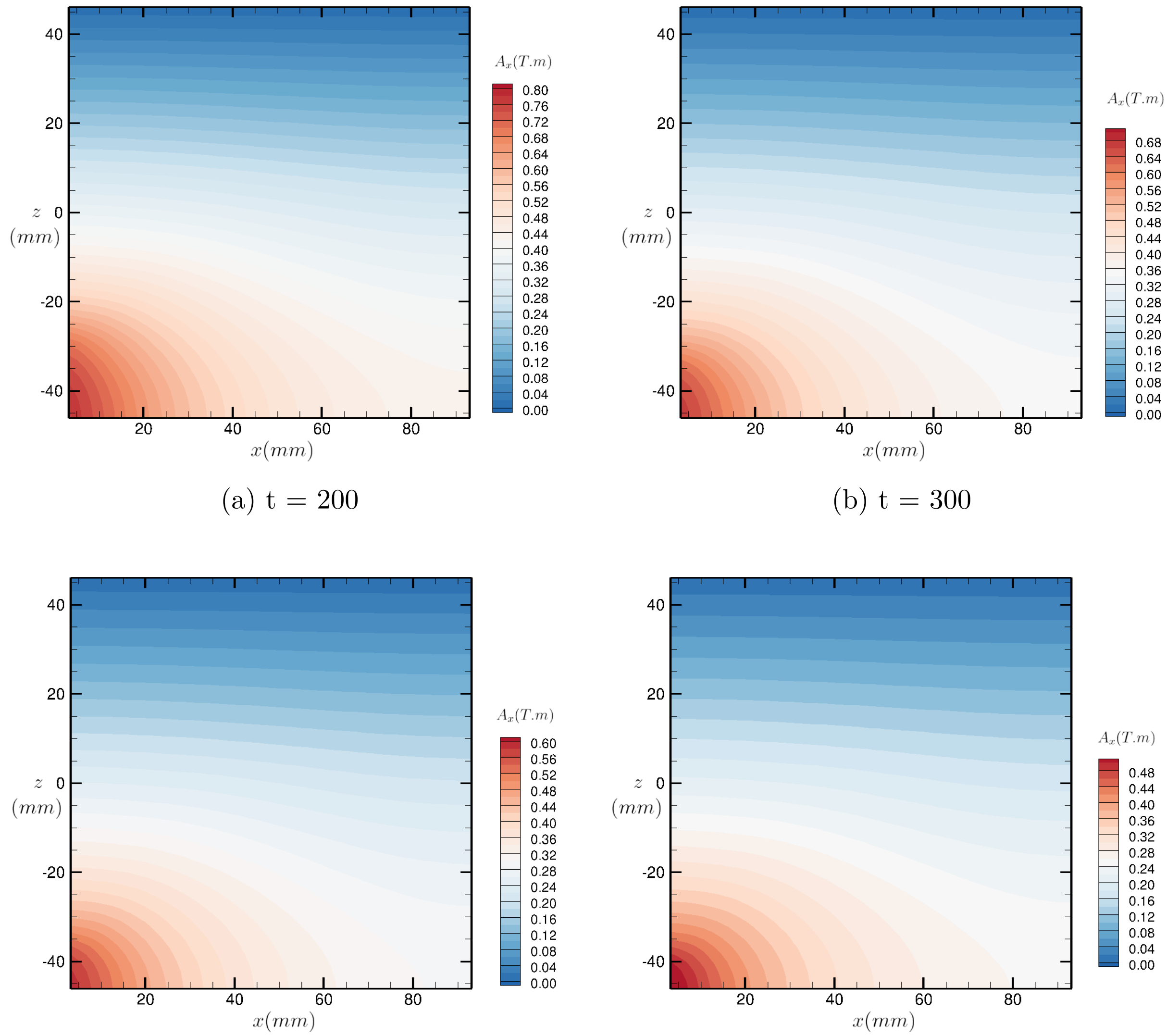

(a) t = 200

(b) t = 300

(c) t = 400

(d) t = 500

Figure 5.24: Simulation results of free surface deformation in liquid metal. The results are presented at non-dimensional time for clarity. The figures display evolution of magnetic vector potential at different times.

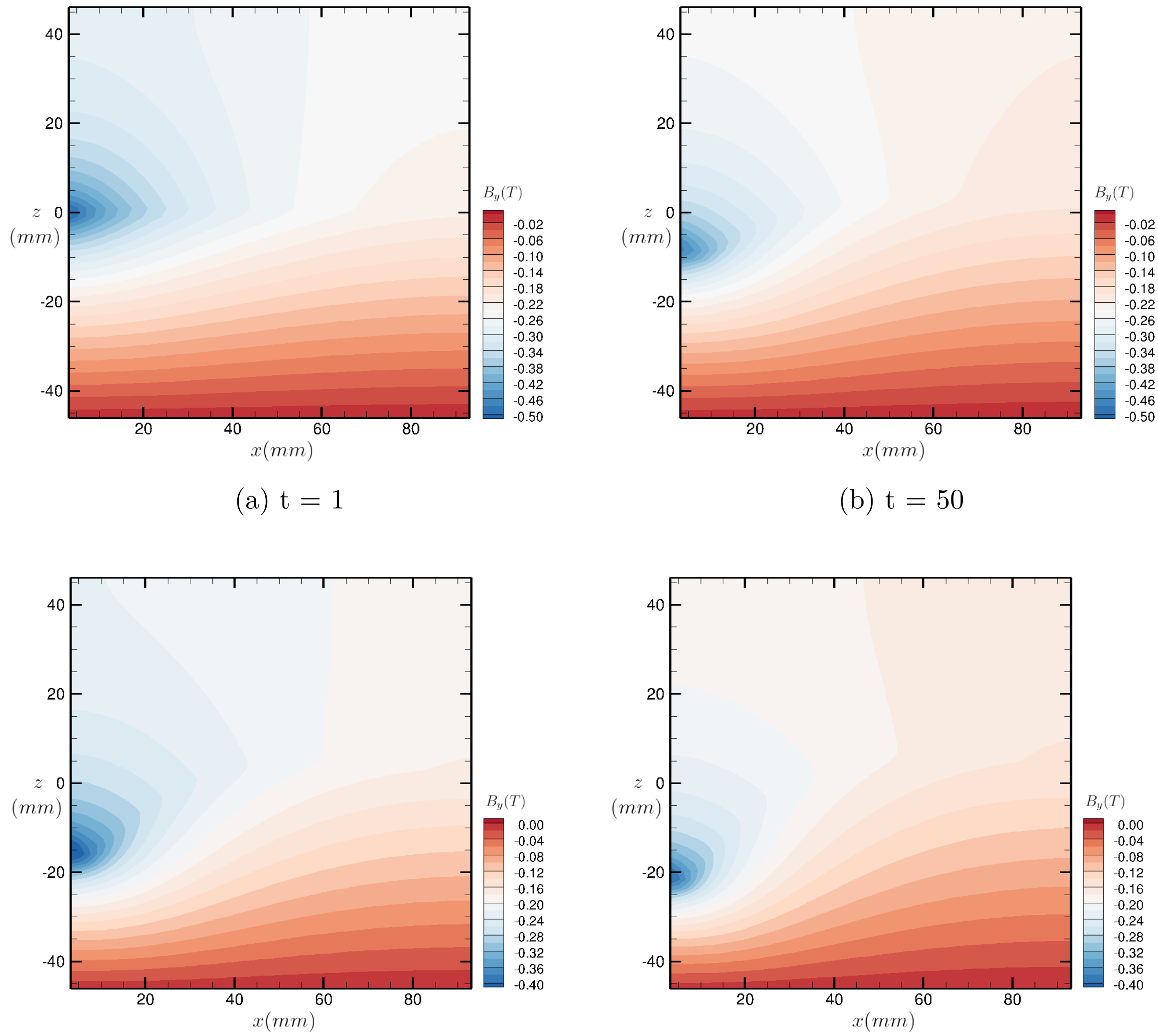

(a) t = 1

(b) t = 50

(c) t = 100

(d) t = 150

Figure 5.25: Simulation results of free surface deformation in liquid metal. The results are presented at non-dimensional time for clarity. The figures display evolution of y component of magnetic field at different times.

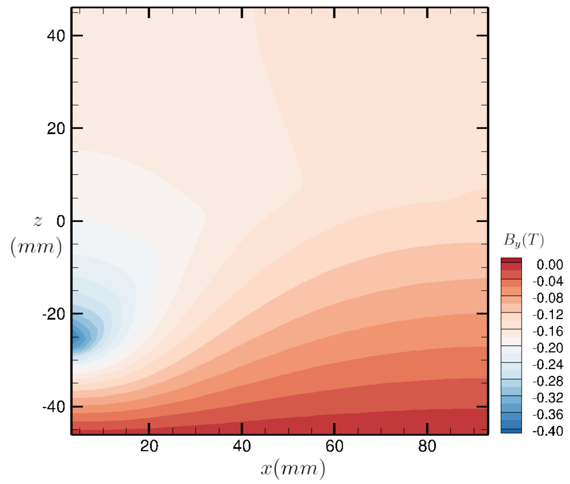

(a) t = 200

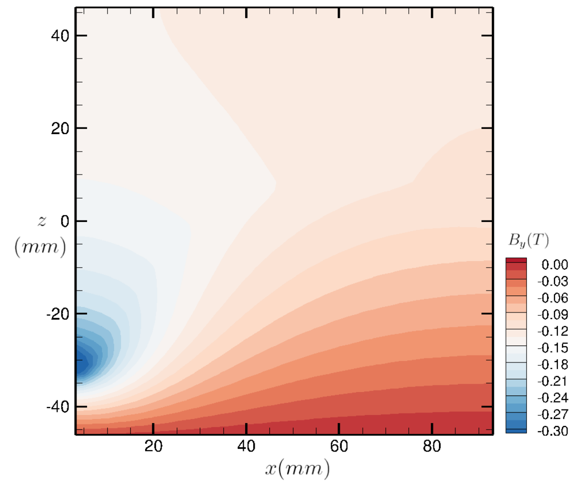

(b) t = 300

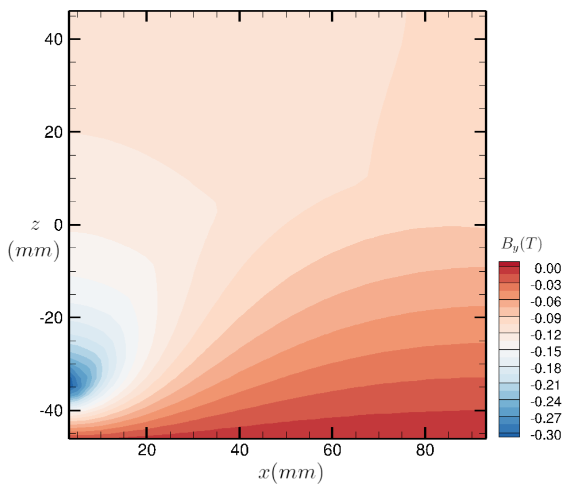

(c) t = 400

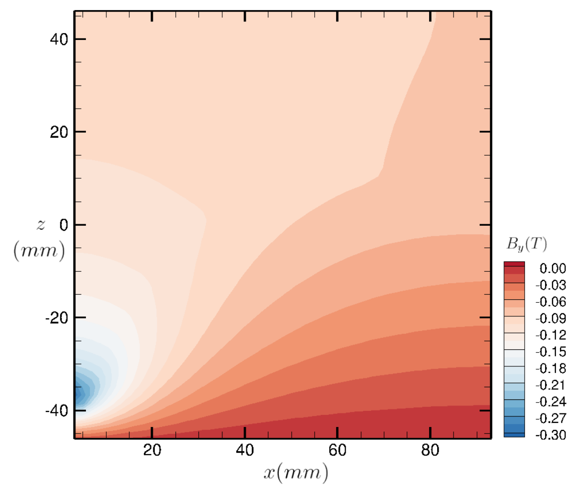

(d) t = 500

Figure 5.26: Simulation results of free surface deformation in liquid metal. The results are presented at non-dimensional time for clarity. The figures display evolution of y component of magnetic field at different times.

Mechanism of Free surface deformation

The simulation results of radial current flow in liquid metal are presented in Figure 5.19 through Figure 5.26. This study examines radial current flow within a cylindrical container partially filled with liquid metal, modeling scenarios relevant to fusion liquid wall configurations.

The mechanism driving the deformation of the free surface can be described as follows:

1. An electric potential difference is applied across the cylinder's inner and outer cylindrical surfaces. Current ($\mathbf{J}$) flows radially within the liquid metal due to applied potential difference as shown in Figure 5.21 and Figure 5.22.

2. Radial current flowing through the liquid metal generates azimuthal magnetic field ($\mathbf{B}$) in accordance with Ampere's law. The magnetic vector potential due to radial current is presented in Figure 5.23 and Figure 5.24. The magnetic field due to radial current is presented in Figure 5.25 and Figure 5.26.

3. The radial current, in conjunction with the azimuthal magnetic field, produces a Lorentz force $\mathbf{J} \times \mathbf{B}$, whose direction is downward as determined by the cross product $\mathbf{J} \times \mathbf{B}$.

4. The cross-sectional area through which current flows increases radially, given by $2\pi rd$. Here, r represents the radial distance, and d denotes the depth of the liquid metal. As the radial distance r increases, the cross-sectional area also increases. Consequently, the current density must decay in the radial direction to satisfy the continuity equation $\nabla \cdot \mathbf{J} = 0$.

5. As the current density decreases radially, the magnetic field also decreases radially. Additionally, the magnetic field also decreases axially as the enclosed current decreases

in the axial direction [11, 16, 24], starting from the free surface . The enclosed current can be conceptualized as the number of current density lines crossing a hollow cylindrical surface at a specific radial distance with different heights. A cylinder with its base coinciding with the bottom surface of the container will have fewer current lines crossing it if its height is much smaller than the depth of the liquid metal. Conversely, if the height of the cylinder approaches the depth of the metal, and its top surface coincides with the free surface, the number of enclosed current density lines is maximum. Consequently, in the axial direction, the magnetic field is stronger near the free surface, whereas in the radial direction, it is stronger near the inner cylindrical surface. Thus, a strong magnetic field is observed at the intersection of the interface with the inner cylindrical surface. This two dimensional magnetic field can be visualized in Figure 5.25 and Figure 5.26.

6. Since both the current density and magnetic field decay in the radial direction, the resulting net downward Lorentz force $\mathbf{J} \times \mathbf{B}$ is stronger near the inner cylindrical surfaces and decays radially. Consequently, the liquid metal is pushed downward near the inner cylindrical surface with a magnitude stronger than at other radial positions. Consequently, fluid pressure builds up in response to this body force, leading to deformation of the liquid metal's free surface as shown in Figure 5.19 and Figure 5.20.

7. As the liquid metal deforms, the current density lines and resulting magnetic field adjust to the shape of the liquid metal. The simulation is stopped before the liquid metal loses contact with the inner cylindrical surface.

Grid Independence Study

To verify the grid independence of the current solutions, the free surface profile at non-dimensional time $t = 200$ is compared using three different mesh sizes: (i) a coarse mesh, designated as M1, with a grid resolution of $N_x \times N_z = 50 \times 50$, (ii) an intermediate mesh, known as M2, with a grid resolution of $N_x \times N_z = 75 \times 75$, and (iii) a fine mesh, termed M3, with a grid resolution of $N_x \times N_z = 100 \times 100$. Between the M2 and M3 mesh sizes, minimal variation in the free surface profile is observed.

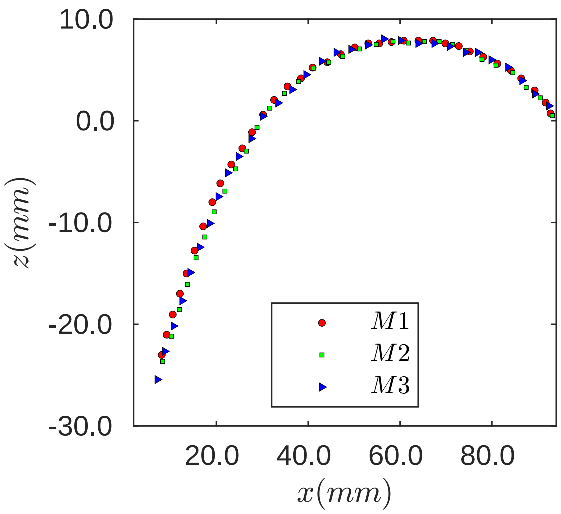

Figure 5.27: Mesh dependency on the interface profile in the simulation of free surface deformation in liquid metal using Maxwell-Navier-Stokes equation.

Effect of Applied total current

This study explores the possibility that an increase in total current could deepen the central void and elevate the overall free surface. Simulations were executed with varying levels of total current, categorized as $I_1 < I_2 < I_3$. The analysis focused on comparing the free surface profile at non-dimensional time, $t = 200$ under these different current conditions. The results indicate that an increase in current magnitude correlates with a overall free surface elevation.

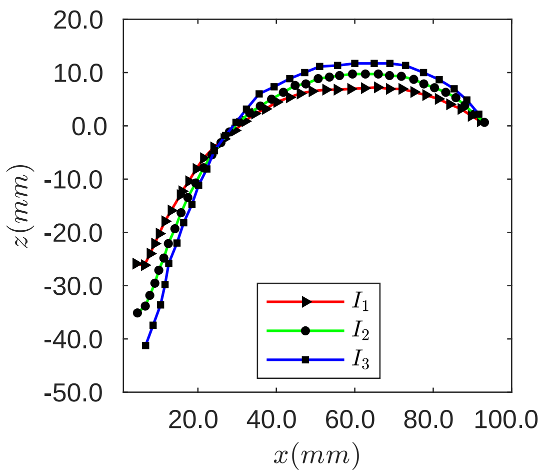

Figure 5.28: Interface profile for three different currents ($I_1 < I_2 < I_3$) in the simulation of free surface deformation in liquid metal using Maxwell-Navier-Stokes equation.

Chapter 6

Summary and Future Work

An attempt has been made to numerically simulate the free surface deformation of a fusion liquid wall, caused by the injected current from Z-pinch plasma. The approach is not only applicable to fusion wall scenarios but broadly to situations involving current injection into any conducting liquid. The dissertation employs Maxwell's equation to solve for electromagnetic fields as opposed to magnetic induction equation in traditional magneto-hydrodynamic (MHD) formulation. The latter is more suitable when an external magnetic field is present and finds limitations in cases where the magnetic field results from current injected into a conducting fluid. In other words, MHD formulation is more suitable to situation when initial magnetic field is known. Solving Maxwell equations on the other hand will be most suitable when you directly inject current into conducting liquid. The development of the final solver involved a systematic approach, beginning with solving Maxwell's equations, then integrating them into the single-phase Maxwell-Navier-Stokes framework, and finally extending to the two-phase Maxwell-Navier-Stokes equations. The summary of the work conducted in this dissertation is provided here.

Potential Formulation of Maxwell Equations : The incompressible Navier-Stokes equations are discretized within a finite volume framework. Employing a collocated grid arrangement for these equations, where both pressure and velocity are stored at the same grid locations, can lead to checkerboard oscillations in the numerical solution.

This issue typically arises due to poor pressure-velocity coupling in the discretized equations. When the pressure field is calculated independently at each grid point without proper coupling to the velocity field, it can lead to non-physical oscillations in the pressure solution. These oscillations manifest as a checkerboard pattern, where adjacent grid points exhibit alternating high and low pressure values, which are not representative of the actual fluid flow. Staggered grid has been widely used to overcome these checkerboard oscillations. Staggered grids, while effective in mitigating the checkerboard problem in Navier-Stokes simulations, pose their own challenges. Firstly, they can complicate the implementation of boundary conditions and the representation of complex geometries due to the non-collocated arrangement of velocity and pressure variables. Secondly, staggered grids often require more complex interpolation schemes for transferring information between the pressure and velocity points, which can increase computational complexity and the potential for numerical errors.

An alternative solution involves using a collocated grid along with Rhie-Chow interpolation, which effectively eliminates checkerboard oscillations. Turning to Maxwell's equations, their original form contains curl operators. When discretized using finite volume methods, these operators necessitate storing variables at locations other than cell centers, such as cell edges and vertices. This leads to challenges akin to those encountered with staggered grid techniques. However, the potential form of Maxwell's equations, involving divergence and Laplacian operators, does not have the issues associated with curl operators. This potential formulation is found to be more suitable for the finite volume discretization framework. With this chosen form of Maxwell's equations, they are expressed in terms of their potentials. The concepts of magnetic vector potential and electric scalar potential are initially summarized. Simply defining these potentials fulfills two of the four Maxwell equations. Subsequently, Maxwell's equations are transformed into their potential form, effectively reducing them from four equations to two.

Validation of Potential Formulation of Maxwell Equations : In this dissertation, the classical problem of a current-carrying wire is solved using the potential formulation of Maxwell's equations. At first, an analytical solution for a current-carrying wire is derived using this potential formulation.

Typically, the integral formulation of the original Maxwell's equations, which are fundamentally expressed in terms of electric and magnetic fields, is used to obtain the analytical solution for the magnetic field of a current-carrying wire. However, in this work, the same analytical solution is derived using the potential formulation of Maxwell's equations. At first, the analytical solution for the electric potential is presented, followed by the derivation of the analytical solution for the current density using this potential. Subsequently, the analytical solution for the magnetic vector potential is calculated, and from this, the exact solution for the magnetic field is derived. This methodical approach aids in validating the solver at each stage of its development.

The potential formulation of Maxwell's equations is solved using a finite volume numerical method and then compared with the derived analytical solution for an axially current-carrying wire. The numerical solutions are found to be in close agreement with the analytical solutions.

The study then extends to radial current flow in a cylindrical domain, where the current flows radially in an annular cylinder from the inner cylindrical surface to the outer cylindrical surface. This simulation is particularly relevant as it closely relates to the current flow in the fusion liquid wall's case, aiding in understanding the boundary conditions for simulating electromagnetic fields in such scenarios. Consequently, this simulation study is conducted with these considerations in mind.

In the case of an axial current-carrying wire, the current density is uniform. However, for radial current flow, the current density decays radially. Additionally, while the magnetic field in the axial current-carrying wire varies only radially, in the radial current case, it changes both radially and axially. This results in a two-dimensional magnetic field for the radial current situation, as opposed to the one-dimensional field in the axial current case. The analytical solution for the radial case is not straightforward, given the two-dimensional nature of the magnetic field. To derive analytical solution, a wider domain is considered, focusing on the central region far from the inner and outer cylindrical surfaces. In this region, the radial dependence is negligible, allowing focus on axial variation, which simplifies the derivation of the analytical solution. The derived analytical solution is found to be in good agreement with the numerical solution. With this validation, the work then proceeded to the next step of integrating Maxwell's equations with the Navier-Stokes equation.

Axisymmetric Simulation Using Wedge Geometry : To simulate axisymmetric problems, wedge geometry is employed, offering several advantages. Without using a wedge formulation, the governing equations would need to be cast in cylindrical coordinates for two-dimensional simulations. However, solving these equations in cylindrical coordinates introduces additional terms, complicating the discretization process. The alternative, a full three-dimensional simulation, can be computationally expensive.

Utilizing wedge geometry for solving axisymmetric problems has its own advantages. It allows for two-dimensional simulations, which are computationally less expensive for axisymmetric problems. Additionally, it enables the use of the Cartesian formulation of governing equations. This is a significant advantage, as discretization techniques and associated numerical methods are more readily available for Cartesian systems, simplifying the computational methods.

The analytical solutions for these axisymmetric problems show good agreement with the numerical solutions obtained using wedge geometry, demonstrating the effectiveness of this approach.

Maxwell-Navier-Stokes Simulations : The previous discussion on Maxwell's equations focused on solid domains. The Maxwell's equations are then extended to include moving conductors, which in this context refer to electrically conducting fluids such as liquid metals. In scenarios where liquid metals flow in the presence of electromagnetic fields, secondary electrical currents and magnetic fields are induced. To accommodate this, Maxwell's equations in their potential form are extended to moving conductors, utilizing Ohm's law for such moving conductors.

Maxwell's equations for moving conductors are then solved in conjunction with the Navier-Stokes equations, which include a body force term known as the Lorentz force, arising due to electromagnetic fields. The combined Maxwell-Navier-Stokes equations are formulated for two specific scenarios: one involving purely applied current, and the other a combination of applied current and an external magnetic field. The latter scenario relates to electrically driven flows. For both these scenarios, the dissertation presents the non-dimensional form of the governing equations, covering both steady and unsteady cases.

To validate the Maxwell-Navier-Stokes system for single-phase flows, electrically driven flows in an annular cylinder is simulated. This test case references Khalzov's dissertation [26], where the evolution of the magnetic field is solved using toroidal field components and poloidal flux functions. In contrast, this study solves the same problem using the potential formulation of Maxwell's equations in Cartesian coordinates.

The setup of the case is as follows: radial currents flow in an annular cylinder from the inner cylindrical surface to the outer cylindrical surface. Additionally, an axial magnetic field permeates the entire domain. The interaction between the radial currents and the axial magnetic field generates an azimuthal Lorentz force, causing the metal to spin. This phenomenon is simulated, and the resulting angular momentum profile shows good agreement with the analytical solution derived from Khalzov's work [26].

Two Phase Maxwell-Navier-Stokes Simulations : The Maxwell-Navier-Stokes equations are further extended to include two-phase flow scenarios with the addition of a volume fraction equation. Physical properties are updated from the volume fraction in these two-phase flow scenarios. Building upon the previous single-phase case, the two-phase version of the electrically driven flow, as outlined in [43, 44], is simulated. In this case, one phase is electrically conducting while the other is not. The setup involves radial currents flowing in an annular cylinder, partially filled with liquid metal, while an axial magnetic field permeates the entire domain. The resulting Lorentz force causes the liquid metal to rotate in the azimuthal direction. The analytical solution for the angular momentum in the liquid metal region is found to be in good agreement with the results from the numerical simulation.

The final study focuses on simulating the two-phase Maxwell-Navier-Stokes equations with the goal of including free surface deformation, representing a fusion liquid wall model scenario. In this model, current from a wire, analogous to the plasma column in a Z-pinch, flows radially through the liquid metal layer. However, the wire or plasma column itself is not part of the model; only the radial current flowing into the liquid metal layer is considered. Unlike the previous study on electrically driven flow in an annular channel, there is no external magnetic field present to rotate the flow.

In this scenario, the radial current flow results in a non-uniform current density along the radius, decaying in the radial direction. Consequently, the magnetic field generated by this current also decays radially. Furthermore, there is an axial variation in the magnetic field, as the enclosed current changes axially, leading to a two-dimensional variation in the magnetic field. This spatially varying magnetic field produces a net downward force within the liquid metal. The resulting Lorentz force leads to a buildup of fluid pressure, causing deformation of the interface, a phenomenon demonstrated through numerical simulation.

Moreover, an increase in the total current inside the liquid metal is shown to accelerate the rate of interface deformation. This is evidenced by comparing the depth of the void and the maximum height of the deformed interface. As the current density increases, the resultant magnetic field becomes stronger, leading to a greater net downward force due to pressure buildup. The simulation shows that the void depth increases with the current density, and consequently, the overall elevation of the free surface also rises as the current density increases.

Recommendation for Future Work : In this study, the Maxwell-Navier-Stokes solver is employed for investigating two-dimensional axisymmetric flows. However, it's important to note that both 'two-dimensional' and 'axisymmetric' are approximations. Naturally, extending the solver to a full three-dimensional model, moving beyond the axisymmetric assumption, is an obvious direction for future work.

Yet, before transitioning to a 3D framework, there is a lot of room for improvement and further study within the current axisymmetric numerical model.

1. Alternate boundary conditions need to be explored to accurately trace the actual current path. It is assumed that the current from the wire changes its direction and flows radially inside the liquid metal layer. This radial flow of current is achieved by setting fixed potentials at both boundaries. However, in reality, the current may exhibit resistance to this directional change, potentially penetrating axially into the liquid metal to a significant depth before transitioning to a radial path. Investigating this behavior could provide insights into the actual dynamics of current transition and the nature of the resulting electromagnetic fields and Lorentz force distribution.

2. When a large current is injected into liquid metal, a significant amount of energy is dissipated as heat due to Joule heating. Therefore, it is essential to solve an evolution equation for temperature in conjunction with the Navier-Stokes equations to account for this effect.

3. The Z-pinch current in a plasma column is pulsed in nature. To accurately represent the actual fusion scenario, it is essential to adapt the solver for pulsed currents. Pulsed currents create waves in liquid metal, as observed experimentally by Dr. Colin Adam's research group [4]. Incorporating this effect could lead to a more realistic representation of the situation during the Z-pinch fusion process.

4. In the fusion liquid wall model study, the current and magnetic field due to the wire are not considered. By utilizing a combination of boundary conditions employed for axial and radial current flows, an attempt can be made to simulate the full model, including the wire. Solving the full model can effectively capture the curvature of current flow as it transitions from axial to radial, providing a more realistic representation of Lorentz force dynamics.

Bibliography

[1] EJ Avital, V Suponitsky, IV Khalzov, J Zimmermann, and D Plant. On the hydrodynamic stability of an imploding rotating circular cylindrical liquid liner. *Fluid Dynamics Research*, 52(5):055505, 2020.

[2] George Keith Batchelor. *An introduction to fluid dynamics*. Cambridge university press, 1967.

[3] Patrick Boissonneau. Magnetohydrodynamics propulsion: a global approach of an inner dc thruster. *Energy conversion and management*, 40(17):1783–1802, 1999.

[4] Kevin Patrick Brannick. *Theory of Wave Formation in Liquid Metal*. PhD thesis, Virginia Tech, 2022.

[5] Francis F Chen et al. *Introduction to plasma physics and controlled fusion*, volume 1. Springer, 1984.

[6] Marwan Darwish and Fadl Moukalled. *The finite volume method in computational fluid dynamics: an advanced introduction with OpenFOAM® and Matlab®*. Springer, 2016.

[7] Peter Alan Davidson. *An introduction to magnetohydrodynamics*. American Association of Physics Teachers, 2002.

[8] Suraj S Deshpande, Lakshman Anumolu, and Mario F Trujillo. Evaluating the performance of the two-phase flow solver interfoam. *Computational science & discovery*, 5(1): 014016, 2012.

[9] ED Doss and HK Geyer. Mhd seawater propulsion. *Journal of Ship Research*, 37(1): 49–57, 1993.

[10] P Fiflis, M Christenson, M Szott, K Kalathiparambil, and DN Ruzic. Free surface stability of liquid metal plasma facing components. *Nuclear Fusion*, 56(10):106020, 2016.

[11] Daniel Fleisch. *A student's guide to Maxwell's equations*. Cambridge University Press, 2008.

[12] TF Flint, MC Smith, and P Shanthraj. Magneto-hydrodynamics of multi-phase flows in heterogeneous systems with large property gradients. *Scientific Reports*, 11(1):18998, 2021.

[13] Flow Z-pinch Lab, University of Washington. Z-pinch attributes. https://sites.uw.edu/zpinchlab/z-pinch-attributes/, 2024. Access the website on: 2024-01-05.

[14] UKNG Ghia, Kirti N Ghia, and CT Shin. High-re solutions for incompressible flow using the navier-stokes equations and a multigrid method. *Journal of computational physics*, 48(3):387–411, 1982.

[15] JB Gilbert, TF Lin, et al. Analytical and experimental studies of the helical magnetohydrodynamic thruster design. In *The Fourth International Offshore and Polar Engineering Conference*. International Society of Offshore and Polar Engineers, 1994.

[16] David J Griffiths and C Inglefield. *Introduction to Electrodynamics, 4th editon*. Cambridge University Press UK, 2017.

[17] Eldad Haber. *Computational methods in geophysical electromagnetics*. SIAM, 2014.

[18] J Hartmann and F Lazarus. Hg-dynamics ii. *Theory of laminar flow of electrically conductive Liquids in a Homogeneous Magnetic Field*, 15(7), 1937.

[19] JT Holgate, M Coppins, and JE Allen. Electrohydrodynamic stability of a plasma-liquid interface. *Applied Physics Letters*, 112(2), 2018.

[20] Fenglei Huang, Dengfei Wang, Zhipeng Li, Zhengming Gao, and JJ Derksen. Mixing process of two miscible fluids in a lid-driven cavity. *Chemical Engineering Journal*, 362: 229–242, 2019.

[21] JCR Hunt. Magnetohydrodynamic flow in rectangular ducts. *Journal of Fluid Mechanics*, 21(4):577–590, 1965.

[22] Michael George Hvasta, Egemen Kolemen, AE Fisher, and Hantao Ji. Demonstrating electromagnetic control of free-surface, liquid-metal flows relevant to fusion reactors. *Nuclear Fusion*, 58(1):016022, 2017.

[23] Raad I Issa. Solution of the implicitly discretised fluid flow equations by operator-splitting. *Journal of computational physics*, 62(1):40–65, 1986.

[24] John David Jackson. *Classical electrodynamics*. American Association of Physics Teachers, 1999.

[25] Hrvoje Jasak. *Error analysis and estimation for the finite volume method with applications to fluid flows*. PhD thesis, Imperial College London (University of London), 1996.

[26] Ivan V Khalzov. *Equilibrium and stability of Magnetohydrodynamic flows in annular channels*. PhD thesis, University of Saskatchewan, 2008.

[27] Abdellah Kharicha, I Teplyakov, Yu Ivochkin, Menghuai Wu, Andreas Ludwig, and A Guseva. Experimental and numerical analysis of free surface deformation in an electrically driven flow. *Experimental Thermal and Fluid Science*, 62:192–201, 2015.

[28] TF Lin and JB Gilbert. Studies of helical magnetohydrodynamic seawater flow in fields up to twelve teslas. *Journal of Propulsion and Power*, 11(6):1349–1355, 1995.

[29] Karl Erik Lonngren, Sava Vasilev Savov, and Randy J Jost. *Fundamentals of Electromagnetics with MATLAB*. Scitech publishing, 2007.

[30] Wladimir Lyra, Colin P McNally, Tobias Heinemann, and Frédéric Masset. Orbital advection with magnetohydrodynamics and vector potential. *The Astronomical Journal*, 154(4):146, 2017.

[31] F Moukalled, M Darwish, and B Sekar. A pressure-based algorithm for multi-phase flow at all speeds. *Journal of Computational Physics*, 190(2):550–571, 2003.

[32] Ulrich Müller and Leo Bühler. *Magnetofluiddynamics in channels and containers*. Springer Science & Business Media, 2001.

[33] Ante Munjiza. Pressure wave in liquid generated by pneumatic pistons and its interaction with a free surface. *International Journal of Applied Mechanics*, 9(03):1–23, 2017.

[34] M Narula, A Ying, and MA Abdou. A study of liquid metal film flow, under fusion relevant magnetic fields. *Fusion Science and Technology*, 47(3):564–568, 2005.

[35] Richard H Pletcher, John C Tannehill, and Dale Anderson. *Computational fluid mechanics and heat transfer*. CRC press, 2012.

[36] Chae M Rhie and Wei-Liang Chow. Numerical study of the turbulent flow past an airfoil with trailing edge separation. *AIAA journal*, 21(11):1525–1532, 1983.

[37] BW Righolt, S Kenjereš, R Kalter, MJ Tummers, and CR Kleijn. Analytical solutions of one-way coupled magnetohydrodynamic free surface flow. *Applied Mathematical Modelling*, 40(4):2577–2592, 2016.

[38] Vernon J Rossow. On flow of electrically conducting fluids over a flat plate in the presence of a transverse magnetic field. Technical report, NASA, Report No. 1358, 1958.

[39] PN Shankar and MD1744305 Deshpande. Fluid mechanics in the driven cavity. *Annual review of fluid mechanics*, 32(1):93–136, 2000.

[40] N Somboonkittichai and GZ Zuo. Surface instability of static liquid metal in magnetized fusion plasma. *Nuclear Fusion*, 63(2):026026, 2023.

[41] Federico A Stasyszyn and Detlef Elstner. A vector potential implementation for smoothed particle magnetohydrodynamics. *Journal of Computational Physics*, 282: 148–156, 2015.

[42] Z Sun, J Al Salami, A Khodak, F Saenz, B Wynne, R Maingi, K Hanada, CH Hu, and E Kolemen. Magnetohydrodynamics in free surface liquid metal flow relevant to plasma-facing components. *Nuclear Fusion*, 63(7):076022, 2023.

[43] Victoria Suponitsky. Axisymmetric mhd with openfoam ("mhdcompressibleinterfoam"). Obtained from General Fusion Inc. through internal communication, 2020.

[44] Victoria Suponitsky and Ivan Khalzov. Test cases for "mhdcompressibleinterfoam" solver. Obtained from General Fusion Inc. through internal communication, 2020.

[45] Victoria Suponitsky, Aaron Froese, and Sandra Barsky. Richtmyer–meshkov instability of a liquid–gas interface driven by a cylindrical imploding pressure wave. *Computers & Fluids*, 89:1–19, 2014.

[46] Victoria Suponitsky, Ivan V Khalzov, and Eldad J Avital. Magnetohydrodynamics solver for a two-phase free surface flow developed in openfoam. *Fluids*, 7(7):210, 2022.

[47] Alessandro Tassone. Magnetic induction and electric potential solvers for incompressible mhd flows. *CFD with OpenSource Software*, 2016.

[48] Jean-Paul Thibault and Lionel Rossi. Experimental modeling of seawater electromagnetic flow control. *ERCOFTAC Bull*, 41(9), 2000.

[49] Xiongbiao Tu, Qiao Wang, Haonan Zheng, and Liang Gao. Meshless methods for magnetohydrodynamics with vector potential. *Journal of Computational Physics*, 470: 111596, 2022.

[50] Henry G Weller, Gavin Tabor, Hrvoje Jasak, and Christer Fureby. A tensorial approach to computational continuum mechanics using object-oriented techniques. *Computers in physics*, 12(6):620–631, 1998.

[51] Frank M White. *Fluid mechanics*. The McGraw Hill Companies,, 2008.

[52] Frank M White and Joseph Majdalani. *Viscous fluid flow*, volume 3. McGraw-Hill New York, 2006.

[53] Wikipedia contributors. Pinch (plasma physics). https://en.wikipedia.org/wiki/Pinch_(plasma_physics), 2024. Access the website on: 2024-01-05.

[54] Zhang Xiujie, Xu Zengyu, and Pan Chuanjie. Mhd effect of liquid metal film flows as plasma-facing components. *Plasma Science and Technology*, 10(6):685, 2008.

[55] Wei Yi, Daniel Corbett, and Xue-Feng Yuan. An improved rhie–chow interpolation scheme for the smoothed-interface immersed boundary method. *International Journal for Numerical Methods in Fluids*, 82(11):770–795, 2016.

Appendices

Appendix A

Vector Identities

$$\nabla\left(\mathbf{A}\cdot\mathbf{B}\right)=\nabla\mathbf{B}\cdot\mathbf{A}+\nabla\mathbf{A}\cdot\mathbf{B} \tag{A.1}$$

$$\nabla\left(\phi\mathbf{A}\right)=\left(\nabla\phi\right)\mathbf{A}+\phi\nabla\mathbf{A} \tag{A.2}$$

$$\left[\mathbf{AB}+\mathbf{CD}\right]\cdot\mathbf{W}=\mathbf{A}\left[\mathbf{B}\cdot\mathbf{W}\right]+\mathbf{C}\left[\mathbf{D}\cdot\mathbf{W}\right] \tag{A.3}$$

$$\nabla\times\left(\nabla\times\mathbf{A}\right)=\nabla(\nabla\cdot\mathbf{A})-\nabla\cdot\nabla\mathbf{A} \tag{A.4}$$

$$\mathbf{A}\times\mathbf{B}=-\mathbf{B}\times\mathbf{A} \tag{A.5}$$

$$\nabla(\mathbf{A}\cdot\mathbf{B})=(\mathbf{A}.\nabla)\mathbf{B}+(\mathbf{B}.\nabla)\mathbf{A}+\mathbf{A}\times(\nabla\times\mathbf{B})+\mathbf{B}\times(\nabla\times\mathbf{A}) \tag{A.6}$$

If A = B, then $\nabla(\mathbf{B}\cdot\mathbf{B})=(\mathbf{B}.\nabla)\mathbf{B}+(\mathbf{B}.\nabla)\mathbf{B}+\mathbf{B}\times(\nabla\times\mathbf{B})+\mathbf{B}\times(\nabla\times\mathbf{B})$ (A.7)

which can be simplified as $\nabla(\mathbf{B}\cdot\mathbf{B})=2(\mathbf{B}.\nabla)\mathbf{B}+2\mathbf{B}\times(\nabla\times\mathbf{B})$ (A.8)

$$\nabla\left(\frac{B^2}{2}\right)=(\mathbf{B}.\nabla)\mathbf{B}+\mathbf{B}\times(\nabla\times\mathbf{B}) \tag{A.9}$$

$$\nabla\cdot(\mathbf{A}\ \mathbf{B})=(\nabla\cdot\mathbf{A}\ )\mathbf{B}\ +(\mathbf{B}\ \cdot\nabla)\mathbf{A} \tag{A.10}$$

If A = B, then $\nabla\cdot(\mathbf{B}\ \mathbf{B})=(\nabla\cdot\mathbf{B}\ )\mathbf{B}\ +(\mathbf{B}\ \cdot\nabla)\mathbf{B}$ (A.11)

Appendix B

Differential Operators in Cylindrical Coordinates

Let ϕ be a scalar function, $\mathbf{A} = A_r\hat{r} + A_\theta\hat{\theta} + A_z\hat{z}$ be a vector field and $\hat{r}$, $\hat{\theta}$, and $\hat{z}$ be the unit vectors in the radial, azimuthal, and axial directions, respectively.

$$\textbf{Del operator :}\ \nabla = \hat{r}\frac{\partial}{\partial r} + \hat{\theta}\frac{1}{r}\frac{\partial}{\partial \theta} + \hat{z}\frac{\partial}{\partial z} \tag{B.1}$$

$$\textbf{Laplacian :}\ \nabla^2\phi = \frac{1}{r}\frac{\partial}{\partial r}\left(r\frac{\partial \phi}{\partial r}\right) + \frac{1}{r^2}\frac{\partial^2\phi}{\partial \theta^2} + \frac{\partial^2\phi}{\partial z^2} \tag{B.2}$$

$$\textbf{Gradient :}\ \nabla\phi = \hat{r}\frac{\partial \phi}{\partial r} + \hat{\theta}\frac{1}{r}\frac{\partial \phi}{\partial \theta} + \hat{z}\frac{\partial \phi}{\partial z} \tag{B.3}$$

$$\textbf{Divergence :}\ \nabla\cdot\mathbf{A} = \frac{1}{r}\frac{\partial(rA_r)}{\partial r} + \frac{1}{r}\frac{\partial A_\theta}{\partial \theta} + \frac{\partial A_z}{\partial z} \tag{B.4}$$

$$\textbf{Laplacian :}\ \nabla\cdot(\sigma\nabla\phi) = \frac{1}{r}\frac{\partial}{\partial r}\left(r\sigma\frac{\partial \phi}{\partial r}\right) + \frac{1}{r^2}\frac{\partial}{\partial \theta}\left(\sigma\frac{\partial \phi}{\partial \theta}\right) + \frac{\partial}{\partial z}\left(\sigma\frac{\partial \phi}{\partial z}\right) \tag{B.5}$$